Porous ß-type Ti-Nb alloy for biomedical applications

DISSERTATION

zur Erlangung des akademischen Grades

Doktor-Ingenieur

(Dr.-Ing.)

vorgelegt

der Fakultät Maschinenwesen

der Technischen Universität Dresden

von

Dipl. Ing. **Ksenia Zhuravleva**

geboren am 27.5.1986 in Sankt Petersburg (Russland)

Contents

Abstract

One of the most important factors for a successful performance of a load-bearing implant for hard tissue replacement is its mechanical compatibility with human bone. That implies that the stiffness should be close to that of a bone and the strength of the implant material must be high enough to bear the load applied under physiological conditions. The Young´s modulus of most of the commonly used biomedical alloys is larger than that of a human bone (around 100 GPa for cp Ti, 112 GPa for Ti-6Al-4V versus 10-30 GPa for cortical human bone). A stiffness reduction of Ti alloys can be achieved by two approaches: (i) selecting an alloy composition with low Young´s modulus i.e. a ß-type alloy and (ii) introducing a reasonable amount of porosity. The composition of Ti-40Nb was chosen for the present work, as it allows to stabilize a single ß-type phase with low Young´s modulus at room temperature.

The samples were produced by a powder metallurgical approach. The Ti-40Nb alloy powder was obtained by ball-milling of elemental Ti and Nb powders. The influence of the milling parameters on the oxygen content in the milled powder was studied. Powders with a lowest oxygen content of 0.4 wt.-% had an almost single ß-type phase after heat treatment and quenching.

Porous samples were produced by loose powder sintering, hot-pressing and sintering with NaCl as a space-holder. The influence of the different processing routes and different porosities on the mechanical properties of the alloy was studied. The samples produced by loose powder sintering had mechanical properties close to those of cortical human bone (Young´s modulus 20 GPa, compression strength 150 MPa) and the samples produced by loose sintering with space-holder materials had mechanical properties close to those of human spongy bone (Young´s modulus 0.2-2 GPa, compression strength 50 MPa)

Porous Ti-40Nb samples were coated with bone-like hydroxyapatite by an electrochemical deposition method in order to improve the osseointegration of the samples with bone tissue. The experiments were carried out with samples produced by different routes and a correlation between the deposition parameters and the morphology of the hydroxyapatite needles was found.

Kurzfassung

Einer der wichtigsten Aspekte für den erfolgreichen Einsatz eines lasttragenden Implantates ist die mechanische Kompatibilität mit den menschlichen Knochen. Die Steifigkeit sollte der des Knochens ähnlich und die Festigkeit hoch genug sein um die physiologisch wirkenden Kräfte aufzunehmen.Der E-Modul der meisten verwendenden Biomaterial-Legierungen ist größer als der des menschlichen Knochens (etwa 100 GPa für cpTi, 112 GPa für Ti-6Al-4V vs. 10-30 GPa für menschlichen kortikalen Knochen). Die Reduktion der Steifigkeit kann durch zwei Ansätze erreicht werden: (i) Die Auswahl der Legierungszusammensetzung mit einem niedrigen E-Modul (ß-Ti-Legierung) und (ii) die Nutzung von Porosität. In der vorliegenden Arbeit wurde die Zusammensetzung Ti-40Nb verwendet, weil mit dieser die Stabilisierung einer metastabilen ß-Phase mit einem niedrigen E-Modul bei Raumtemperatur möglich ist.

Die Proben wurden auf pulvermetallurgischem Weg hergestellt. Das Ti-40Nb-Legierungspulver wurde durch Kugelmahlen von Ti- und Nb-Elementpulvern erzeugt. Es wurde der Einfluss der Mahlparameter auf den Sauerstoffgehalt der gemahlenen Pulver untersucht. Die Pulver mit dem niedrigsten Sauerstoff Gehalt von 0.4 wt.-% wiesen nach einer Wärmebehandlung und Abschrecken fast vollständig die ß-Phase auf.

Die porösen Proben wurden durch Sintern der Pulverschüttung, Heißpressen und Sintern mit NaCl-Platzhaltern erzeugt. Es wurde der Einfluss der verschiedenen Prozessrouten und der unterschiedlichen Porositäten auf die mechanischen Eigenschaften der Legierung untersucht. Die Proben, die durch Sintern der Pulverschüttung hergestellt wurden, wiesen mechanische Eigenschaften ähnlich denen des menschlichen kortikalen Knochen auf (E-Modul 20 GPa, Druckfestigkeit 150 MPa). Die Proben, die durch Sintern mit Platzhaltern erzeugt wurden, zeigten mechanische Eigenschaften ähnlich denen des menschlichen spongiösen Knochens (E-Modul 0.2-2 GPa, Druckfestigkeit 50 MPa).

Die Ti-40Nb-Proben wurden mittels elektrochemischer Abscheidung mit knochenähnlichem Hydroxyapatit beschichtet um die Osseointegration im Knochengewebe zu verbessern. Die Beschichtungen wurden auf Proben, die auf verschiedenen Herstellungsrouten hergestellt wurden, aufgebracht und es wurde eine Korrelation zwischen den Abscheideparametern und der Morphologie der Hydroxylapatit-Nadeln gefunden.

1. Introduction

Metallic biomaterials have a long history. Stainless steel was firstly used as an implant material in the surgical field. Then, Co-based alloys were put into practice. Co-Cr based alloys are the representative Co-based alloys for biomedical applications. They have higher wear resistance as compared to stainless steels. Typical Co-Cr alloys are Co-Cr-Mo, Co-20Cr-15W-10Ni, Co-28Cr-6Mo [1]. Titanium is the newest material among the main metallic biomaterials [2].

There are two main challenges in the design of the metallic implant materials: to make them mechanically and biologically compatible to the human bone. The biocompatibility comprises wear and corrosion resistance, which determine metal release rates, cytotoxicity and tissue reactions which can be caused by this material. Wear loss occurs for example at artificial joints between stem and bone or in case of bone fracture at fixtures between osteosynthesis plates and screws. The corrosion resistance is evaluated by anodic polarization tests in different environments and the results of these tests demonstrated that some elements (like V, Al, Fe, Ni, Co, Cr) are toxic for the human body and are, therefore, not desired in the implant alloys [2]. Ti and Nb are among the "vital" elements and are safe for biomedical applications [3].

Mechanical compatibility implies the reduction of the stiffness mismatch between implant material and bone, which can cause "stress-shielding" effects that strongly retard the mechanical stimulation of bone healing processes [4]. The Young´s modulus of healthy human cortical bone is 15-30 GPa and that of human spongy bone is around 0.2-2 GPa [5]. The Young´s modulus of commonly used bulk implant materials is much larger, e.g. ≈110 GPa for cp Ti, 112 GPa for Ti-6Al-4V and 185-205 GPa for stainless steels.

It has been reported that a single ß-type phase with low Young´s modulus of 60-62 GPa can be stabilized at room temperature for Ti-40Nb by quenching of a cast alloy from the ß-phase region [6]. The Young´s

modulus of the Ti-40Nb alloy can be further reduced to 48 GPa by small alloying additions (e.g. Sn, In) and by thermomechanical processing (cold rolling and annealing). But the achieved value is still not low enough compared to that of human bone [7].

It is difficult to lower Young´s modulus of bulk cast alloys further. But the elastic behavior can be considerably influenced by the introduction of porosity. As for example for Ti at a porosity of approximately 30% the Young´s modulus is nearly equal to that of a cortical bone, i.e. 20 GPa (Figure 1) [8].
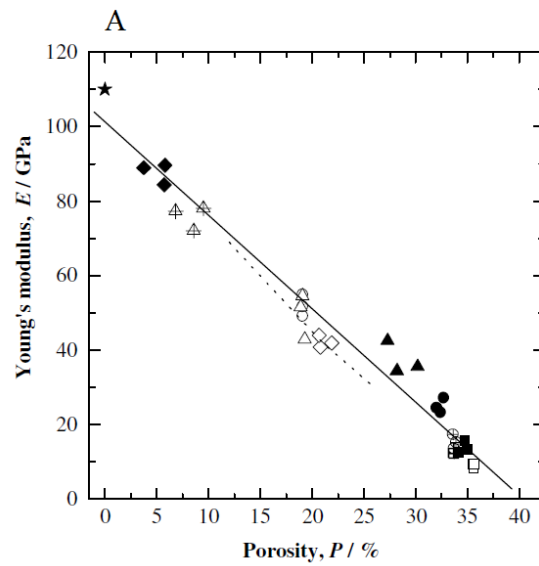
Figure 1: Young´s modulus of sintered porous Ti compacts made from gas-atomized powders as a function of porosity [8].

Ingrowth of bone tissue into pores is decisive for a porous implant to obtain successful osseointegration [9]. The materials surface state plays an extremely important role in the response of the biological environment to the artificial medical device. Calcium phosphate coatings [10] as well as hydroxyapatite coatings [11] improve the osseointegration and increase the bioactivity of the implant surface [12].

The present study describes successful routes of producing biocompatible and mechanically compatible Ti-40Nb porous alloy samples. Firstly, Ti-40Nb alloy powder is produced by ball-milling and the correlation between the oxygen contamination and the milling parameters is discussed. To design alloy bodies with desired mechanical properties several compaction routes were applied. In the present work loose powder sintering and a space–holder technique are used. A route to obtain samples with interconnected porous architectures with controlled porous size and shape is demonstrated. ß-type Ti-40Nb samples made from loose sintered powder have a low Young´s modulus value. Samples with mechanical properties very close to those of human cortical bone and human spongy bone are produced by loose powder sintering and sintering with NaCl space-holders. The porous samples are then electrochemically coated with hydroxyapatite. The correlation between the deposition parameters and the morphology of hydroxyapatite crystals is demonstrated.

Chapter 2

Theoretical background

2.1. Basic materials requirements for long-term load-bearing implant applications

The successful performance of long-term load-bearing metallic implants for osteosynthesis applications in the human body depends on many factors. One of the most important of them is the mechanical compatibility of the material. A second important factor is a high corrosion and wear resistance of the material that will minimize the metal release rate and, thus, a negative tissue reaction of the metallic implant in the body. There is a group of metallic elements, known as "vital elements", which possess a low cytotoxicity and are relatively safe to be inserted in a body for long-term use [2]. The third important factor is a high biofunctionality of the surface, which basically depends on the chemistry and the topography of the surface. To improve the biofunctionality different surface treatments and coatings can be applied.

2.1.1. Mechanical compatibility

Metals and their alloys are used as biomaterials because of their stiffness, strength and toughness. Most important are stainless steels, Co-Cr alloys, Ti and its alloys. Co-Cr alloys were found to be the most inert materials. Ta was introduced in medical practice, but had poor mechanical properties and difficulties in processing. Steel implants were cheap and simple in processing, but could corrode in the body under certain circumstances, for example in highly stressed regions [13]. Co-Cr alloys have good wear, corrosion resistance and fatigue strength but contain elements which are harmful for the body, so the application of these alloys is strongly limited. The materials to replace Co-Cr alloys were Ti and its alloys. They are very light (e.g. the Ti density is 4.5 g/cm^3 compared to 7.95 g/cm^3 for 316 stainless steel and 9.2 g/cm^3

for a wrought Co-Ni-Cr-Mo alloy) and have good mechanochemical properties. Ti-6Al-4V is an (α+ß) type alloy that is widely used as a biomaterial.

But a main problem is that of a significant stiffness mismatch, which is expressed in a large difference between the Young's modulus of a human bone and that of a bulk metallic implant material (e.g. 112 GPa for Ti-6Al-4V and ≈100 GPa for cp Ti). The Young´s modulus of human cortical bone is 15-30 GPa and that of human spongy bone is around 0.2-2 GPa [5], which is considerably lower than that of most of the commonly used implant materials (Figure 2). This mismatch can cause a so-called «stress-shielding» effect: the implant is stiff and carries a great part of the load applied under physiological conditions. A bone that is not properly loaded does not feel the normal physiological stress and becomes weaker. The stress-shielding retards bone remodeling and healing and results in an increased porosity of the bone surrounding the implant. This mismatch of the stiffness has been identified as a major reason for implant loosening [14]. Therefore, a reduction of this mismatch by decreasing the value of Young´s modulus is an important concern in implant materials design.
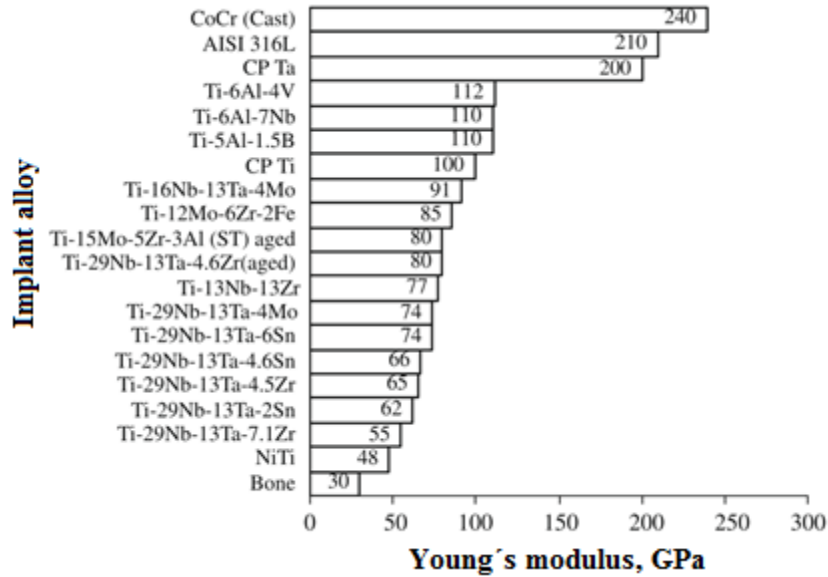
Figure 2: Values of Young´s modulus of most commonly used biomedical alloys [15].

The Young´s modulus of the most commonly used implant alloys is too high compared to that of a human bone as demonstrated in Table 1. The Young´s modulus of a cast Co-Cr alloy is 230 GPa which is way too high compared to that of a human bone. Stainless steel demonstrates a Young´s modulus of ≈200 GPa which is too high as well. Ti and α-type Ti alloys have a lower Young´s modulus of ≈110 GPa. ß-type Ti alloys have lower Young´s modulus than α-type, for example the Young´s modulus of ß-type Ti-13Nb-13Zr alloy is 79 GPa.

Another important mechanical characteristic for implant alloys is their strength. In case of a bone fracture, main support will be provided by an osteosynthesis plate made from cast alloys. These plates should provide the support for the bone and a high mechanical strength. The porous bodies for hard tissue replacement can be used as mechanically stable substrates of resorbable biomaterials (drugs, bone cements) directly in the bone defects. Their strength should be comparable to that of a human bone, i.e. 70-150 MPa for cortical bone and 5-50 MPa for spongy bone [5]. The compressive yield strength of the most commonly used implant materials is presented in Table 1.

Table 1. Physical and mechanical properties of various implant materials in comparison to natural bone [16], [17].

Properties	Natural bone	Co–Cr alloy	Stainless steel	α-type Ti	ß-Ti-13Nb-13Zr
Density (g/cm^3)	1.8–2.1	8.3–9.2	7.9–8.1	4.4–4.5	4.5-5.5
Elastic modulus (GPa)	3–20	230	189–205	110–117	79
Compressive yield strength (MPa)	130–180	450–1000	170–310	758–1117	620-900
Fracture toughness (MPam$^{1/2}$)	3–6	N/A	50–200	55–115	N/A

To sum up the literature data it can be concluded that ß-Ti alloys are generally preferred materials for biomedical applications due to their relatively low modulus. The Young´s modulus of ß-type Ti alloys is relatively low compared to that of α-Ti or other implant biomaterials, but still too high compared to that of a human bone. Further reduction of Young´s modulus of ß-type Ti alloys is needed. The compressive yield strength of ß-type Ti alloy should be as high as possible as well as its fracture toughness.

2.1.2 Biocompatibility of materials for long-term load-bearing implants

Important characteristics of long-term load-bearing implant materials are wear and corrosion resistance, which determine the release of metallic species into the physiological environment and, therefore, the cytotoxicity and the tissue reactions which can be caused by this material. The wear mechanisms for titanium alloys are roughly grouped into abrasive wear and adhesion wear. Adhesive wear is considered to be the predominant wear mechanism within a living body [18]. The wear of the material inside the human body should be kept as low as possible. A good corrosion resistance of Ti and its alloys results from the spontaneous formation of very stable protective oxide films (mainly TiO_2) on metal surfaces in a wide range of corrosive media [19].

The corrosion resistance is evaluated by anodic polarization tests in different environments. Typical data from literature for polarization resistances of elements and alloys used in implant materials were summarized by M. Niinomi [3] and are plotted against their biocompatibility in Figure 3. The polarization resistance corresponds to the metal ion release rate in the physiological environment. These most commonly used metals were classified in three groups according to their biocompatibility: harmful, neutral and vital. Vital elements like Ti, Ta and Nb have a very high corrosion resistance, respective a very low metal release rate, and can therefore be used for long-term implantation in the body. Different metallic ions released from implants can cause different tissue reactions. For example, Al is considered to cause the Alzheimer disease [20]. Ni as well as Co and Cr cause a metal sensitivity and allergic reactions [21]. Finally it can be concluded that the release of ions depends upon the corrosion rate of the alloy and on the solubility of the first formed corrosion products. Consideration of corrosion product stability in tissue further limits the choice to Ti, Ta, Nb, and Zr and some of their alloys [17].
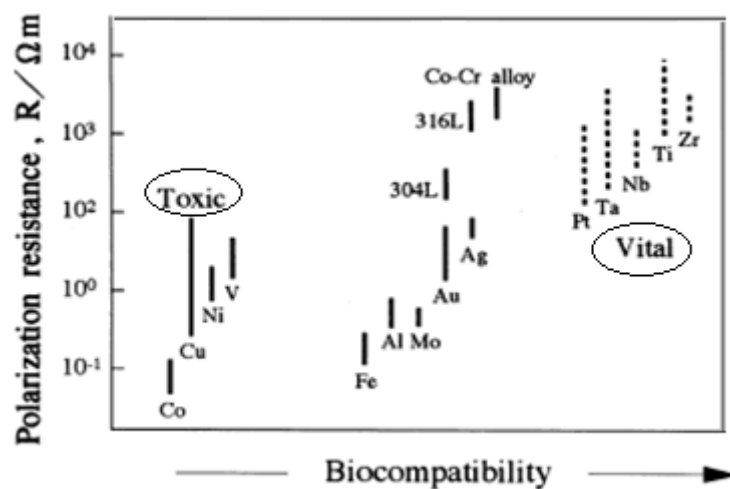

Figure 3: Polarization resistance and biocompatibility of metals used for implant materials [5].

8

The survival rate of living cells on the substrate indicates the cytotoxicity of the material [22]. In an investigation by Hornez et al. [23] it has been demonstrated that Pt, Sn, In, Ti, Au and Pd are "vital" elements; Cr, Cu and Ag are toxic, while Ni, Zn, and Co are highly toxic. Calcium is as well the main element in the mineral phase of bone and so it is unlikely to be toxic even if large amounts are released [24]. Mg is used for biodegradable implants and is considered to be not toxic according to the work by Staiger et al. [16]. Co and V are higher in cytotoxicity than Ni, Cr, Mo and Al [25]. It has been also identified that certain ions are transported inside the body from the implant site and are finally concentrated in various organs, like liver, lung, spleen, lymph node [26]. This body reaction does not appear immediately but has long term consequences. This must be considered in a new materials design.

The cytotoxicity response of α+ß Ti–6Al–4V was found to be better than that of pure Ti or of ß-phase Ti–29Nb–12Ta–46Zr alloy [22]. ß-Ti alloys based on the Ti-Mo system were found to be not desired for a long stay in the body, because a large amount of Mo was associated with severe tissue reactions in animal studies [26]. Elimination of Mo was preferred in Ti-15Zr-4Nb-2Ta-0.2Pd alloys, although it included elemental Sn and Pd which do not show a good biocompatibility [26]. The cell viability of studied Ti–Ta alloys is almost the same as that of pure Ti [19].

2.1.3. Surface functionality

The events after implantation include interactions between the biological environment and artificial material surfaces. The material surface plays an extremely important role in the response of the biological environment to the artificial medical devices. In case of implants made of titanium, the normal manufacturing steps usually lead to an oxidized, contaminated surface layer that is often stressed and plastically deformed, non-uniform and rather poorly defined. Proper surface modifications are intended to improve the bioactivity, biocompatibility, blood compatibility, wear and corrosion resistance of titanium

and titanium alloys. There are several surface modification methods in use based on mechanical, chemical and physical processes which are reviewed and described according to the formation mechanism of the modified layer on the surface of titanium and its alloys [27]. Common mechanical surface modification methods are machining, grinding, polishing and blasting. The typical objective of mechanical modifications is to obtain specific surface topographies and roughness, to remove surface contamination and, therefore, to improve bone tissue adhesion [28].

Chemical methods include chemical treatments, electrochemical treatments (anodic oxidation), sol–gel coatings, chemical vapor deposition (CVD) and modifications with bioactive molecules. Chemical treatments comprise such techniques as acid treatment (used to remove oxides and contaminations), hydrogen peroxide treatment (improves the bioactivity of titanium implants), alkali treatment (titanate formation enables the formation of a biologically active bone-like apatite layer), anodic oxidation (produces different types of protective oxide films on metals) and many others. A typical alkali and heat treated Ti surface is shown in Figure 4a.
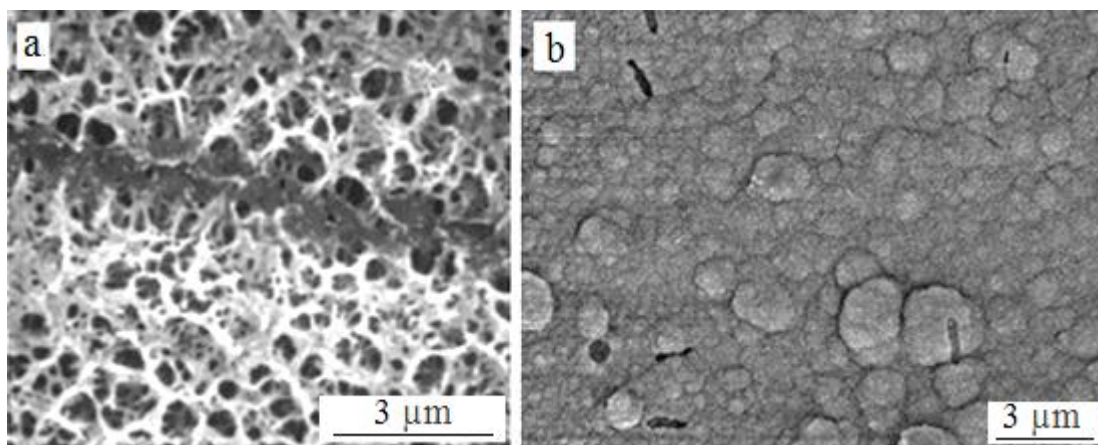

Figure 4: Typical Ti surfaces after (a) alkali and heat treatment and (b) Ca ion implantation [27].

Among the most commonly used physical methods are plasma spraying (often used to form ceramic coatings), ion plating (energetic bombardment with particles that alter the substrate surface and influence the film formation process), sputtering (a relatively simple method to deposit thin films), ion implantation (energetic ions are introduced into the surface layer of a solid substrate via bombardment) [27]. A typical Ti surface after Ca ion implantation is presented in Figure 4b.

Porous architectures of an implant surface or of the implant itself are considered to be beneficial for the bone cell activity and finally for bone tissue growth. The ingrowth of bone tissue into pores is decisive for a porous implant to obtain successful osseointegration. One critical factor for bone ingrowth is the pore size. According to a study by Xue [9] the bone cells span directly across the small pores with size less than 150 μm. For the pores with a size less than 100 μm, cells did not grow into the pores. If the size of a pore was more than 200 μm, cells could not span directly across it. In those cases, growth of bone cells was observed only in the interior of these large pores. Although the optimum pore size required for effective bone ingrowth is still under discussion, Xue et al. concluded that in order to optimize capillary tissue and osteoprogenit or cell migration into porous spaces, pore sizes larger than 100 μm are necessary. It was observed that porous samples not only enhanced cell adhesion and proliferation, but also stimulated cell differentiation.

2.2. Ti and Ti alloys for implant applications

2.2.1. Ti and its alloys: structure-property relations

Ti is a widely used material for biomedical applications because of its comparatively high biological compatibility and good corrosion resistance. The main problems of Ti implants are: low shear strength, low wear resistance and a too high Young´s modulus [29]. To solve these problems the improvement of

mechanical properties is necessary. This requires a principal understanding of structural aspects as basis for an utilization of structure-property relations.

Pure Ti crystallizes at low temperatures in hexagonal closed packed structure, a hcp α-phase (space group *P6₃/mmc*), and yields a Young´s modulus of ≈100 GPa.
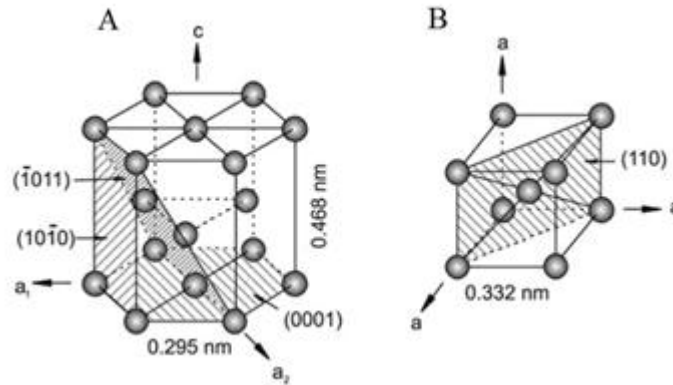

Figure 5: Crystal structure of hcp α- and bcc ß-phases [30].

The temperature of the α- to ß-phase transformation in pure Ti is $T_{Ti}^{\alpha\to\beta}=$ 882°C. The atomic unit cells of α- and ß-phases are presented in Figure 5 (a) and (b), respectively. The hcp α-phase has a limited plasticity compared to the bcc ß-phase. As discussed before, the ß-phase (bcc, space group Im$\bar{3}$m) has much better mechanical properties related to biomedical applications of the material. By alloying Ti with different elements it is possible to change the temperature of the α→ß transformation or even to stabilize a single ß-phase at room temperature upon certain thermal treatments. Depending on their influence on the ß-transition temperature, the alloying elements of titanium are classified as neutral, α-stabilizers and ß-stabilizers. Neutral elements such as Sn and Zr are soluble in both α- and ß-phases and do not have a significant influence on the transformation temperature. The α-stabilizing elements (Al, O, N and C) extend the α-phase field to higher temperatures and develop an α+ß area as shown in Figure 6. There are

two types of ß-stabilizing elements according to their influence on the phase transformation in the alloy: ß-isomorphous and ß-eutectoid. ß-isomorphous elements such as Mo, V, Ta, Nb are completely dissolvable in the ß-phase. A schematic phase diagram for this kind of elements is presented in Figure 6. The more of these elements are added to the alloy the lower is the decrease of the ß- transition temperature. The ß-eutectoid elements have a limited solubility in Ti and form intermetallic phases by eutectoid decomposition of the ß-phase. Typical ß-eutectoid elements are Fe, Mn, Cr, Co, Ni, Cu, Si and H.
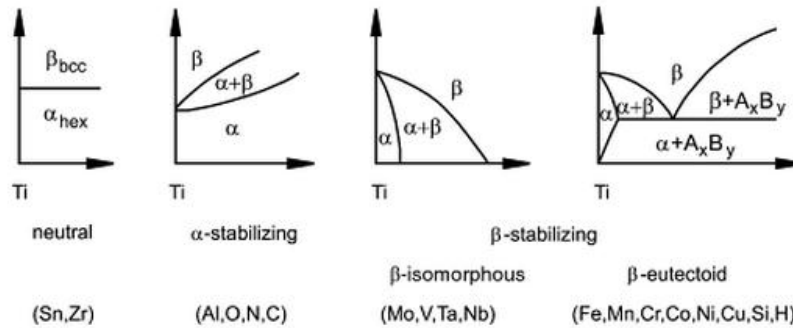
Figure 6: Influence of alloying elements on phase diagrams of Ti alloys [30].

The phase composition of Ti alloy can be controlled by the alloying elements and the thermal treatment routes. The use of ß-stabilizing elements is beneficial to fulfill the demand to reduce the Young´s modulus of Ti alloy (see 2.1.1) but those alloying elements should be "vital" and cause no tissue reaction (see 2.1.2). Therefore, the choice of alloying elements is limited to Ta and Nb.

2.2.2. The Ti-Nb system

In the equilibrium Ti-Nb phase diagram there are only two stable solid phases (see Figure 7): the hcp α-phase and the bcc ß-phase. There are the two melting points $T_{Ti}^{ß \to L}= 1670°C$, $T_{Nb}^{ß \to L} =2469°C$ and the allotropic transformation temperature of titanium $T_{Ti}^{\alpha \to ß}= 882°C$. At a very low Nb content up to 3 at.-%

the stable phase at room temperature is the hcp α-phase. With increasing Nb content the α+ß mixture is stabilized at room temperature. The higher the Nb content is in the alloy, the higher is the fraction of the bcc ß-phase in this phase mixture. At a concentration of 40 at.-% Nb the ß-phase becomes stable at room temperature. Normally, the ß-phase is a high temperature phase and the ß-transition temperature decreases with an increasing Nb content.
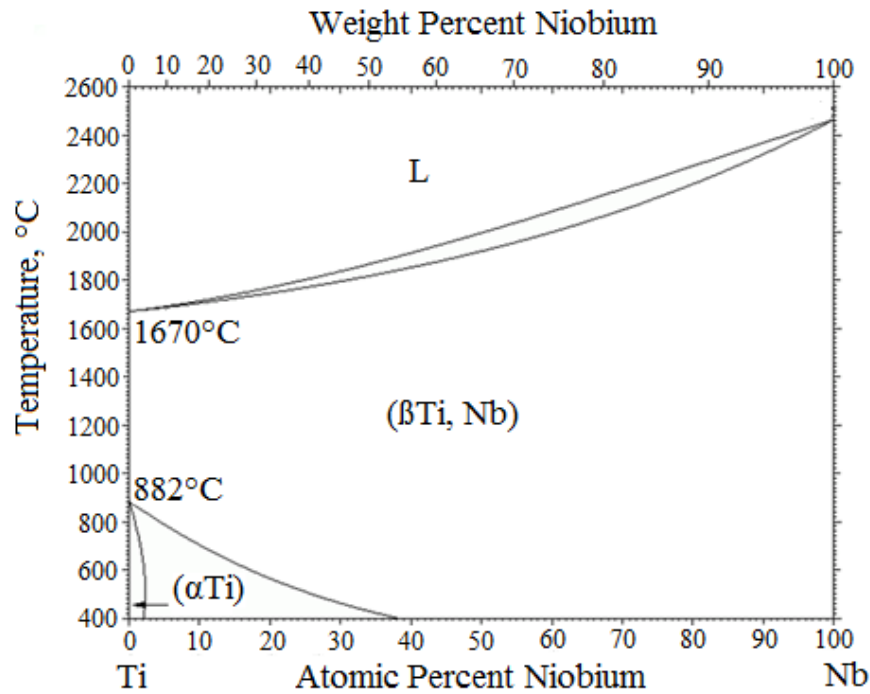
Figure 7: Equilibrium phase diagram of Ti-Nb system [31].

Under non-equilibrium conditions there are several metastable phases that can occur in the Ti-Nb system. Their presence depends on both the composition of the alloy (amount of Nb) and on the cooling rate. There are two diffusionless transformations which occur in titanium rich alloys during quenching from the ß-phase field. These two phases, the martensites a' and a", and the ω phase compete to form in the metastable bcc matrix. The calculated T_0 curves are shown in Figure 8. A T_0 curve consists of points at

which the free energies of two phases are equal. If the temperature is below or equal to T_0 a single phase alloy of one crystal structure may transform to another crystal structure without a change in composition. The temperature of martensite transformation T_s lies below T_0, because the formation of martensitic α´and α´´ phases strain the matrix and an additional driving force is needed to overcome this [32]. The formation of ω-phase strains the matrix even more, so its curve lies even lower. Alloys with less than 14.3 at.-% Nb will be martensitic at room temperature after rapid quenching from the ß-phase region. Two martensitic phases are known: α' (hexagonal space group *P6₃/mmc*) and α" (orthorhombic structure, space group *Cmcm*). The composition of the alloy determines which martensite is formed. The ω-phase (hexagonal structure, space group *P6/mmm*) precipitates during slow quenching from the ß-phase region or forms during isothermal aging [32].
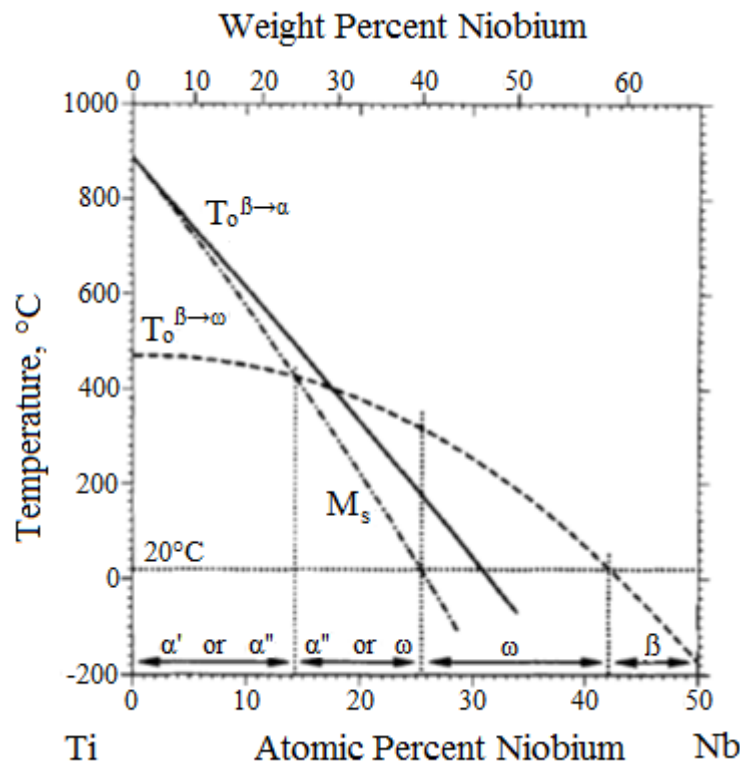
Figure 8: Non-equilibrium phase diagram of Ti-Nb [32].

Between 14.3 and 25.5 at.-% Nb the alloys contain ω-precipitates if slowly cooled to 20°C and martensite if rapidly quenched. Alloys with more than 25.5 at.-% Nb cannot have a martensitic microstructure at room temperature. Quenched alloys with compositions between 25.5 and 42.2 at.-% Nb may contain ω precipitates at room temperature. Alloys with more than 42.2 at.-% Nb should be single-phase ß at 20°C [33], [32].

The different stable and metastable phases have different Young´s modulus values. The lowest Young´s modulus has the ß-type phase and the ω-phase has the highest [34], [35]. In the work of Ozaki [6] a correlation between the Nb concentration and Young´s modulus of the alloy is demonstrated. This curve was plotted for cast Ti-Nb alloys after quenching into Cu moulds (Figure 9).
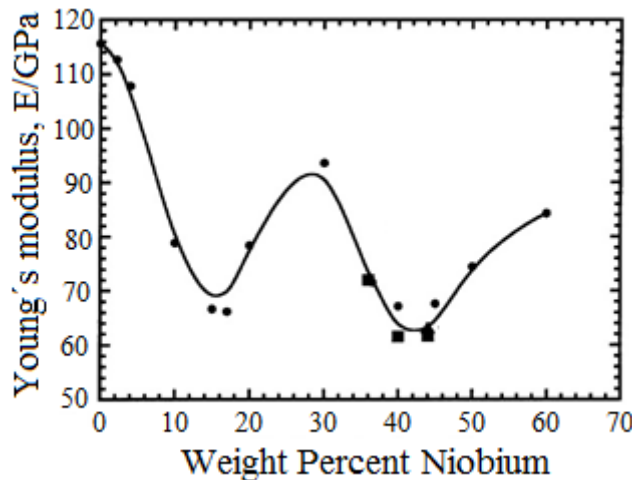
Figure 9: Effect of Nb content on Young´s modulus of quenched Ti-Nb alloys [6].

At very low Nb content Young´s modulus of the alloy is close to the Young´s modulus of pure Ti, i.e. ≈110 GPa. With growing Nb content the Young´s modulus decreases because of the presence of martensitic α´or α´´ phases. The first local minimum in the curve appears at 15 wt.-% Nb and is around

70 GPa. With increasing Nb content Young´s modulus increases up to 90 GPa at ≈ 30 wt.-% Nb. In this interval ω-precipitations are present in the quenched alloy and enlarge its elastic modulus. The martensitic alloys with <30 wt.-% Nb are promising materials for biomedical shape-memory applications [36]. The second minimum of the curve appears at ≈40 wt.-% Nb and corresponds to a single ß-phase alloy. The value of its Young´s modulus is 62 GPa [6]. The Ti-Nb system is a well-established thermodynamic system, since it is of interest for a variety of applications. Earlier studies refer to an application of these alloys as superconducting material [37].

2.3. Porous Ti-based materials

A certain amount of porosity in an implant allows to mimic bone structures and simultaneously to provide customized mechanical properties. Thus, porosity is beneficial for both improvement of the osseointegration of a bone and reduction of Young´s modulus of an alloy sample. A major disadvantage of porous bodies is their limited strength.

An example of the correlation between mechanical properties of metallic bodies and their porosity was demonstrated in a fundamental work by Oh et al. [8]. The porous bodies were produced by sintering of gas-atomized cpTi powders. Obviously, Young´s modulus decreases linearly with increasing porosity (Figure 10 a). It can be concluded that the Young´s modulus of Ti compacts can be controlled in the range between 110 GPa (full density) and 9 GPa at a porosity of 35%. Most importantly, Young´s modulus values of the compacts with porosities from 32 to 36 % are comparable to that of human cortical bones, i.e. around 20 GPa.
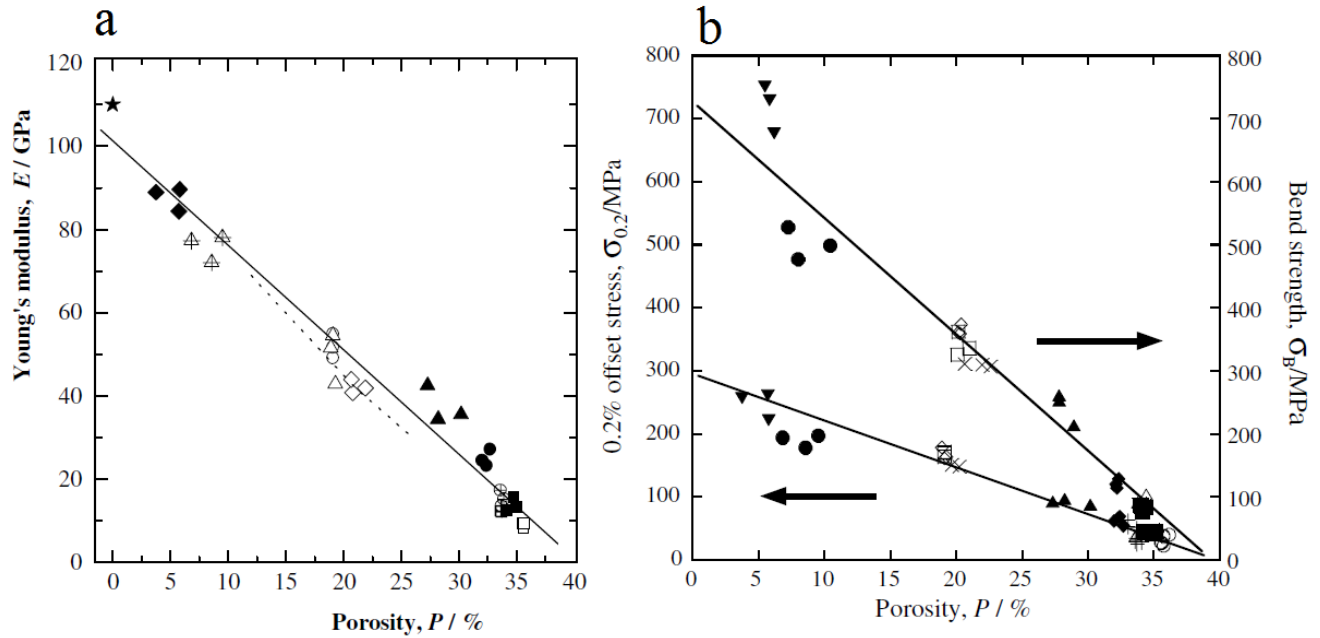
Figure 10: (a) Young´s modulus of sintered cpTi compacts made from gas-atomized powder as a function of porosity and (b) three-point bending strength and 0.2% offset compressive strength of sintered porous Ti compacts as a function of porosity [8].

Nomura et al. found that with the increasing porosity from 10 to 40% in the porous samples obtained from loose sintered cp Ti the Young´s modulus reduces according to the following law:

$$E = E_0 \cdot (1 - P)^b \tag{1}$$

where E_0 is Young´s modulus of Ti ($\approx$110 GPa), P – the porosity and b - constant that is equal $\approx$5 for this particular material [38].

The increase porosity reduces the strength of the alloy as well as demonstrated in Figure 10b. At a porosity of 32-36 % the strength of the samples was below 100 MPa. To find a compromise between low Young´s modulus and suitable strength of an alloy is an important challenge for the design of biomedical materials.

The necessity of porosity in materials for hard tissue replacement for bone regeneration has been shown by Kuboki et al. [39]. Scaffolds for good osseointegration should mimic the bone morphology, structure and function. The interconnection of the pores as well as the pore size is important factors for bone ingrowth inside of the implant. Large pores (100–150 μm and 150–200 μm) yielded substantial bone ingrowth. Smaller pores (75–100 μm) resulted in ingrowth of unmineralized tissue. Smaller pores (10–44 and 44–75 μm) were penetrated only by fibrous tissue. The optimum pore size for metallic scaffolds is presently considered to be 100-400μm [40].

The most commonly used ways to produce porous metallic alloys are powder metallurgical methods. The simplest method to obtain porous bodies is powder sintering. The loose powder sintering process consists of two steps: (i) green powder compaction and (ii) sintering. For detailed description of loose powder sintering see section 2.3.2.2 a. This method allows to obtain porosity values in the range of 5 to 45% [8]. The obtained porosity is formed in the gaps between the powder particles (see Figure 19a) and comments to it) and depends on particle shape and size, compaction pressure and sintering temperature. When the total porosity of the sample is higher than 19% almost all the pores are interconnected [40]. For green compaction an important property of the powder is its shape and, therefore, its production method. Different production methods result in different shapes of the powder particles (spherical, irregular, flakes-like and so on) and a different green strength of the compressed samples (see Table 2). Due to its irregular shape ball-milled powder has good green strength and compressibility and, thus, yields porous samples with a relatively high strength [41].

Methods that allow to control the porosity as well as the pore size and shape are space-holder methods. Different space-holder materials are added to the metallic powders during the initial green compaction or hot-pressing step. Some space-holders like bicarbonate (NH_4HCO_3) are not stable at high temperatures and, therefore, can be only added for compaction at room temperature or can be evaporated at a

temperature of 300-600 °C before the final sintering step [42]. Mg powder can be also used as a space-holder: it is suitable for green compaction as well as for hot-pressing, because the evaporation temperature of Mg is higher than that of organic space-holders. Mg is removed during a sintering step at 1000-1200°C [43, 44]. Metallic gas-atomized Mg powder particles have a spherical shape and yield almost spherical shapes of the pores as seen in Figure 11 a). NaCl particles can also be used as a space-holder material. The boiling temperature of NaCl is high, i.e. around 1410°C, so that it can be used for green compaction, hot-pressing and sintering and will be finally removed by immersion in water. NaCl powder particles have a cubic shape and, therefore, also yield a cubic shape of the pores as can be seen in Figure 11b). The main advantages of using NaCl as a space-holder are its low cost and that it is easily dissolved in water. Besides that NaCl in small amounts is not harmful for a living body and can be used for production of alloys for biomedical applications [45].
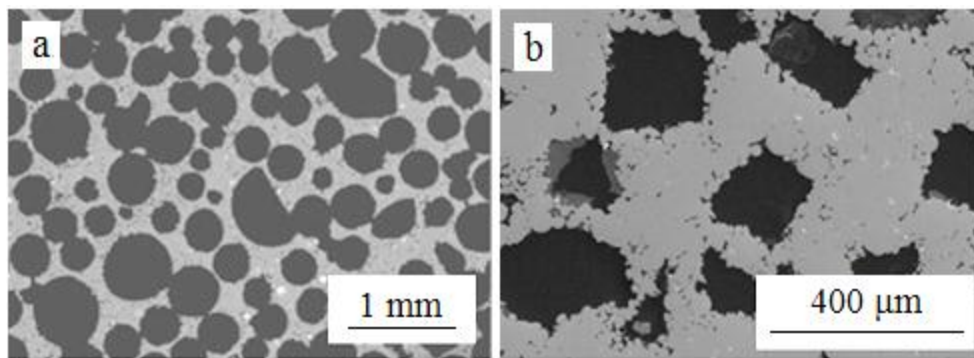
Figure 11: Porous Ti alloys produced with (a) Mg sphere-shaped particles as space-holder; (b) NaCl cubic-shaped particles as space-holder.

Another widely used powder metallurgical method to produce porous samples with desired pore size distribution and pore geometry is selective laser melting (SLM). This method allows to process samples with complicated geometry directly from the three-dimensional (3D) CAD-data. The building of the sample from the metallic powder occurs layer by layer. The energy for the sintering or melting of the

20

powders is provided by a laser beam that scans the powder layer and melts it according to the CAD-data. After the melting a fast solidification of the layer occurs that allows to stabilize metastable phases in SLM processed samples [46]. An example of a body with directional pores produced by this method is presented in Figure 12. The metallic powders are heated to very high temperatures and rapidly cooled, so it is possible to stabilize metastable phases in the final product. By this method an almost fully dense material (99% density) or very porous structures can be produced. The samples produced by the SLM method demonstrate outstanding mechanical properties. For example, Zhang et al. [47] succeeded in obtaining 99.3% dense samples from gas-atomized ß-type Ti–24Nb–4Zr–8Sn powder. The authors confirmed a single ß-phase composition of the alloy after building. The Young´s modulus of these samples was around 53 GPa, the ultimate tensile strength reached ~660 MPa and the strain exceeded 10%.
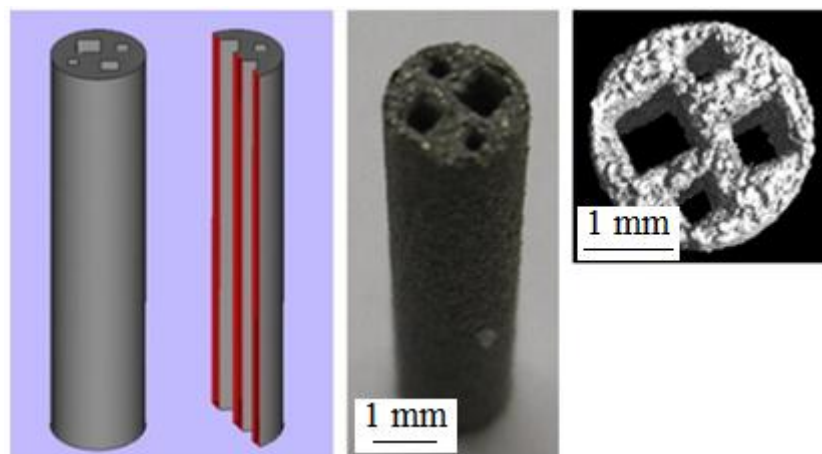

Figure 12: Sample with directional pores produced by the SLM technique from Ti gas-atomized powder [49].

Pattanayak et al. [48] carried out SLM of pure Ti gas-atomized powder. They have demonstrated that at porosities in the range of 75‑55% the compressive strength appears to be in the range of 35‑120 MPa [48].

In a study by Facchini [46] a Ti-6Al-4V alloy produced by SLM is compared to that produced by SLM with further post-building heat treatment (hot working and annealing). The Young´s modulus is in both cases around 105 GPa and the material was fully dense (relative density 99.7 ± 0.1%). The tensile strength of SLM samples is significantly higher than that of hot worked and annealed samples, i.e. 1095 MPa and 870 MPa, respectively. The reason for the difference in the mechanical properties of the alloys is the different phase composition. In the SLM processed sample the phase composition was determined as α+ß phase mixture with the presence of martensitic α´´-phase. A post-building heat treatment causes the transformation of the metastable martensite α´´ in the α-phase, with a morphology that depends on the heat treatment, resulting in an increase in ductility and a reduction of strength values. The SLM of Ti-based powders is a relatively new and very challenging technique, that is why there is not much literature data available until today.

Another relatively new powder compaction technique is spark plasma sintering (SPS). During the SPS process a pulsed current generates plasma that activates the surface of the powder. An applied pressure makes the powder flow and thus, forming dense materials with an ultrafine microstructure is possible as the processing time is short. This technique was applied by Handtrack et al. to synthesize Ti-Si alloy samples with high strength and hardness from ball-milled powder. The density of sintered powder varied depending on the sintering parameters and went up to almost 100% of the theoretical density. The samples demonstrated a relatively high bending strength of 1650 MPa. The new material shows high hardness, strength and improved wear resistance in comparison to other titanium materials [50].

2.3.1 Metal powder processing

2.3.1.1 Ball-milling

Metal powder production methods are classified as: mechanical, chemical and physical. Among the mechanical methods are for example: fluid energy grinding, machining, shutting and graining. One of the commonly used physical methods is gas-atomization. Typical chemical methods include reduction, thermal decomposition or hydride-dehydrate process [51].

High energy ball-milling is one of the most effective mechanical methods. This process involves repeated welding, fracturing and re-welding operations of metallic powder particles leading to microstructural refinement and phase formation and transformation reactions. Elemental powders are mixed in a special vial and milled using metallic balls for a suitable time. The high energy generated by the ball collisions is transferred to the powder particles and introduces the above mentioned process up to alloying. Another approach is to use pre-alloyed material (for example, made by casting), when the ball-to-ball collisions will cause a refinement of the alloy powder. One of the greatest problems of ball-milling is the contamination of the resulting powder with wear products from the milling tools, impurities from the milling atmosphere and decomposition of the milling agents. Ball-milled powder is usually contaminated with O, N, C and Fe. Another problem of this method is a relatively small powder yield, especially if the milled materials are ductile. The powders tend to cold weld to the milling balls as well as to the walls of the vial. To overcome this problem different milling and anti-sticking agents are used, cryomilling and milling in different atmospheres (for example in hydrogen) are used [52].

During intensive ball-milling several processes can occur: grain size reduction that can lead to the formation of nanocrystalline material, mechanical alloying of starting powders resulting in alloy

formation or in the presence of milling agents or reactive atmospheres, chemical reactions, like oxidation or hydrate formation.

a) Nanocrystalline metals or alloys produced by ball-milling

A significant reduction of grain sizes is a well-known phenomenon that occurs during ball-milling. Grain sizes with nanometer dimensions were reported for many mechanically alloyed metals, alloys and intermetallics. There have been many studies carried out to explain the grain size reduction process. Hellstern et al. [53] reported that there is an enhanced shear band formation observed at the early stages of milling because of the high deformation rates. With continued milling the average atomic level strain increases due to the increasing dislocation density. At a certain dislocation density within these heavily strained regions the crystal structure disintegrates into subgrains that are separated by low-angle boundaries. This results in a decrease of the lattice strain. On further processing the deformation occurs in shear bands located in previously unstrained parts of the material. The small angle grain boundaries are replaced by higher angle grain boundaries. Consequently, dislocation-free nanocrystalline grains are formed [51]. Because of their novel combinations of mechanical, physical, and magnetic properties they have received considerable attention in the past few years [54].

b) Amorphous alloys by ball-milling

A solid alloy with a liquid-like (short range ordered) atomic arrangement is called an amorphous (metallic) alloy or metallic glass. The amorphous phase has been synthesized starting from: blended elemental powder mixtures, pre-alloyed powders, mixtures of pre-alloyed powder and mixture of pre-alloyed with elemental powders. When starting from pre-alloyed materials, the reduction of the grain size down to the nanometer scale is followed by the final amorphisation that occurs by an interdiffusion step.

When starting from elemental metal powder mixture or mixture of pre-alloyed materials with elemental powders, the mechanical alloying process must take place (as described in detail in 2.3.1.2).

The most important experimental parameters for an amorphization process to occur are: milling energy, milling temperature and impurity contamination. A strict control of the constitution of the intermediate and final milling products is necessary. An increased milling energy is normally expected to introduce more strain and to increase the defect concentration in the powder and, thus, leads to easier amorphization. However, higher milling energies also produce more heat (and higher temperatures) and this can result in a crystallization of the amorphous phase. Therefore, a balance between these two effects will determine the nature of the final product phase formed [51].

The presence of additional contaminating elements can favor the amorphization. For example, it has been reported that an amorphous phase was obtained in ball-milled Fe–Cr alloy powders only in the presence of oxygen [55]. Contamination has also been found to affect the stability of the amorphous phases, for example Ti-Al powders [56] or Zr-Al powders [57].

c) Metastable phase formation by ball-milling

One of the main benefits of ball-milling is that it allows to alloy elements which do not alloy at normal equilibrium conditions or by conventional techniques [58]. Due to the high mechanical and thermal energy input, ball-milling is a non-equilibrium process and, therefore, stabilizes metastable phases at room temperature. The appearance of metastable phases is related with the possibility of avoiding the formation of the stable intermetallic compounds in the milling process as has been proved in a study by Koch et al [59]. It has been demonstrated that the phase selection during mechanical alloying is energetically determined. Usually, the phase with the lowest free energy is observed, exhibiting either an amorphous or a crystalline structure with a nanometer grain size. A broad practical experience supports

the theory: in several works the authors have reported successful attempts to stabilize a metastable phase by ball-milling. For example, Machio et al. [60] alloyed Ti with Mg, i.e. a ß-eutectoid element. Elemental powders of Ti and Mg were ball-milled for 20 hours under argon. As-milled powder consisted of a single bcc metastable ß-phase and the peaks in the XRD pattern were very broad suggesting a strong grain refinement and high lattice strain. In another study by Omran et al. [61] a metastable ß-type Ti-35Nb-2.5Sn alloy was synthesized by mechanical alloying during high energy ball-milling of elemental powders. Nb is a ß-stabilizing element and Sn has a neutral effect as an alloying element for Ti (see 2.2.1). After 1 and 4 hours the milled powder consisted of an α+ß phase mixture, but after 12 hours of milling only ß-phase peaks were visible in the XRD pattern. Zhou et al. [62] produced a Ti-35.4Nb alloy by ball-milling of elemental Ti and Nb powders. These powders with different nominal Nb mass concentrations of 12-45 wt.-% were blended using a planetary ball-mill for 2 hours. The compositions with higher Nb content represented an almost single metastable ß-phase after milling. There were still some traces of the α-phase present, but the intensity of α-phase peaks decreased with increasing milling time.

2.3.1.2 Basic principles of mechanical alloying

The process of ball-milling for mechanical alloying is schematically shown in Figure 13. A mixture of elemental powders is placed in the milling vial together with steel (or WC) balls in a protective inert gas atmosphere. For ball-milling different types of mills can be employed [52], but planetary ball-mills are most frequently used in laboratories. The size of the balls, the ball-to-powder weight ratio, the milling speed, the milling atmosphere, the milling duration and mode are the main variables of the ball-milling process that have a strong influence on the final product. During milling the vial rotates in reverse to the main rotation direction of the device and so the balls collide with each other and deform the powder particles. The intensity of the process depends on the chosen milling parameters.
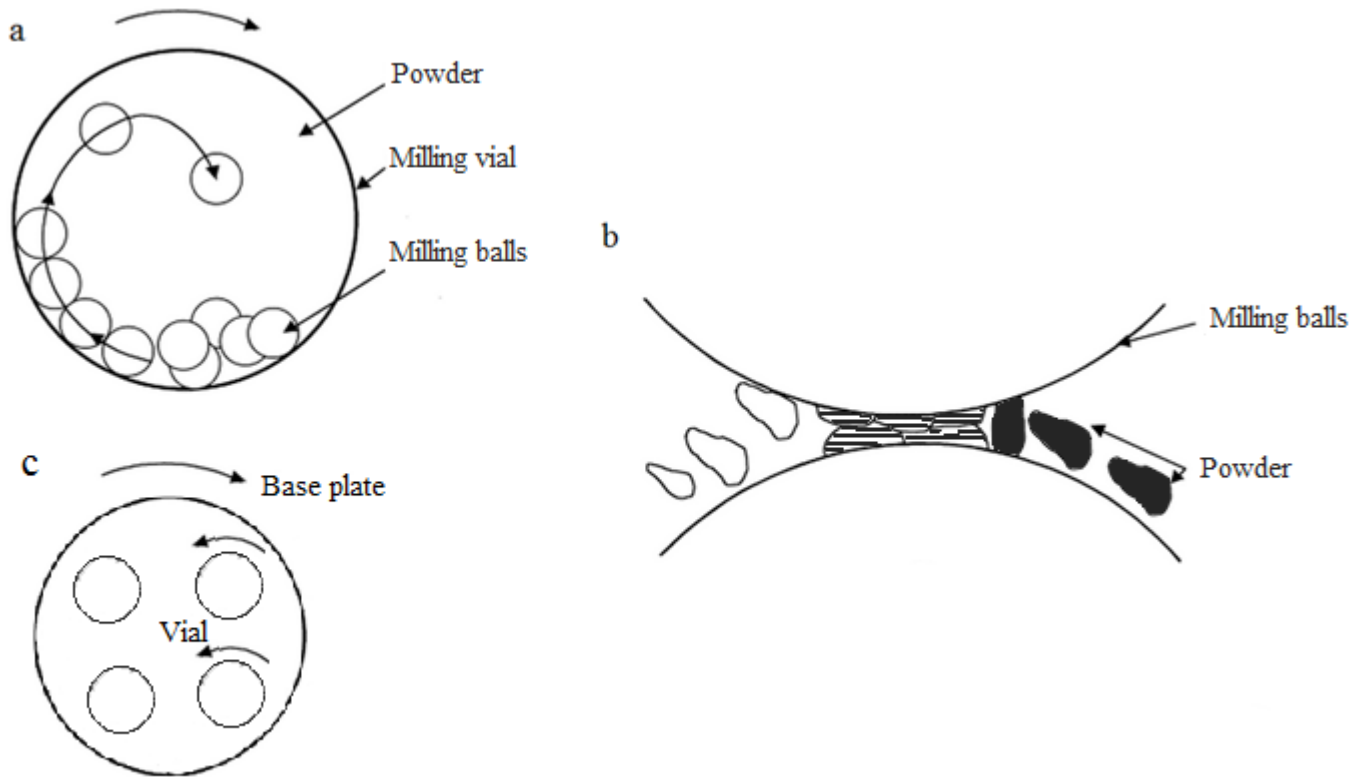
Figure 13: Schematic sketch of the process of ball-milling of metal powder (a) in a ball-mill, (b) ball-to-powder collision during mechanical alloying [63] and (c) the movements of base plate and vials.

During each collision the powder particles are submitted to severe plastic deformation: they are deformed, fractured and mutually cold welded. This process is repeated many times leading to new particles with a characteristic layered microstructure (Figure 14a) that is refined as the process progresses (Figure 14b, c). At the same time highly reactive surfaces are created and the concentration of defects (e.g. vacancies, dislocations, grain boundaries) in the starting crystalline phase progressively increases. Atomic mobility in the interfacial regions of the starting metals is therefore enhanced and an interdiffusion process, driven by the negative heat of mixing, enables alloying.

Figure 14: SEM images of Ti-50Nb powder after 2, 6 and 10 hours of milling [64].

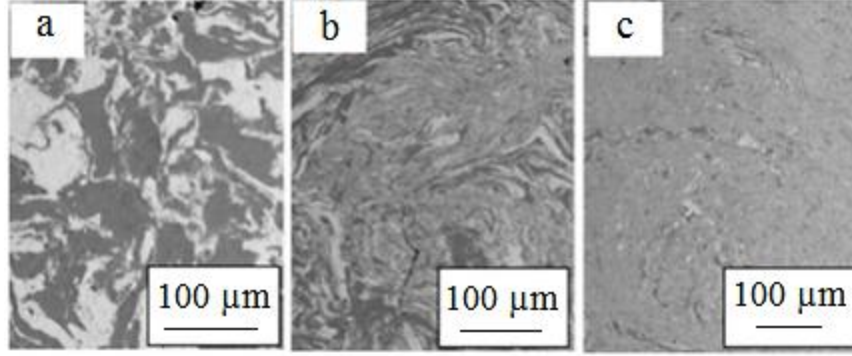Phase transformations can occur by solid-state reactions during ball-milling starting from crystalline elemental powders. In Figure 15 the paths of all possible reactions are taken into account together with the related Gibbs free energy changes and with timescale τ. A metastable phase is represented by an energy level G_{met} which is elevated relative to that of the relevant crystalline phases in equilibrium at G_x, i.e. the energy level of the starting elemental powders or that of competing equilibrium reaction products. In the course of the milling process in a first stage a higher energetic intermediate state G_0 is established (introduction of many lattice defects, formation of the metallic elemental layer systems in cold welded particles). Upon further milling, from the energetic viewpoint the stabilization of the lower energetic equilibrium phase should be favored. In order to avoid this and to stabilize the higher energetic metastable phase, the whole process must be strictly kinetically controlled via the reaction time, i.e. the transformation $\tau_{0 \to met}$ must be fast, but the further transformation rate $\tau_{met \to x}$ must be very slow.

The above consideration can be summarized with the following kinetic conditions:

$$\tau_{0 \to met} \ll \tau_{0 \to x} \tag{2}$$

$$\tau_{met \to x} \gg \tau_{0 \to met} \tag{3}$$

28

where $\tau_{0\rightarrow met}$ and $\tau_{0\rightarrow x}$ are the timescale for the metastable and stable phase formation starting from the initial stage G_0 whereas $\tau_{met\rightarrow x}$ corresponds to the phase transformation from metastable to a stable phase.
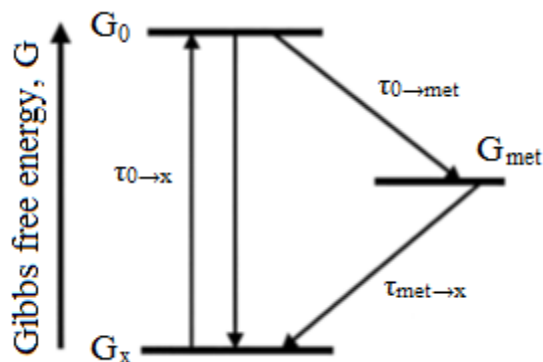
Figure 15: Schematic illustration of all possible reaction paths with the corresponding Gibbs free energy changes and timescale τ which can take place during the solid-state formation of a metastable phase [65].

2.3.1.3. Problems and challenges of ball-milling of Ti alloys

One of the main problems of ball-milling is a severe sticking of the powders to the milling tools. The powder yield is the amount of loose powder recovered from the container after ball-milling. It has been demonstrated, that with increasing milling time the yield decreases [66], which is a special big problem for ductile materials such as Ti. In a work by Bhattacharya et al. [67] high-energy ball-milling was employed to produce nanocrystalline Ti‑Al powders. During the ball-milling the authors faced the problem of severe sticking, which reduced the powder yield to almost zero. The effects of milling parameters such as milling tools, initial state of the powders and addition of process control agents (cyclohexane, stearic acid and titanium hydride) were investigated. The best results of 65-80% yield were obtained upon milling in the absence of process control agents in a WC vial and in a Cr‑steel vial. Nouri et al. [68] examined the influence of different contents and types of process control agents, i.e., stearic acid (SA) and ethylene-

bis-stearamide (EBS), on the microstructural evolution and characteristics of the α+ß Ti-16Sn-4Nb alloy. According to their results the addition of both SA and EBS led to a delay in the alloy formation during mechanical alloying and caused contamination of the material mainly with C and O. An optimum amount of 1 wt.-% of process control agent led to a good balance between cold welding and fracturing and, thus, favored the formation of the titanium alloy.

In some other works the authors used NaCl as an anti-sticking agent. It has been reported that NaCl does not decompose during ball-milling like organic agents and, thus, does not contaminate the powder with O and C. The authors mentioned that addition of 2 wt.-% NaCl was sufficient to overcome the sticking problem during ball-milling of Ti-Mg alloys [69]. In a work by Bahmanpour et al. [70] single phase Cu-Zn alloys were processed by high energy ball-milling of elemental powder at room temperature. NaCl was used to control the deformation process and to prevent cold welding of the powder to the milling media. It was found that 0.125 wt.-% of NaCl can effectively control the consolidation behavior of the powder and helps to overcome the cold welding of the powder to the milling media.

Another big problem of ball-milling is the contamination of the anticipated powder by different elements while milling. The most common contaminations are Fe (from the steel milling tools), O and C (are present in the milling atmosphere and occur after the decomposition of process control agents) [70]. But some authors suppose that in some cases the contaminations support the desired phase and that there would be no phase transformation when only pure metals would be present. hcp→fcc transformations were reported in Group IVB elements Ti, Zr and Hf upon mechanical milling. Seelam et al. [71] found that transformation was observed in powders milled under regular conditions and no such transformation was observed when the powders were milled in an ultrahigh purity atmosphere. Nouri et al. [72] have investigated the effect of the ball-milling time on the structural characteristics of a biomedical Ti-16Sn-4Nb alloy. The powder was synthesized using a high energy ball-mill for different periods of time. The

authors reported a growing percentage of contamination in the milled powder with increase of milling time. Thus, the O content in the powder milled for 1 hour was found to be 1.25 wt.-%, after 10 hours 2.15 wt.-% and after 20 hours 2.65 wt.-%. The amount of Fe grows as well, from 0.2 wt.-% at 1 hour, 0.41 wt.-% at 10 hours up to 0.47 wt.-% at 20 hours. It has been demonstrated that the contents of N, C and Cr grow with increasing milling time as well. It has been suggested that the contamination with O is mainly attributed to the leakage of air into an inadequately sealed container.

2.3.1.4. Other powder processing techniques

There are some other methods to produce metal alloy powders besides ball-milling. One of the most commonly used methods is gas-atomization. Atomization is a process of spraying a molten metal stream at moderate pressures. The principal method is to disintegrate a thin stream of molten metal by subjecting it to the impact of high energy jets of gas or liquid. Inert gases or air are used as gas environment, water is most commonly used as liquid environment. Powders, produced by this method have a relatively low amount of contaminations and a spherical shape (Figure 16a). By this method pure metals as well as alloys can be produced [41]. This is a non-equilibrium technique which enables very rapid cooling rates of 10^5 Ks^{-1} and can therefore stabilize metastable phases in the alloys.
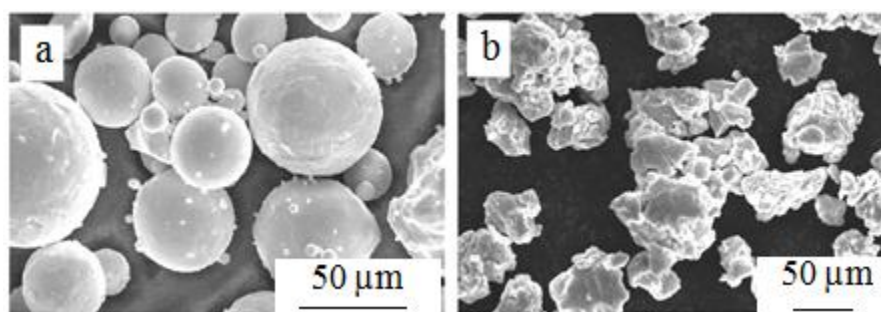

Figure 16: (a) Gas-atomized and (b) ball-milled powder morphology.

This method was successfully applied to yielding Ti powder particles of a typical spherical shape. Gas-atomized Ti powder was used for example in a study by Oh et al. [8] for the production of porous samples by loose powder sintering. Ahsan et al. [73] used commercial Ti-6Al-4V gas-atomized powder and a powder obtained by plasma rotating electrode (PREP) processes with a particle size of 45–105 μm. PREP is an advanced powder production technique, able to produce particles with near perfect spherical morphology. Ti-6Al-4V powders produced by both of these methods had an α+ß phase composition.

It has been reported on the production of gas-atomized Ti-45Nb and Ti-50Nb powders with a single ß-phase structure [74]. Powders produced by the gas-atomization process have high purity and relatively low compressibility and green strength because of their shape. This means that loose powder sintering of gas-atomized powders leads to relatively high porosity and low strength of the samples. Gas-atomized powder may be successfully compacted by hot-pressing, selective laser melting and so on. Loose powder sintering works better for powder particles with non-regular shape, for example ball-milled powders. High energy ball-milling of Ti with a proper addition of ß-stabilizing elements (Ti-35Nb-2.5Sn) resulted in a metastable ß-phase after 12 hours of milling as reported by Omran et al. [61]. Ball-milled powder is known to have a better compressibility and green strength due to its irregular shape, but a relatively low purity because of contaminating during the milling process (see chapter 2.3.1.3). A summary of various powder production methods and some properties of the produced powder is given in Table 2 [41]. The purity is an important aspect for powder that influences the mechanical properties of the compacted bodies (see 4.1.2). The highest purity corresponds to the powder produced by a gaseous reduction of solids, electrolytic deposition and carbonyl method. Gas-atomized powder has a relatively good purity as well. Ball-milled powder can be contaminated during the milling process and, therefore, has medium or low purity. The contamination level can be controlled by the milling parameters: milling media, speed, time, presence of milling agents and so on (see 2.3.1.1). Compressibility is an ability of the powder to be

compacted to high densities. Ball-milled and electrolytically deposited powder has the best compressibility and the gas atomized powder has the lowest compressibility. Green strength of spherically shaped powder particles is usually low. The highest green strength is typical for irregularly shaped or spongy powder particles, such as ball-milled powder or powder produced by gaseous reduction of solutions.

Table 2: Summary of various powder production methods and the powders properties [41].

Method	Purity	Particles shape	Compressibility	Green strength
Ball-milling	Medium	Irregular	High	Medium to high
Atomization	Relatively good	Irregular to smooth, rounded	Low to high	Low
Gaseous reduction of solids	Medium	Irregular, spongy	Medium	High to medium
Gaseous reduction of solutions	High	Irregular, spongy	Medium	High
Reduction with carbon	Medium	Irregular, spongy	Medium	Medium to high
Electrolytic deposition	High	Irregular, dendritic	High	Medium
Carbonyl method	High	Spherical	Medium	Low
Grinding	Medium	Flaky	Medium	Low

2.3.2. Sintering of porous metallic bodies

2.3.2.1. Sintering process - basic principles

Figure 17 shows a schematic illustration of the powder sintering process between two spherical powder particles. In Figure 17a two powder particles are brought in close contact with each other. They have a perfect spherical shape and are only contacting in one point. In Figure 17b the particles undergo necking but their centers have not moved closer together. Since the particle centers are still at the same distance apart, a dimensional change has not occurred.
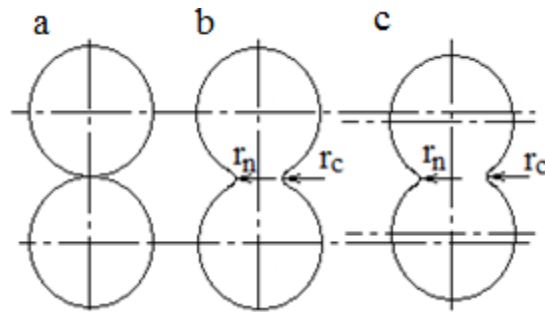
Figure 17: Sintering of spherical metallic particles in (a) close contact; (b) neck formation without overall shrinkage and (c) neck formation with shrinkage [75].

The situation in the second case (Figure 17c) is different. Here the particle centers have moved closer together. Hence, if these spherical particles are part of a larger powder mass, macroscopic shrinkage of the sintered body would have been observed. The neck formation between two particles is a necessary condition during sintering. The neck ensures the bonding between powder particles: the stronger it is the higher is the strength of the porous body. If the radius of the neck between two particles r_n is much larger than the radius of curvature r_c, then the stress σ acting in the neck (whose magnitude is related to the surface tension γ) is approximately:

$$\sigma = \frac{\gamma}{r_c} \qquad (4)$$

This stress is directed outwards (tensile stress) from the neck. One result of this stress in the neck is that the equilibrium vapor pressure will be slightly larger above the neck than over the particle surface remote from the neck. Because of this difference in equilibrium vapor pressure it is possible for the material to be transported by evaporation from some parts of the particle surface and to condensate on the neck with the result that the neck between the particles will grow. In summary, it can be concluded that at the junction between two particles a stress exists which is acting in a manner to make the neck grow [75].

The driving force for the sintering is a reduction of the total interfacial energy. The total interfacial energy of a powder compact is expressed as γA, where γ is the surface (interface) energy and A is the total surface (interface) area of the compact. The reduction of the total energy can be expressed as:

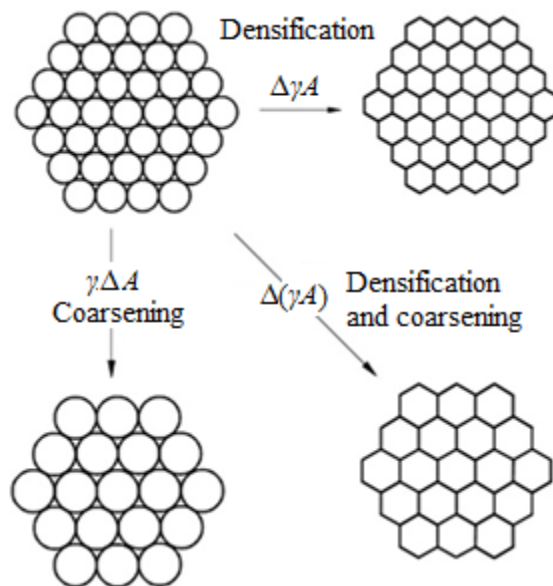$$\Delta(\gamma A) = \Delta\gamma A + \gamma\Delta A \tag{5}$$

Figure 18: Basic phenomena occurring during sintering under the driving force of sintering $\Delta(\gamma A)$ [76].

Here, the change in the interfacial energy ($\Delta\gamma$) is due to densification and the change in interfacial area is due to grain coarsening. For solid state sintering, $\Delta\gamma$ is related to the replacement of solid/vapor interfaces (surfaces) by solid/solid interfaces. As schematically shown in Figure 18, the reduction in total energy occurs via densification and grain growth, the basic phenomena of sintering.

The final properties of the sintered body such as strength and stiffness will strongly depend on the interparticle bonding and thus, on the chosen sintering route and parameters. In addition to the bonding formation, sintering can also lead to chemical changes in the powder, dimensional changes, relief of internal stresses, phase transformations and alloying process [74]. There are several main parameters that influence the sintering process:

1. Sintering temperature: increasing of the sintering temperature increases the rate of all the processes that take place during sintering.

2. Sintering time: it has been noticed that the degree of sintering increases with increasing of sintering time.

3. Sintering atmosphere: sintering can be carried out in inert gases (to avoid powder oxidation during sintering) or in reactive media like oxygen [77].

Besides that during the sintering process the powder particles can roll and rotate as proven by experimental data and DEM computer simulations in a study by Kieback et al. [78].

2.3.2.2. Sintering techniques

a) Loose metal powder sintering

Loose powder sintering is the simplest method of compaction of metal powders and it is used for manufacturing of highly porous metal bodies. Basically, the powder is poured or vibrated into a mould

which is then heated to the sintering temperature under protective atmosphere without any applied mechanical load. The form and the complexity of shape which can be achieved by this method depend to a large extend on the flow characteristics of the powder. In this respect the process is analogous to metal casting as well as to the fact that the component must be removable from the mould after sintering. As sintering of metal powders usually occurs at high temperatures, powder contaminations may become a serious problem. The main source of contaminations is the sintering atmosphere.

The powder sintering is carried out in a mould which is heated to a relatively high temperature. It is important that the component must be removable from the mould after the sintering is finished. The characteristics required for the mould material are: (i) it should be easily machineable or formable into a required shape; (ii) it should withstand the sintering temperature without appreciable deformation; (iii) it should not weld to the powder during sintering. For most applications machined or welded metal moulds are used although graphite may also be employed where no reaction with the powder is likely [75].

This method results in very porous metallic bodies with mostly interconnected micro-porosity. The amount of porosity can be controlled by the applied temperature in a narrow range. Besides that porosity gradients can be created by varying the powder particle size [79]. Solid bodies made by loose powder sintering usually demonstrate relatively low values for strength and fatigue strength as well as for Young´s modulus and wear resistance. For example Ti powder with a particle size in the range of 420-500 µm was loose sintered to a porosity of 41.5 % in a study by Asaoka et al. [80]. These samples had a relatively low Young´s modulus of 5.2-5.5 GPa and a compression strength of 182±34 MPa.

b) Loose metal powder hot-pressing

Hot-pressing is one of the methods of pressure assisted sintering. The pressure is applied to dense packed powder particles; it is transmitted through the powder as a set of forces acting across the particle contacts.

The deformation at these contacts is at first elastic, but as the pressure rises, the contact forces increase, causing plastic yielding and expanding the points of contact into contact areas [81].

By hot-pressing of loose metal powders it is possible to form dense compacts with a high density. Densification is determined by a significant deformation of the particle contacts. The process occurs at elevated temperatures. The densification behavior of hot-pressed powders changes significantly when sintering is pressure-assisted. The final density depends on the compaction pressure applied during the heating cycle, pressing temperature and holding time. In general, with increasing compaction pressure, pore volume fraction and pore size decrease dramatically. With increasing temperature the density of the final samples increases [82].

The microstructure of a hot-pressed sample influences the mechanical properties mainly via the grain size. A significant grain growth occurs often at high process temperatures or at long holding times. The heating regime correlates to the phase composition of the alloy as well. For example, stabilizing of martensitic α´´ phase or metastable ß-phase in Ti-Nb alloys demands fast cooling rates as discussed in section 2.2.2.

The hot-pressing technique has certain disadvantages. For most metal powders the main problem is oxidation of the particles. It may be necessary to maintain a protective atmosphere not only during heating and pressing but also during cooling and after ejection. The use of elevated temperatures limits the choice of die materials. High speed steel dies will operate satisfactorily only up to 500°C, but die wear increases rapidly above this temperature. Above 500°C it is necessary to use the superalloys based on Ni or Co or cemented carbides. Above 1000°C the field is limited by graphite, oxide, uncemented carbide formation [75].

c) Sintering with space-holders

The space-holder material allows to control the pore size and shape and therefore, a microscopic pore volume fraction of a sintered sample. For this method the metallic powder is mixed with space-holder particles to obtain the desired porosity fraction. Then the mixture is compacted by cold or hot-pressing and sintered by different methods and routes. Finally, the space-holder is removed. Some of the space-holder evaporate at elevated temperatures during the sintering step (carbamide, polymer granules, Mg) or are washed out by water (NaCl or sugar). By using different shapes of the space-holder particles it is possible to produce samples with different pore shapes such as cubic, spherical or irregular. Carbamides or ammonium hydrogen carbonates are among the most commonly used space-holder materials, but they have a low dissociation temperature and their decomposition products may cause oxidation and degradation of the final porous bodies [45]. Mg is a biocompatible material, it has a relatively high evaporation temperature (1107 °C) and some residual Mg traces in porous bodies will not limit their biocompatibility [16]. NaCl can be easily dissolved in body fluids and in small quantities it is not toxic for the human body [83]. Besides that NaCl has a high melting temperature (801°C) and can be used in porous sample production by a wide variety of methods.

For sintered porous materials fabricated by using space-holder there are two types of porosity (see Figure 19) as listed below:

1. Macro-pores – these are formed by the space-holder particles, which determine the size and morphology of these large pores.

2. Micro-pores (typical size range <10 µm) – that are formed in between the metallic powder particles (like in the loose sintered powder). The size and morphology of these small pores are determined by the size of the constituent powder particles and the level of compression and sintering [84].
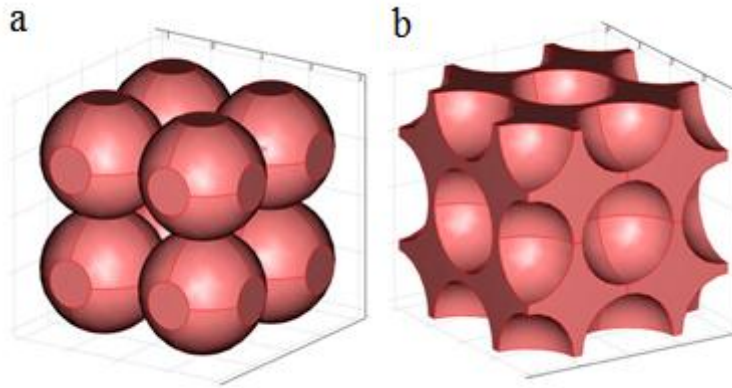
Figure 19: Porosity in metallic bodies processed by sintering of powders with space-holder material (a) micro-porosity in between the sintered powder particles and (b) macro-porosity after the space-holder particle removal [84].

Sintering with space-holders results in macro-porosity, that significantly reduces Young´s modulus as well as the strength of the samples. The micro-porosity can be controlled via process parameters like temperature, pressure, holding time as well as by the powder particle shape and size. By this method it is possible to control the shape of the pores by choosing space-holder materials with a proper shape of the particles. Nevertheless, the space-holders can be another source of contamination for the final product.

Processing porous bodies by a space-holder technique is widely represented in the literature. In a work by Aydogmus et al. [44] homogeneous TiNi alloys having porosities in the range 59–81% were produced using Mg powder as space-holder. Spherical commercial gas-atomized TiNi powders and spherical Mg powders were used as starting materials. These powders (50%, 60%, 70%, and 80% Mg by volume, balance TiNi) were mixed for 30 minutes using a 5 wt.-% polyvinyl alcohol (PVA) solution as the binder prior to compaction. After that the samples were loosely sintered at 1100°C for 1 hour for all the samples

produced. The processed alloys exhibited interconnected open pores that replicated a spherical shape of Mg particles (see Figure 11a) and had average pore sizes of around 400 μm.

Niu et al. [85] used carbamide particles as space-holders. Pure Ti powder with a mean particle size of 44‑74 μm and an irregular particle shape was used. The spherical carbamide particles in the size range of 200‑600 μm were chosen as the space-holder material. The size of the spacer particles was selected according to empirical investigations. To increase the green strength of powder compacts, Ti powders were mixed with the binder polyethylene glycol. Based on the differential thermal analysis of the carbamide and the sintering process of Ti powders, the heat treatment includes three steps, i.e. at 200° C for 3 hours, 350° C for 3 hours and 1250° C for 3 hour, followed by furnace cooling. The final alloy had a porosity range of 55‑75% and a pore size distribution of 300‑500 μm. Young´s modulus of these samples was 3-6.4 GPa and the plateau stress varied between 10 and 35 MPa.

Gao et al. [86] have demonstrated a successful route to produce porous Ti-Mo samples utilizing NH_4HCO_3 powder as a space-holder. 25 wt.-% of NH_4HCO_3 was added to blended Ti–10Mo metallic powder, cold pressed and then sintered. The space-holder particles were evaporated during sintering at 1200°C for 5 hours. Porous samples had a low Young´s modulus of 20 GPa and a compression strength of 174 MPa. A study by Lee et al. describes an attempt to produce directional pores [87]. Commercial Ti-6Al-4V powder was blended with 50 % Cu and warm extruded. The Young´s modulus of these samples was determined as 4 GPa and a compression strength as 257 MPa.

2.3.3. Preparation and mechanical properties of Ti-based porous materials

As mentioned above, the porosity and particle interconnections as well as the phase composition and the grain size strongly determine the mechanical properties of Ti alloys. Examples demonstrating the correlation between the porosity, the microstructure and the mechanical properties are given below.

Commercial gas‑atomized Ti‑6Al‑4V powders had particle sizes in the range from 45 to 250 μm with an average particle size of 107 μm. Magnesium powder with a wide range of particle size distribution (300‑1500 μm) and an average particle size of 660 μm was used as space-holder material. Ti‑6Al‑4V/Mg powder mixtures containing 30, 40, 50, 60 and 70 vol.-% Mg were at first green compacted (cold pressed) at various pressures (375, 510, 750 and 1125 MPa) and then sintered at temperatures between 1000 and 1250°C with 50°C intervals. The final total porosity of the foams manufactured by evaporation of the space-holder particles from Ti-6Al-4V/Mg compacts varied in the range of about 43 to 64%. The elastic modulus and the yield strength determined in compression tests were in the ranges of 1.42–14.7 GPa and 28.2–150 MPa, respectively. The mechanical properties of the foams were found to depend on microporous cell wall properties, which in turn depend on the neck size between the powder particles. The phase composition depends on the temperature of the process and on the cooling rate of the samples. Slow cooling of porous Ti–6Al–4V samples from the high temperature β-phase region resulted in a diffusion controlled phase transformation leading to a lamellar type of Widmanstätten structure containing α-platelets and β-laths.

Lee et al. [86] demonstrated a powder metallurgy synthesis route for porous Ti–6Al–4V structures comprising the consolidation of Ti–6Al–4V alloy powders by warm extrusion and the characterization of mechanical properties of these samples. Commercial gas-atomized Ti–6Al–4V powders with a mean particle size of <44 μm were blended with 50 vol.-% of Cu powders with particle size between 20 and 44 μm. Cylindrical precursor rods were produced by warm extrusion of the blended powders at 1076°C and 1146°C. Porous Ti–6Al–4V foams were obtained through dissolution of the Cu phase in the extruded precursor by immersion into a 50 : 50 concentrated HNO_3 : H_2O solution. After a warm extrusion process the pores had a directional orientation shown in Figure 20. The foam processed at 1146°C exhibits an

average maximum strength of 257 MPa and 82% strain. The foam processed at 1076°C has a maximum strength of only around 50 MPa and a strain of 0.1%.
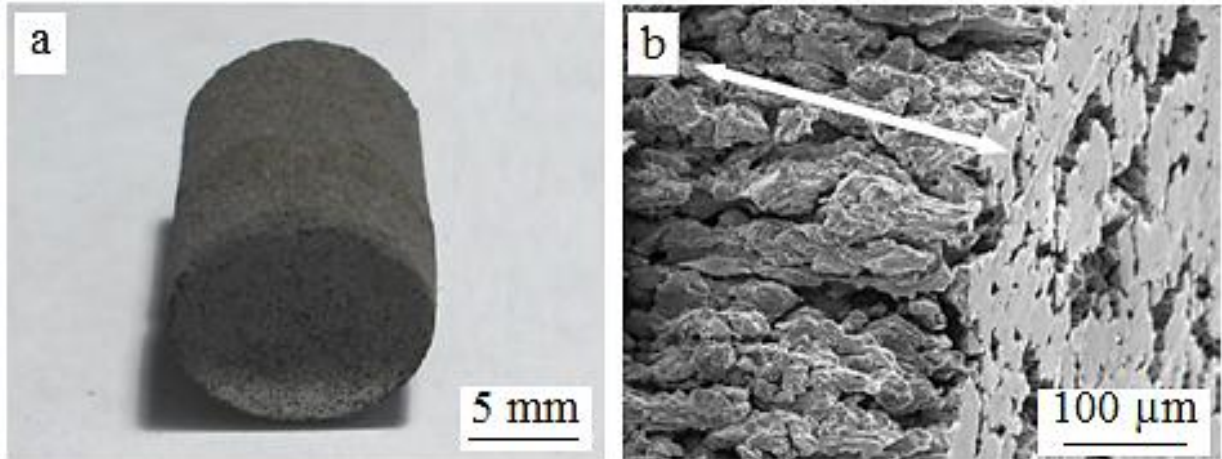

Figure 20: Macro- and microstructural images of a Ti–6Al–4V foam prepared at 1146°C. The arrows on the images show the extrusion direction. (a) Outer shape of as-dissolved Ti–6Al–4V foam, (b) detailed microstructure of Ti–6Al–4V foam [87].

The Young´s modulus was only determined for a foam processed at 1146°C and has a value of 4 GPa at a porosity of 50% (compared to 117 GPa for "solid" cast Ti-6Al-4V [88].

Porous ß-type Ti-18Nb-4Sn alloy samples were prepared by a powder metallurgy technique in a work by Xiong et al [89]. Elemental metal powders of Ti, Nb and Sn were mechanically alloyed by ball-milling for 2 hours. The ball-milled Ti–18Nb–4Sn powder (single ß-type phase of as-milled powder) was mixed with ammonium hydrogen carbonate (NH_4HCO_3), which was used as space-holder material. The mixture of Ti‑18Nb‑4Sn powder and NH_4HCO_3 was cold pressed into green compacts in a hydraulic press. The sintering was performed in two steps: the first step was carried out at 175°C for 2 hours to burn the space-holder and in the second step the compacts were heated to 1200°C and held for 3 hours to sinter the remaining metal powder into a porous product. For comparison, porous Ti–18Nb–4Sn products with four

different porosities, i.e. 30, 40, 50 and 60% as well as dense Ti‑18Nb‑4Sn alloy bodies (3% porosity) were mechanically tested in compression. After sintering, α-Ti and β-Ti phases formed in the sintered porous Ti–18Nb–4Sn sample, but no elemental Ti, Nb and Sn was detectable. The elastic modulus determined from the initial linear slope of the stress–strain curve was 75.8 GPa, which is higher than the previously reported value of a similar Ti–Nb–Sn alloy prepared by ingot metallurgy. The elastic moduli of porous Ti–18Nb–4Sn alloys with a porosity varying from 30 to 60% were measured to be 33.2-10.8 GPa, and their compressive strengths were 420–112 MPa.

To sum up the theoretical and experimental data reported in literature it can be stated that porous Ti alloys have a relatively low Young´s modulus and strength compared to the fully dense alloys. The mechanical properties of the samples can be controlled by the volume fraction of porosity in a wide range. There are many ways to produce porous samples, but the simplest and most commonly used ones are loose powder sintering, hot-pressing and sintering with a space-holder material. Another important aspect that allows to control the mechanical behavior of the alloy is its alloy composition and microstructure. So far, a variety of prominent examples for preparation and characterization of porous α-type (Ti) or (α+ß)-type (Ti-6Al-4V) samples are reported. However, studies on porous ß-type Ti alloys are still very scarce. Ti-Nb alloys are of particular interest for biomedical applications since they are composed only of bio compatible elements. In the Ti-Nb system there are several phases that can be stabilized at room temperature. From empirical studies with molten and rapidly quenched alloys it is known that the metastable ß-phase has the lowest Young´s modulus (≈62 GPa) among all the phases in Ti-Nb alloys and a good ductility. A single metastable ß-phase state can be obtained at 40-45wt.-% Nb. The challenges of the powder metallurgical approach for the production of porous low modulus Ti-40Nb alloy samples are to produce firstly ß-phase Ti-40Nb powder mainly by solid state processing and to further demonstrate that the heat treatments do not only sinter the powder particles but also preserve the

state of a single ß-phase in an alloy sample at room temperature. For that purpose suitable temperature, holding times and cooling rates must be utilized.

The Ti-Nb powder can be produced by different ways. A reliable and commonly used method is a ball-milling technique. According to the theoretical background of ball-milling and some literature data it appears to be possible to form an alloy from elemental Ti and Nb powders and to stabilize a metastable ß-phase. But ball-milling has certain disadvantages. The first challenge is overcoming the severe powder sticking to the milling tools. The commonly used organic agents used to overcome the sticking decompose during the milling process and contaminate the powder with O, C and N. NaCl is another promising anti-sticking agent that was used in several works with different powder types and can be used to replace the traditional organic agents. The second challenge is to reduce the contamination of the powder with O during milling that comes mostly from the atmosphere. The long milling time results in the saturation of the Ti powder with O which is a strong α-phase stabilizer. One of the possible ways to reduce the O content is to adjust the milling parameters.

Finally, the challenge of the present work was to produce porous ß-type Ti-40Nb samples with a Young´s modulus comparable to that of a human bone (≈20 GPa) and a strength of ≈150 MPa. The desired porosity should be interconnected and have dimensions of 100-400μm. In the present work several successful methods to produce single ß-phase Ti-40Nb porous alloy with low Young´s modulus are discussed.

Chapter 3

Experimental details

3.1. Materials processing

3.1.1. Ball-milling and powder processing

The starting powders for porous sample processing were produced by ball-milling (see section 3.1.1.1). Two types of commercial Ti powders were used as starting material: (i) Johnson Matthey GmbH (purity 99.4%, <100 mesh, irregular shape) and (ii) gas-atomized Ti powder produced by TLC Technik (purity 99.2%, < 100 mesh, spherically shape). For all experiments Nb powder from Johnson Matthey GmbH (purity 99.8%, 325 mesh, irregularly shaped) was employed. The starting amount of O in powder measured by CGHE method (see section 3.2.4) was 0.4 wt.-% for (i) Ti powder and 0.137 wt.-% for (ii) Ti powder. The elemental powders were mixed under high purity argon atmosphere (H_2O <0.5, O_2<0.5) to a selected composition of Ti-40Nb or Ti-45Nb. The milling process was carried out under argon using a Retsch PM 400 planetary ball-mill. The material used for the steel vials and balls was plain carbon steel C15. For all milling experiments the ball diameter was 10 mm and the ball-to-powder ratio was 20:1. There were two sets of milling parameters used for different powder batches. In the first set of experiments the milling speed was 200 rpm and the milling was stopped every 10 hours to take some powder for tests (continuous mode). In the second set of experiments the milling speed was 250 rpm and the milling was interrupted every 15 minutes for 15 minutes to let the vials cool down (interval mode). Ti-40Nb (milled from atomized Ti powder) and Ti-45Nb (milled from atomized Ti-45Nb powder) were submitted to the interrupted milling mode. The total milling time was in all cases 40 hours. To prevent oxygen contamination, all steps were carried out in a glove box under inert gas atmosphere.

Ti-45Nb gas-atomized powder was ordered from TLC Technik. The powder was sieved to a size smaller than 20 µm and then milled in order to change the shape of the particles from spherical to irregular because irregularly shaped powder show a much better compressibility and green strength than the spherically shaped ones (see 2.3.1.4. and Table 2). The same vials and balls were used for the milling process. A continuous milling mode was used in this experiment.

The different starting powders and milling parameters are summarized in Table 3. The Ti-40Nb alloy composition with irregular Ti as a starting powder was only milled in continuous mode because the oxygen content in as-milled powder (around 1.7 wt.-%) was way too high compared to the allowed O content of 0.4 wt.-% for biomedical alloys [90]. The Ti-40Nb composition with spherical Ti powder as starting powder was milled in continuous mode and, in a second attempt, in interval mode. The interval mode is more gentle and thus the powder is less contaminated with oxygen and other elements. At continuous mode the oxygen content of this powder was 0.88 wt.-%. To further reduce this value a the second attempt (with interval milling) was carried out. Gas-atomized Ti-45Nb powder had low oxygen content and the milling was carried out just for 20 hours. That's why the milling mode was chosen to be continuous.

Table 3: Summary of the milling parameters and milling modes used for ball-milling of Ti-40Nb and Ti-45Nb elemental and Ti-45Nb gas-atomized powders.

	Ti-40Nb irregular Ti powder	Ti-40Nb atomized Ti powder	Ti-45Nb atomized Ti powder	Ti-45Nb atomized Ti-45Nb powder
Speed, rpm	200	200/250	250	200
Milling mode	continuous	continuous / interval	interval	continuous
Milling time	40 hours	40 hours	40 hours	20 hours

To avoid powder sticking to the milling tools NaCl powder was used as an anti-sticking agent. Different amounts of NaCl were added to the vial prior to milling, i.e. 0.25, 0.5, 1, 1.5 and 2 wt.-%. For a comparison milling without any anti-sticking agent was also carried out. The milling environment has no humidity and thus, no corrosion occurs during milling.

3.1.2. Porous sample production

Compaction without space-holders

The first route to produce porous ß-type Ti-Nb samples was loose powder sintering. The ball-milled Ti-40Nb alloy (produced from elemental Nb and elemental irregular-shaped Ti) powder was at first cold-pressed using a Weber-Pressen PW 100 E hot-press. Powder samples of 3 grams were pressed in a 10^{-4} vacuum atmosphere for 90 minutes with a pressure of 300, 420, 540 and 700 MPa at room temperature. After that the green samples were placed in argon-filled quartz tubes. The compacts were sintered at a temperature of 1000°C for 4 hours and then water-quenched.

For comparison the same powder was compacted by hot-pressing (see section 2.3.2.2.b). 3 grams of powder were placed in a hot-press chamber and compacted for 30 minutes at a temperature of 600°C with

a pressure of 700 MPa. To avoid oxidation of the powder the hot compaction was processed under vacuum. Then the compacts were slowly cooled down inside the hot-press. After that some samples were cut and submitted to compression tests. Other samples were sealed in argon-filled quartz tubes, sintered for 4 hours at 1000°C, water-quenched and then cut and submitted to compression tests.
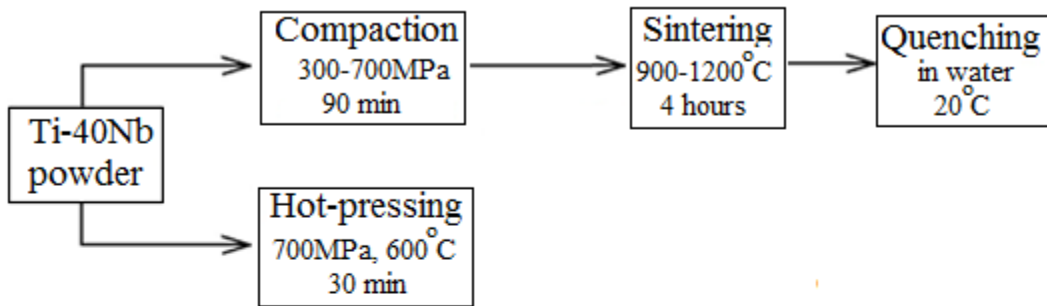
Space-holder methods

Mg or NaCl particles were sieved to obtain a size range of 100…300 µm and used in the following as space-holder materials. Ti-40Nb powder (produced from elemental Nb and elemental irregular-shaped Ti as well as the powder produced with spherical Ti) was mixed with space-holders to obtain the anticipated porosity of 50…80%. The calculation of porosity was based on the density of NaCl (2.125 g/cm^3) and Mg (2.32 g/cm^3) and the density of cast Ti-40Nb alloy of ≈5.5 g/cm^3. This mixture was pressed to green samples in a 10^{-4} vacuum atmosphere for 90 minutes with a pressure of 700 MPa at room temperature. After that the samples were sealed in argon filled quartz tubes, sintered at 1000°C for 4 hours and water quenched. Mg particles were evaporated during sintering. NaCl particles were dissolved by immersion in water at 80°C for 4 hours.

For comparison another series of samples was produced from the same powders by hot-pressing with space-holders. Ti-40Nb alloy powders were mixed with Mg or NaCl powder. The mixture was compacted in a hot-press for 30 minutes at 600°C with a pressure of 700 MPa in vacuum atmosphere. Then the compacts were slowly cooled inside the hot-press chamber. After that the samples were sealed in argon-filled quartz tubes and sintered for 4 hours at 1000°C and water-quenched.

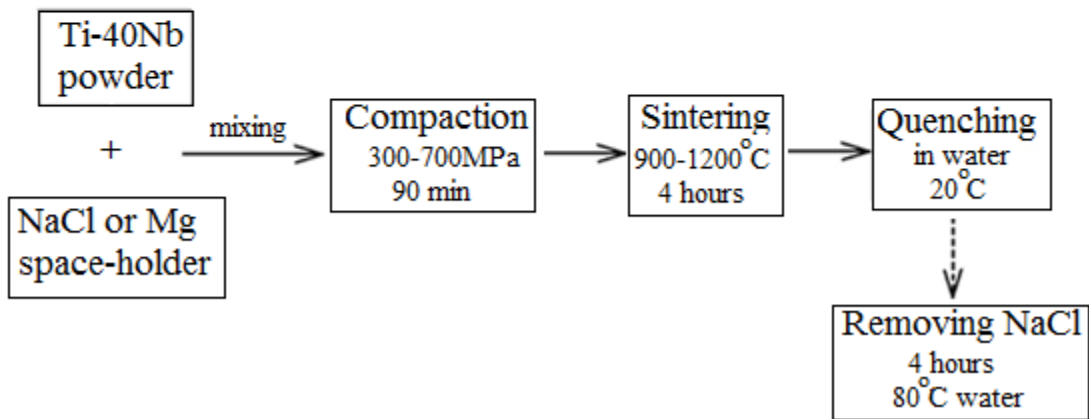All the compaction routes are represented schematically in Figure 21.

Figure 21: Porous Ti-40Nb alloy samples processing routes.

3.1.3. Surface modifications

Electrodeposition of hydroxyapatite coatings

A popular method for surface modification of biomedical materials is hydroxyapatite (HAP) coating. Compared with physical methods, chemical treatment is believed to be more suitable for complex surface morphologies such as porous structures, because it allows the liquid medium a full access to the outer and inner surfaces. Three different types of samples were prepared: porous Ti-40Nb samples made with NaCl as space-holder, porous Ti-40Nb samples made with Mg as space-holder and reference Ti-40Nb samples made by the loose powder sintering route. For the porous sample production the Ti-40Nb powder was green-compacted at a pressure of 700 MPa for 2 hours, then sealed in quartz tubes filled with argon, sintered for 2 hours at 1000°C and water quenched. NaCl was removed by immersing the samples in water at 80°C for 4 hours. Mg was evaporated during sintering. To make reference samples Ti-40Nb powder was green compacted at a pressure of 700 MPa for 2 hours, then sealed in quartz tubes filled with argon, sintered for 2 hours at 1000°C and water quenched The porosity of samples processed with Mg was 50% and that of samples processed with NaCl was 60%. Before coating, the samples were cleaned with distilled water and ethanol in an ultrasonic bath. Ti-40Nb reference samples were polished incrementally with silicon carbide paper from grit 320 to 4000 and cleaned with ethanol and distilled water in an ultrasonic bath for 10 minutes.

The electrodeposition experiments were carried out by A. Chivu (Dept. of Materials Science and Engineering, Politehnica University of Bucharest, Romania) in the IFW Dresden. The electrochemical deposition of HAP was carried out using a Solatron SI 1287 electrochemical interface connected to a three-electrode cell, with the sample as a working electrode, a platinum net as a counter electrode and a saturated calomel electrode (E(SCE)=241 mV vs. SHE) as reference. A Ti-40Nb compact acted as

working electrode and was electrically connected at one end and directly immersed into the solution. The electrolyte solution used for the electrodeposition of HAP was based on $Ca(NO_3)_2$ and $NH_4H_2PO_4$ powders which were dissolved in distilled water. Two types of solutions were prepared: electrolyte 1, 0.61 mMCa$(NO_3)_2$ and 0.36 mM $NH_4H_2PO_4$ with a pH value of 4.5 and electrolyte 2, 1.22 mMCa$(NO_3)_2$ and 0.72 mM $NH_4H_2PO_4$ with a pH value of 6. A potentiostatic mode was applied with a cathodic potential of -1 V versus SCE up to 3 hours. In addition, stirring of the electrolyte was carried out and the temperature was maintained at 620°C. Porous samples were coated for 1, 2 and 3 hours in electrolyte 1 and for 3 hours in electrolyte 2. Reference samples were coated for 3 hours in electrolyte 1 and for 3 hours in electrolyte 2. After deposition the samples were rinsed in distilled water and then dried at 645°C for 24 hours.

3.2. Characterization methods

3.2.1. X-Ray diffraction

Structural characterization of powder samples (see section 4.1) and compacted samples (see section 4.2) as well as HAP coating characterization (see section 4.3) was carried out using the Brucker D8 X-ray diffractometer with Co K_α radiation (XRD). The powder samples were attached to the PVC sample holder with a zapon lacquer. Both the fixing agent and the sample holders do not interfere with the measurements performed in a scanning range according to a work by N. Schlorke-de Boer [91]. All the XRD measurements were carried out in the angle range of 30-140° (2θ) with steps of 0.05° and a measuring time of 2 seconds per step.

For the interpretation of XRD data an XPert software was used. The lattice parameters and phase correlations were evaluated with the same software using a LeBail profile fitting procedure. To analyze of the grain size from XRD patterns a Debye-Scherrer method was applied.

The Debye-Scherrer equation allows to evaluate a mean grain size from the XRD patterns and can be written as:

$$\tau = \frac{K \cdot \lambda}{\beta \cdot \cos \theta} \tag{6}$$

 where K is a shape factor, λ - XRD wavelength (for the present study 1.7892 Å), β - line broadening at full width at half maximum intensity (FWHM), θ - the Bragg angle [92].

3.2.2. Transmission electron microscopy (TEM)

The samples for transmission electron microscopy were prepared by Dina Lohse (IFW Dresden). Powder samples were prepared by ion milling. For the mechanical thinning of the powder samples the powders were first embedded into epoxy resin Gatan G1 with a powder-to-epoxy volume ratio of 2:3. Then the embedded samples were heated to 130°C and held for 30 minutes. After that the samples were ultrasonically cut to a thickness of 3 mm, and then grinded and polished using a Phoenix 4000 grinding-polishing machine and SiC grinding paper. For further thinning the samples were ion milled with Ar ions. Single-sided low-angle ion milling was carried out in a Gatan PIPS. The ion energy was set at 3.5 keV.

Sintered bulk samples were prepared by focused ion beam (FIB) technique using a Gemini 1540 XB cross-beam machine at 30-keV Ga ion energy. To protect the lamella against the ion beam, a Pt layer was deposited at the front side. To keep the thin sample stable, some thick support bars were left in between very thin windows. The sample was attached to a 3 mm M-shaped sample-holder and the thinning was stopped when holes appeared in the lamella.

TEM studies were carried out by Matthias Bönisch (IFW Dresden). For TEM, a FEI Tecnai F30 instrument operated at 300 kV and equipped with Schottky field emitter, super-twin objective lens,

STEM unit, EDAX EDAMIII energy-dispersive X-ray spectrometer, and Gatan GIF200 imaging energy filter was employed.

3.2.3. Scanning electron microscopy (SEM)

Morphological characterization of the powder particles was performed using a scanning electron microscope Gemini 1530 SEM. The cathode voltage varied from 5 to 10 kV with a working distance of about 10 mm. The powder samples were embedded into Epofix cold-setting embedding resin with an addition of carbon powder to make the samples conductive. The proportion of carbon powder to embedding resin was 1:1. Embedded samples were left to dry for 8 hours and then grinded and polished on a Phoenix Beta grinding-polishing machine with SiC paper with a roughness from 800 to 4000. Sintered bulk samples were cut to discs with a diameter of 10 mm and a thickness of 2 mm on an Accutom-50 cutting device. For cutting, a 10S15 cutting disc was used with a rotating speed of 2000 rpm and a linear speed of 0.05 mm per second. After cutting the samples were grinded and polished using a Phoenix Beta grinding-polishing machine with SiC paper with a roughness from 800 to 4000.

Energy-dispersive X-ray spectroscopy measurements (EDX) were carried out using a Jeol 6400 SEM being equipped with both a backscattered electron (BSE) detector and an EDX detector (by Noran systems) for compositional analyses. The samples were prepared in the same way as for the SEM. EDX measurements were performed with a cathode voltage of 8-11 kV.

3.2.4. Chemical analysis

Chemical analysis was performed by Dr. Wolfgang Gruner and Cornelia Geringswald (IFW Dresden). The oxygen content in the as-delivered (irregular- and spherical-shaped Ti, gas-atomized Ti-45Nb powder) and as-milled powder (Ti-40Nb powder made of elemental irregularly and spherically shaped Ti, milled gas-atomized Ti-45Nb powder) was determined by carrier gas hot extraction (CGHE). The materials were encapsulated into a Sn capsule inside a glove box with an Ar atmosphere (H2O<0.5 ppm,

O2<0.5 ppm). This capsule with powder was taken out from the glove box and sealed inside of a Ni capsule. A commercial nitrogen/oxygen analyzer TC-436-DR (Leco, USA) was used. The measurement probe was placed into a heated graphite crucible and heated up to about 2500°C in streaming helium gas, and the reaction of the oxygen from the material with carbon from the crucible occurs according to:

$$MeO + C \rightarrow Me + CO \tag{7}$$

The evolved CO is detected by an IR-detector and its amount is quantified against a reference material.

3.2.5. Micro-Computed-Tomography (µCT)

In µCT the X-rays create a cross-section of a 3D object and recreate it into a virtual 3D model of an object. It is a non-destructive method. The principle scheme of the measurements is presented in Figure 22. The sample is placed in a holder that rotates between the X-Ray tube and the detector. Together, the tube and the detector scan across the subject, sweeping the narrow x-ray beam through the sample. During translational motion, measurements of x-ray transmission through the subject are made by the detector at many locations. After the scanning is finished there are hundreds or thousands of images that can be put together to form a 3D image of a sample (reconstruction).
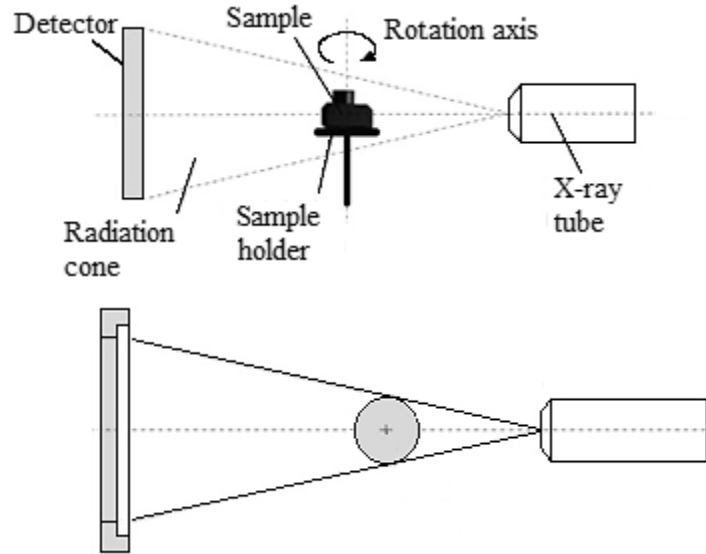
Figure 22: Principle scheme of a µCT measurement.

The µCT measurements were performed at Dresden University of Technology, Center of Microtechnical Manufacturing, by Dr.-Ing. Martin Oppermann. The system used was a computed tomograph Nanotom S from GE Company. Porous Ti-40Nb samples with pores size in the range of 125-300 µm processed with NaCl or Mg space-holders (see 4.2.2) were studied with this device. The samples were cylindrically shaped and prepared for compression tests and, thus, had dimensions of 3 mm diameter and 6 mm height. The main idea of µCT analysis was to obtain 3D data for compression test samples, to evaluate the distribution of pores as well as to find possible cracks in the material. Cracks and a non-homogeneous pore distribution can have a dramatic influence on the results of the compression tests. Sintered porous Ti-40Nb samples were scanned at 130 kV with a voxel size of 2.5 µm and subsequently, coarsened to 10 µm voxel size. Reconstruction was done by Robert Müller with the SkyScan Software in the Institute of Materials Science, TU Dresden.

The μCT measurements were also carried out at the IFW Dresden using the Phoenix Nanotom M device from GE Company. This device was applied for porous Ti-40Nb samples processed with space-holders as well as for loose sintered and hot-pressed samples. The main idea for the analysis was to evaluate the inner architecture, i.e. the interconnection of the pores between each other. An interconnected porous structure (open porosity) is an important demand for materials for hard-tissue replacement. The samples were scanned at 130 kV with a voxel size of 3 μm. The images were then reconstructed with Volume Graphics software.

3.2.6. Compression test experiments

Compression tests were carried out on samples produced both with and without space-holders (see section 4.2) by Arne Helth (IFW Dresden). The compression test samples had a shape of cylinders with a diameter of 3 mm and a height of 6 mm. The samples were polished plane-parallel using a special sample holder. At least 3 samples of the same type were taken for each test. The device used was an Instron 5869, tests were conducted at room temperature. The samples were loaded continuously to failure at a strain rate of 10^{-3} s^{-1}. The stress-strain curves were built from the compression test data by Origin software. The Young´s modulus was calculated from the linear part of the stress-strain curve in the elastic region according to [93]:

$$E = \frac{\sigma}{\varepsilon} = \frac{F/A_0}{\Delta L/L_0} = \frac{F \cdot L_0}{A_0 \cdot \Delta L} \tag{8}$$

Where σ and ε are stress and strain respectively (can be taken from the curve), F is a compression force, A_0 and L_0 are initial cross sectional area of the sample and its initial length, respectively. ΔL is the length change of the sample during compression. F and ΔL are also among the outcoming raw data, calculated by the device during the compression test.

The influence of porosity on the compression failure of the materials can be attributed to the following facts: reduction of the real cross-sectional area of a sample; stress-concentration factor of pores; size effect (the load might be more uniformly distributed in non-porous than in porous materials); prevention of crack propagation by pores; reduction in theoretical strength by the pores [94]. A typical stress-strain curve for a porous material is presented in Figure 23a. The curve is divided into four regions according to a study by Todo et al. In region A the sample demonstrates a linear elastic behavior. In the beginning of region B structure is reorganized and failure of the wall structures of the pores takes place. During stage B the stress stays almost constant. In the beginning of region C the failure process reaches its saturation corresponding to a disappearance of the pores. Region D is the second linear region corresponding to linear elastic behavior of the bulk structure with totally vanished pores [95].

A stress-strain curve of porous samples can be compared to the stress-strain curve for a porous bone (Figure 23 b) presented and discussed by Kefalas [96]. In this study regions C and D are united into one "stage III" and, therefore, the curve was found to consist of three stages. At the first stage a hardening and softening of the material takes place: a growing number of walls between the pores break and collapse, however, a fraction of the total number of the walls is assumed to still resist compression.
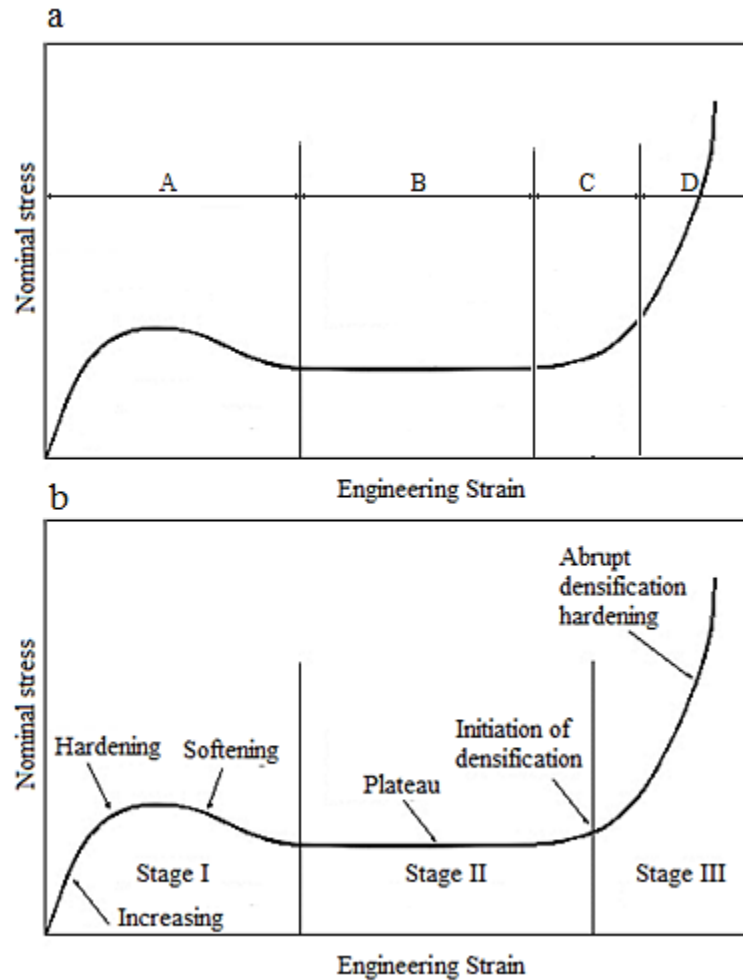
Figure 23: (a) Four different regions in the stress-strain curve of porous materials [95] and (b) three stages in the stress-strain curve of the cancellous bone under uniaxial compression [96].

In the second stage the global structure is assumed to have degenerated into two main phases. One phase consists of a load-bearing stack of failed but bridged struts of the material, encompassing isolated remnants of the original porous structure. These isolated remnants of the original porous structure constitute the second phase. In the final rapidly increasing part of the stress‑strain curve (stage III, Figure 23b), all pores have collapsed, and have degenerated as such. As demonstrated further (see section 4.2) in

the stress-strain curve of porous samples these three phases can be found as well, suggesting that the porous Ti-40Nb samples have the same failure mechanism as described above.

Chapter 4

Results and discussion

The first challenge of the present study was to produce ß-type Ti-40Nb alloys by ball-milling starting from elemental Ti and Nb powders. The second challenge was to obtain porous ß-type Ti-40Nb samples with a Young´s modulus comparable to that of a human bone (≈20 GPa) and a strength of ≈150 MPa.

One of the main problems occurring in the ball-milling process was a small powder yield of ductile Ti alloys. This problem was solved by an addition of a certain amount of a milling agent and the application of suitable milling parameters. Nevertheless, the milled Ti-Nb powder was saturated with oxygen which is a strong α-phase stabilizer in the Ti-Nb system and is not desired to be present in high fractions. Further heat treatment experiments confirmed that a single ß-phase cannot be stabilized at room temperature in the alloy powder with 1.77 wt.-% of oxygen. To reduce the amount of oxygen cleaner starting powders were used and more gentle milling parameters were applied. This resulted in reduction of the oxygen content in the as-milled powders down to 0.37 wt.-% and a single ß-phase could be stabilized by quenching.

Several successful routes for porous Ti-40Nb alloy sample production will be demonstrated in section 4.2. Green compacted and sintered powders resulted in relatively low compression strength of 125-450 MPa and a Young´s modulus of 5-24 GPa. Further experiments with different sintering temperatures proved a strong correlation between the process temperature and the strength of the samples.

Alloy samples with controlled porosity were processed by sintering with space-holders. The strength of these samples varied from 5 to 45 MPa and the Young´s modulus varied in the range of 1.2-3.1 GPa. The porosity was interconnected and its shape depended on the particle shape of the space-holder.

In section 4.3. results of the surface treatment of porous Ti-40Nb alloy samples will be discussed. Samples produced with NaCl as a space-holder were coated with hydroxyapatite $Ca_{10}(OH_2)(PO_4)_6$ by an electrochemical method. The correlation between the deposition time, the solution concentration and the morphology of the hydroxyapatite coating will be obviously demonstrated. Finally it will be concluded that porous samples with a complicated inner architecture can be successfully submitted to hydroxyapatite coating.

4.1. Preparation of ß-type Ti-40Nb via ball-milling

As described before (see section 3.1.1.1), cold welding of the powder particles to the milling media and a resulting small powder yield are one of the main disadvantages of ball-milling of ductile metals. The powder yield is the amount of loose powder that can be recovered from the container (vial) after the ball-milling process. Using traditional organic anti-sticking agents can lead to their decomposition and contamination of milled powder with O, N, C. These contaminations are not desirable. In this section a successful route to produce ß-type Ti-40Nb powder by mechanical alloying via ball-milling without the use of organic milling agents is demonstrated.

4.1.1. Influence of milling parameters and milling agents on the mechanical alloying of Ti and Nb

Milling parameters

Changing the milling parameters and, thus, the intensity of the milling process, can help to reduce the cold welding effect and to enlarge the yield. In first milling experiments only elemental Ti and Nb powders but no milling agents were used and a continuous milling for 40 hours using a speed of 200 rpm was applied (continuous milling mode). The powder yield after a milling experiment was only about 10 wt.-% relative to the total weight of the initial powder mixture. Most of the powder was cold-welded to the vial and the balls. During the ball-milling a complete and homogeneous alloying of Ti (hcp α-phase)

and Nb (bcc ß-phase) into the bcc ß-phase Ti-40Nb alloy was anticipated. But the powder that stack to the walls did not take part in the milling process and was unreacted even after 40 hours. The loose powder that can be found in the vial after 40 hours was in a single ß-type phase state according to the XRD pattern in Figure 24 a. A change of the milling parameters and thus, the intensity of the process were expected to influence the sticking problem. Interval milling with a speed of 250 rpm comprising 15 minutes of milling and 15 minutes of rest was applied (interval milling mode). The milling temperature rises with increasing milling time and speed because of the intensive collisions between the balls and the balls and the vial [97]. The intervals gave time for the vial, the balls and the powder to cool down.

The interval milling regime resulted in a slight increase of the powder yield up to ≈14 wt.-% and still, there was a lot of unreacted powder sticking to the vials and balls. The XRD pattern of loose Ti-40Nb powder after interval milling is presented in Figure 24 b.
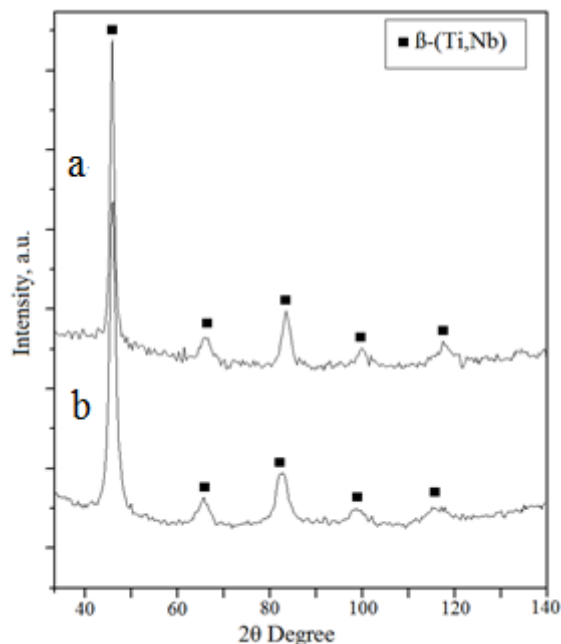

Figure 24: XRD patterns of Ti-40Nb powder ball-milled for 40 hours with different milling modes: (a) continuous mode and (b) interval mode.

Similar as for the XRD pattern taken from the continuously milled powder, there are only peaks corresponding to the ß-type phase detectable, which suggests that the alloying of the elemental powders was complete during the ball-milling. Therefore, for both milling experiments the formation of a bcc ß-(Ti, Nb) phase can be concluded which is attributed to the solid solution of Nb in the Ti lattice.

There has been an attempt to ball-mill crushed pieces of cast pre-alloyed ß-type Ti-40Nb rod material. It is known from the literature [67] that milling of pre-alloyed powders results in a higher yield than milling with starting elemental powders. Besides that milling of pre-alloyed cast material should result in a less contaminated powder. But the experiment does not work; because of the high ductility of the ß-phase alloy the milling was not successful. After 100 hours of milling in a continuous mode the metal pieces were not even refined and there was just a tiny powder yield obtained. So the powder processing was generally carried out following the above mentioned routes.

Changing the milling speed from 200 to 250 rpm did not have a great influence on the powder sticking as well as on the phase transformation. The interval milling appeared to be more gentle than the continuous one: the powder yield was slightly higher and the oxygen contamination of powder milled in the interval mode is considerably lower (see 4.1.2).

Milling with NaCl

NaCl powder was employed as milling agent to reduce the cold welding effect and thus, to enlarge the powder yield and to enable phase reactions. Different fractions of NaCl powder (<65 µm) of 0.25, 0.5, 1, 1.5 and 2 wt.-% (relative to the total weight of the Ti and Nb powder) were added to the vials before milling. The milling regime was similar to that of the first experiment: the milling speed was 200 rpm and the total milling time was 40 hours. The powder yields for the continuous milling mode with

different amounts of NaCl powder are summarized in Table 4. The selected values are the results of at least four experiments.

Table 4: Powder yield (wt.-%) after 40 hours of ball-milling of Ti and Nb elemental powders with addition of varying fractures (wt.-%) of NaCl.

Powder yield of milling experiments with different fractions of NaCl powder					
0 wt.-%	0.25 wt.-%	0.5 wt.-%	1 wt.-%	1.5 wt.-%	2 wt.-%
12±0.5	13.5±2.9	12±3.11	19.5±3.1	15.5±5.5	87±5.6

Additions of 0.25 and 0.5 wt.-% NaCl were not enough to overcome the dominance of cold welding over fracture and, therefore, after 40 hours of milling the yield was still very small. In those cases it can be suggested that the NaCl powder was mostly embedded inside the metal particles during mechanical alloying and that this amount of NaCl is not enough to prevent the cold welding. The use of 1 and 1.5 wt.-% of NaCl shifted the balance between cold welding and fracture towards the latter, but still the yield was not high enough. Thus, 2 wt.-% of NaCl is the minimum amount, which is needed to reliably balance the cold welding and fracture processes during the ball-milling and to significantly enlarge the yield to almost 90%. The sticking problem occurs because of the high ductility of the Ti–Nb alloys. NaCl has an influence on the ''fracture–cold welding balance'' during ball-milling: it reduces cold welding so that the powder fracturing process is promoted. NaCl particles are incorporated in the metal particles surfaces and spread on the surface like a lubricant [98].

An important aspect is the analysis of the progress of the mechanical alloying process and related phase transformation reactions with milling time. XRD patterns of Ti-40Nb powder mixtures milled with 2 wt.-% NaCl are shown in Figure 25 in dependence on the milling time.
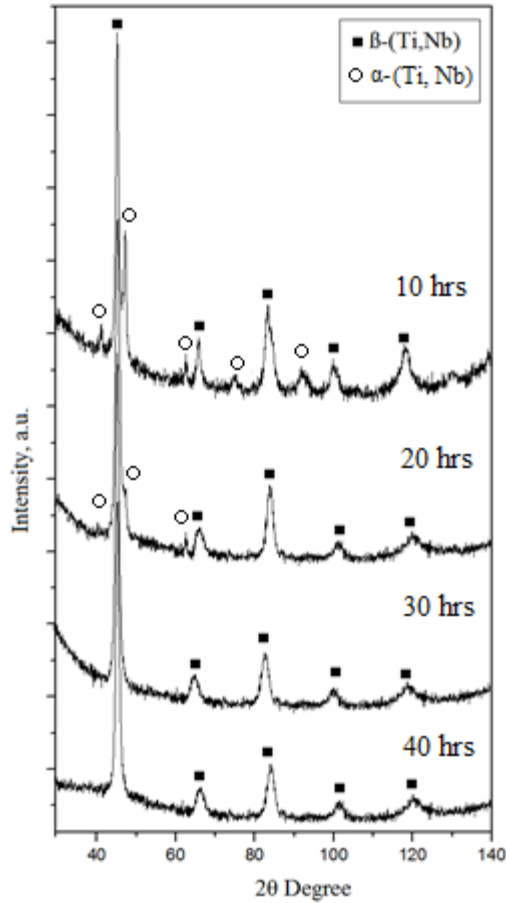
Figure 25: XRD patterns of Ti-40Nb powders: powders milled in continuous mode for 10, 20, 30, and 40 hours with 2 wt.-% NaCl addition.

According to the Ti-Nb non-equilibrium diagram (see Figure 8) the alloys with a low Nb content still consist of single α-phase or a mixture of α- and ß-phases. That is why the α-Ti peaks in the XRD patterns disappear gradually and are detectable even after 30 hours of ball-milling indicating that the starting powders are not yet completely reacted. The reflections of Nb and ß-type Ti-Nb are overlapping in the XRD pattern that is why the mechanically alloying was considered to be complete when the α-phase peaks disappeared. At the same time Nb peaks are moving towards the Ti-40Nb reflections. The broadening of the peaks during milling indicates both a lattice deformation and a decrease of the grain

size. Beyond 30 hours of milling α-Ti peaks are no longer detectable in the XRD pattern, so that it can be suggested that the full hcp to bcc transformation took place (see section 3.1.1 c). The mechanism of α→ß phase transformation of a Ti alloy during ball-milling was described by Pasha et al. [99] as follows: for the transformation to occur a severe plastic deformation resulting in a large lattice expansion is firstly required. Besides that a grain refinement is an important factor in the phase transformation induced by ball-milling: a significant reduction of the grain diameter d_c may lead to a substantial increase in Gibbs energy in ultrafine crystals through the Gibbs-Thompson equation:

$$\Delta G = \frac{4\gamma \cdot V_m}{d_c} \tag{9}$$

where γ is the interfacial energy, V_m - molar volume. In this regard, for example, the continued reduction in d_c below 10 nm eventually causes a bcc to fcc polymorphic change in Ti ball-milled powder [100]. In the present experiments, after 40 hours of milling a single bcc Ti-40Nb phase can be detected in the XRD patterns. The cross-sections of powder particles milled for 10 and 40 hours with 2 wt.-% NaCl were studied with SEM-BSE imaging to follow the alloying process and to verify that the alloy phase is homogeneous in the final particles (Figure 26).
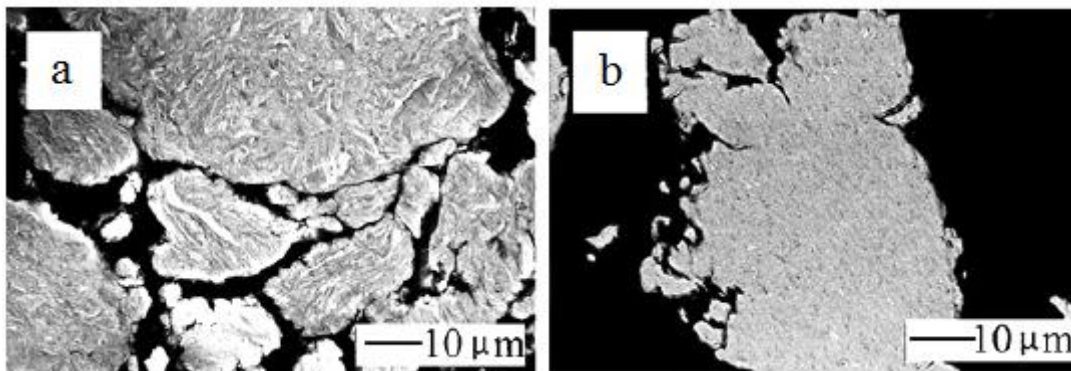

Figure 26: SEM-BSE images of cross sections of ball-milled Ti-40Nb powder particles after (a) 10 hours of milling and (b) 40 hours of milling.

After 10 hours of milling (Figure 26 a) a layered structure is detected. This kind of structure is typical for ball-milled powder and results from the intense repeated welding and fracture processes (see section 2.3.1.2). According to the SEM-EDX studies, the brighter areas in the SEM images represent Ti- and darker Nb-rich areas. The presence of Ti- as well as of Nb- rich areas is in good agreement with XRD data (Figure 25 after 10 hours of milling) where both α-Ti and Nb can be detected. After 40 hours of milling there are no spots of Ti and Nb visible in the BSE image and the cross-sectional area of the mechanically alloyed particles appears to be homogeneous (Figure 26 b). This is supported by the XRD data where after 40 hours of milling only the peaks of the ß-type (Ti, Nb) phase are present (see Figure 25).

α- and ß-type Ti phases can be clearly detected by XRD, but possible minor phases like martensitic α´´- and the ω-phase (see 2.2) have peaks which overlap those of the main α- or ß-phases in the XRD pattern. That is why they cannot be reliably detected by XRD. In principle the ω-phase can be present in as-milled Ti-Nb powder because this phase can be induced by pressure (and thus, by the mechanical load applied during intense ball-milling) [101] as well as by temperature [102]. The most adequate technique to prove the presence or absence of the ω-phase is TEM analysis. In Figure 27 selected TEM results are presented.
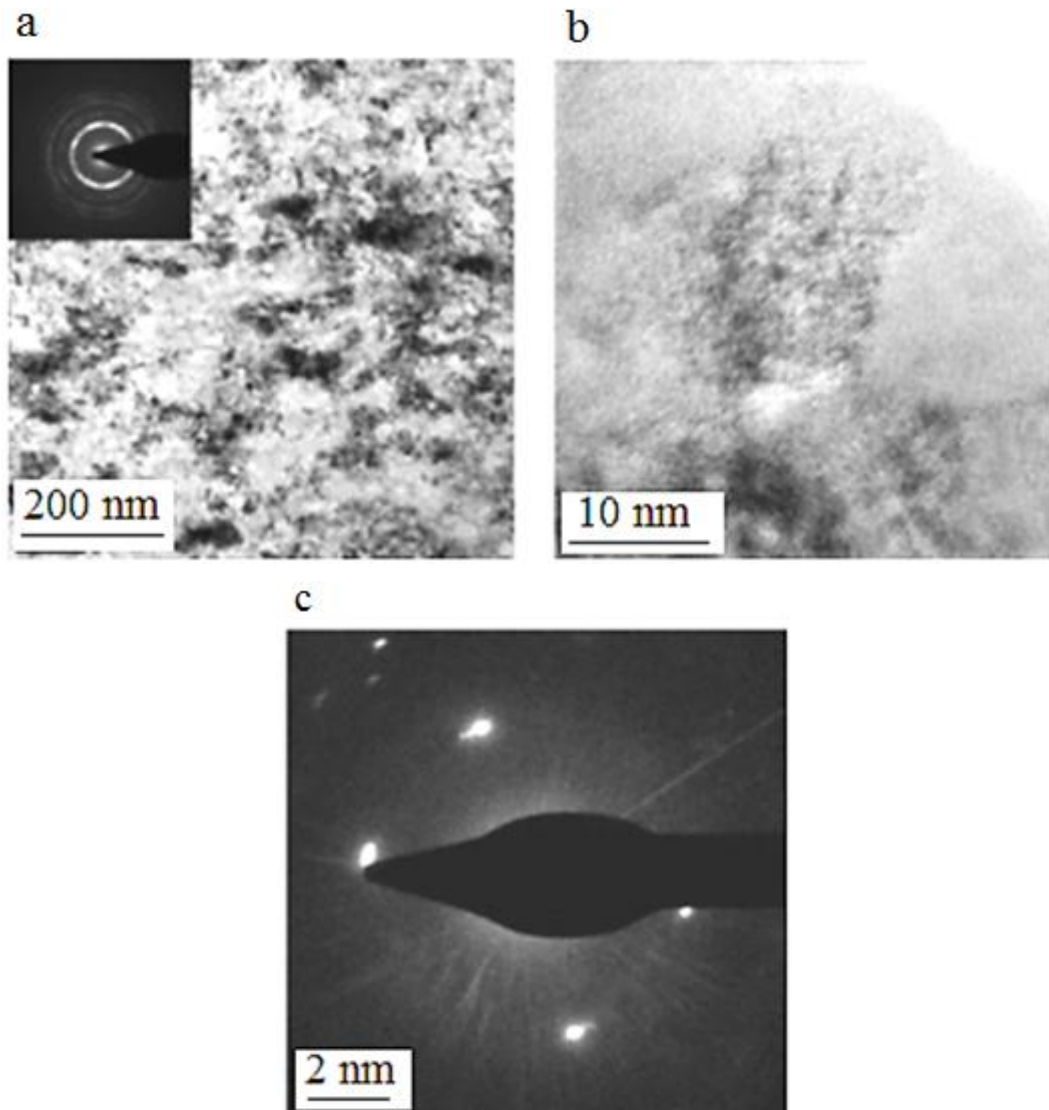
Figure 27: TEM studies of Ti-40Nb alloy powder, ball-milled for 40 hours with 2 wt.-% NaCl: (a) overview bright field image and selected area electron diffraction pattern; (b) high resolution bright field image of a single grain with cubic structure; (c) selected area electron diffraction pattern of a single grain indicating a cubic structure.

The bright-field TEM micrograph in Figure 27a displays the typical strained structure of the milled nanosized powder grains indicating that the lattice is strongly distorted. The electron diffraction pattern taken from this distorted area (inset in Figure 27a) proved that it was nanostructured. Nanograins are

overlap so the diffraction pattern yields a ring shape. High resolution bright-field TEM imaging and electron diffraction was used to analyze the structure of a single grain in more detail (Figure 27b, c). According to the electron diffraction pattern (Figure 27c) the lattice of the grain is cubic. No α- or ω-phase precipitations were found. The grain size of alloyed powder, which was milled for 40 hours with 2 wt.-% NaCl addition was determined from XRD patterns according to the Debye–Scherrer equation (see section 3.2.1) and was confirmed by the TEM images. The mean grain size was found to be 12±5 nm.

The morphology of the powder particles milled with 2 wt.-% NaCl is shown in Figure 28. After 10 hours the particles are mostly agglomerated and their mean particle size is about 30 μm. Upon further milling particle fracture dominates and leads to particle refinement. After 40 hours of milling the powder particles exhibit a uniaxial shape and a mean size of 10 μm was typical. Powder particles, which were milled for 40 hours in a continuous mode without NaCl addition had a less uniaxial shape (Figure 28e) and the powder particles, obtained after interval mode milling were much bigger (Figure 28f).
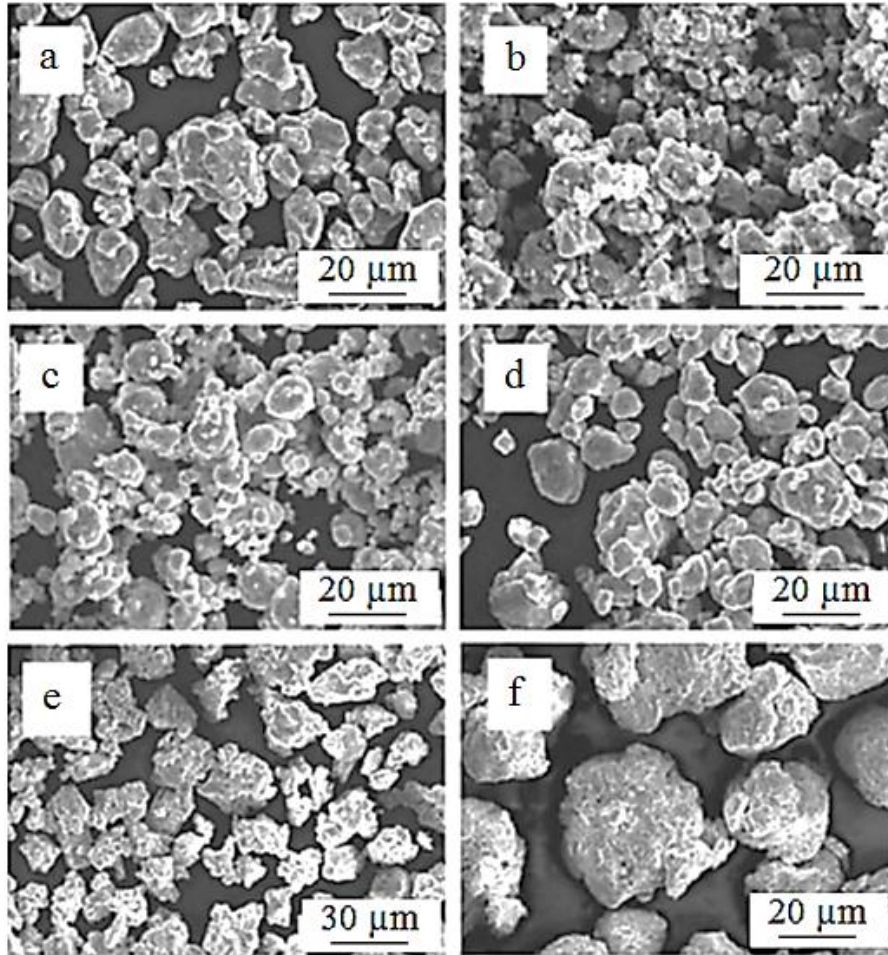
Figure 28: SEM images of Ti-40Nb powder particles after continuous milling with 2 wt.-% NaCl (a) 10 hours; (b) 20 hours; (c) 30 hours; (d) 40 hours; (e) after 40 hours milling in continuous mode with the same parameters but without NaCl; (f) after 40 hours milling in interval mode but without NaCl.

The change in the shape of the metal powder particles milled with NaCl for different times is caused by the influence of NaCl on the surface state of the particles. It has been reported [103] that metal powder particles undergo less deformation with the addition of larger amounts of process control agent (PCA). So it can be suggested that in this study, due to NaCl addition, the powder particles colliding with the milling balls are hardened and fracture into smaller particles. As it can be noticed in Figure 28, the

powder particles milled for 40 hours with 2 wt.-% of NaCl are much smaller than those milled without PCA (Figure 28 e and f). Besides that the shape of the particles milled with 2 wt.-% of NaCl is uniaxial and almost spherical. That is an evidence of a balance between fracture and cold welding during the ball-milling process.

A long milling duration is associated with contaminations of the powders from the milling atmosphere and from the wear of the milling tools. However, in the present case the contamination with Fe from the milling tools or with NaCl from the anti-sticking agent is low, i.e. <1 wt.-%. EDX analyses on cross-sections of powder particles revealed that the final Ti–Nb powder (after 40 hours of milling) contains contaminations of Fe, Na and Cl. The level of contaminations of the Ti-Nb powders milled with 2 wt.-% of NaCl is presented in Table 5.

Table 5: Results of SEM EDX analysis reflecting the contamination of powders with Cl, Na and Fe after different times of milling with an addition of 2 wt.-% NaCl.

Milling time	Amount of contaminations		
	Cl, wt.-%	Na, wt.-%	Fe, wt.-%
10 hours	0.9±0.21	0.41±0.14	0.36±0.04
20 hours	0.93±0.2	0.44±0.14	0.40±0.07
30 hours	0.93±0.15	0.48±0.12	0.42±0.03
40 hours	0.94±0.1	0.42±0.11	0.49±0.02

Upon milling the Ti-Nb powder took up oxygen from the milling atmosphere. The oxygen content was determined by CGHE (see 3.2.4) and was found to be about 0.4 wt.-% in the starting Ti powder and increased up to about 1.77 wt.-% in the completely alloyed powder after 40 hours of ball-milling with an

addition of 2 wt.-% NaCl. The route of the porous sample preparation includes the use of NaCl powder as a space-holder material. After compaction the soluble NaCl particles (the ones used as a milling agent and the ones used as a space-holder) will be removed by water. A small fraction of NaCl particles that may not be dissolved by water exposure is mainly encapsulated inside the alloy particles and thus, it can be predicted that it will not be released in the body fluids as well. Thus, some residual amount of NaCl should not limit the biomedical application of the alloy. With increasing milling time the amount of Fe increases, whereas the amount of Na and Cl remains nearly constant.

4.1.2. Effect of oxygen content and heat treatment conditions on phase evolution

The powders need to be sintered in order to form a porous alloy body. But upon heat treatment of ball-milled powders phase transformations can occur. These transformations depend mostly on temperature, cooling rates and contaminations in the powder. The challenge is to find the suitable milling and sintering parameters to produce porous samples consisting of single ß-phase. In practice the stabilization of the ß-phase turned out to be a big challenge for the ball-milled powders. The behavior of ball-milled Ti-40Nb powder upon heat treatment is different from that of cast alloys or even from that of alloy powder processed by other methods. The main reason for that is a large lattice strain level in ball-milled powder particles and a comparatively higher amount of contaminations like oxygen that can influence the phase transformation.

The amount of oxygen can be critical for phase transformation reactions in Ti alloys because oxygen is a strong α-phase stabilizer (see 2.2.1.) and the ß-transition temperature increases with increasing oxygen content [104]. The effect of oxygen as an α-phase stabilizer is around 7 times stronger than that of aluminum, which is also an α-phase stabilizer [105]. Oxygen can origin from the oxides in the initial starting powders and from the milling tools, from the decomposition of PCA or from the milling

atmosphere. As the particles get smaller they become more reactive. The purity of the milled powder can be influenced by the milling parameters as well as by the choice of the initial powders.

The general strategy that was followed in the present work can be divided into two parts:

1. Milling of different powder types at different milling parameters intended to reduce the O content in the Ti-40Nb powder;

2. Fast quenching from the ß-phase region of ball-milled Ti-40Nb powders intended to stabilize the ß-phase at room temperature.

In the first experiment the ball-milling started with elemental Ti (Figure 29a) and Nb powders (Figure 29 d) mixed to a composition of Ti-40Nb.
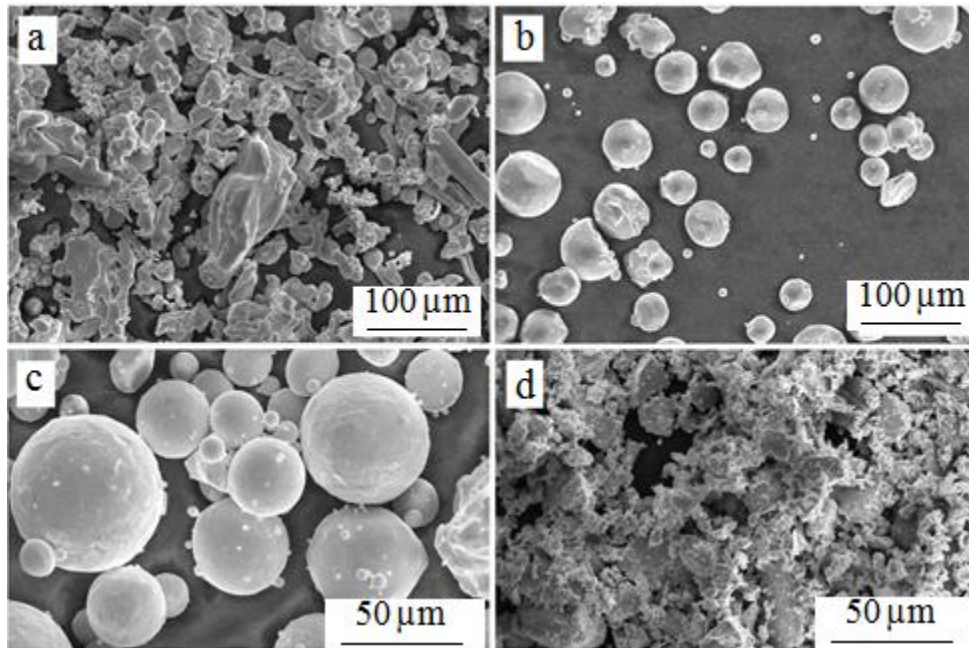
Figure 29: SEM image of initial powders before ball-milling: (a) Ti, (b) gas-atomized Ti, (c) gas-atomized Ti-45Nb, (d) Nb.

The XRD patterns of Ti-Nb powders before and after ball-milling are represented in Figures 30 a and b, respectively. As-milled Ti-40Nb powder consists of single ß-phase according to the XRD patterns and has a high oxygen content of 1.77 wt.-%. The water quenching was carried out from different temperatures of 700, 900, 100 and 1200°C in order to evaluate the influence of the heating temperature on the amount of α-phase in the quenched powder. The XRD patterns representing the results of these experiments are summarized in Figure 31.
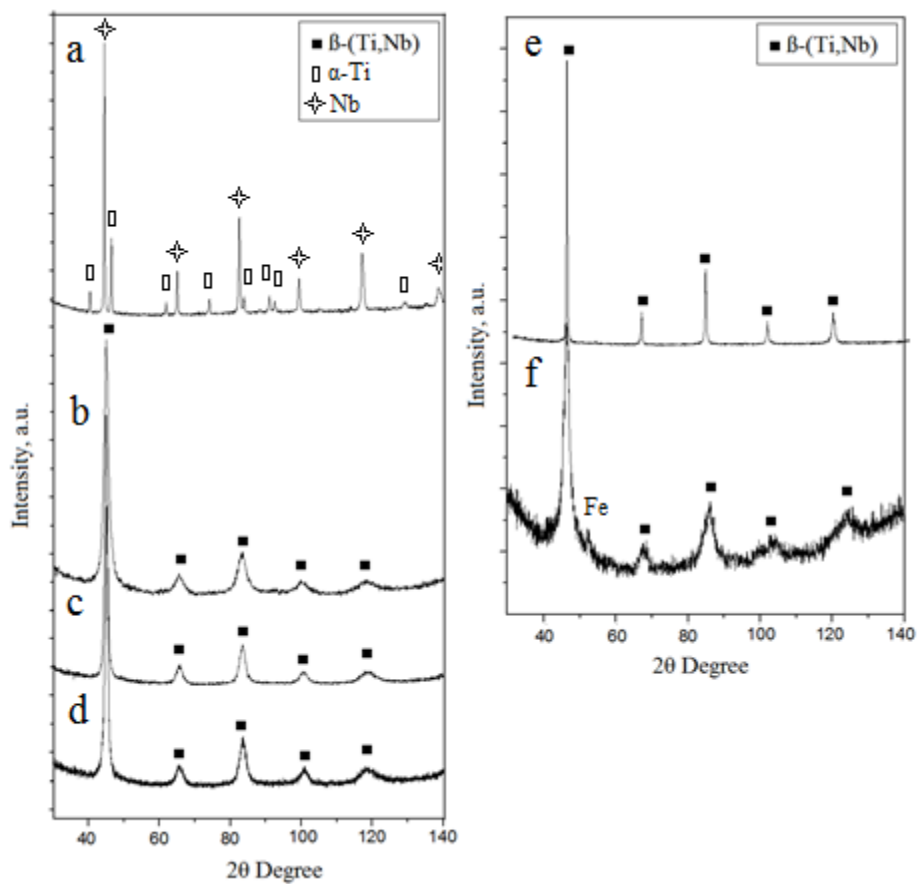
Figure 30: XRD patterns of powders, before and after 40 hours of ball-milling with 2 wt.-% NaCl: (a) initial Ti and Nb mixture, (b) Ti-40Nb; c) Ti-40Nb (at.); (d) Ti-40Nb (250 rpm) after 40 hours of ball-milling, (e) initial Ti-45Nb (atomized) powder and (f) 20 hours of milling Ti-45Nb (atomized) powder.
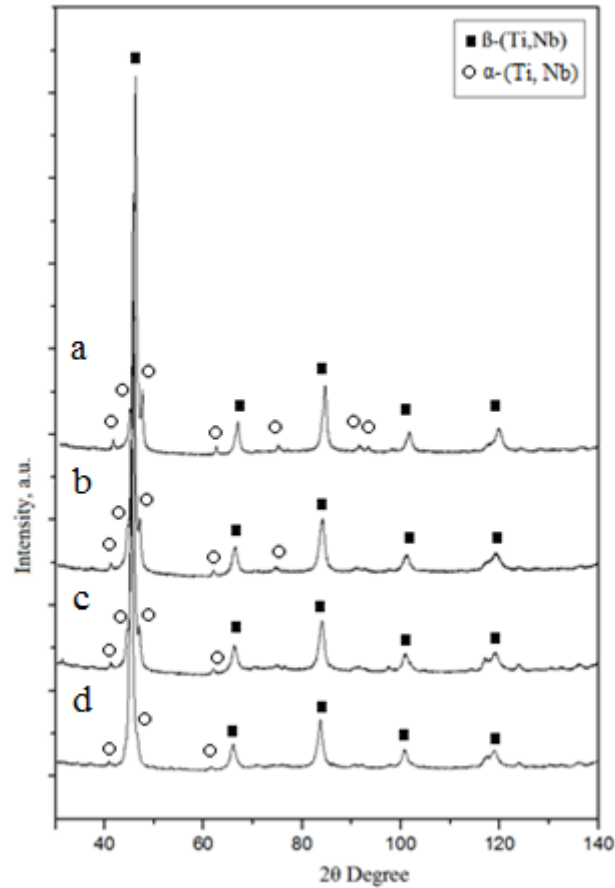
Figure 31: XRD patterns of Ti-40Nb powder with 1.77 wt.-% oxygen after water quenching from (a) 700°C, (b) 900 °C, (c) 1000°C and (d) 1200°C.

The addition of Nb as a ß-stabilizing element reduces the temperature of the α→ß transition to ≈600°C for the composition of Ti-40Nb as seen in the diagram in Figure 7. In pure Ti this temperature $T_{Ti}^{\alpha \to ß}=$ 882°C (see 2.2.2). As mentioned above, ball-milled powder is contaminated with oxygen that acts as an α-phase stabilizer and rises the α→ß transition temperature even higher. The ternary Ti-Nb-O diagram is not available in the literature.

The XRD pattern of Ti-40Nb ball-milled powder with 1.77 wt.-% oxygen quenched from 700°C is presented in Figure 31a. The α-phase peaks are clearly visible in the pattern suggesting and a content of the α-phase determined using by XPErt software is around 17 wt.-%. Rising the temperature to 900, 1000

and 1200°C (Figure 31b, c, d) results in a slight decrease of amount of α-phase. The powder quenched from 1200°C still contains a relatively high amount of α-phase. A further rise of temperature in these experiments was not possible due to the limitation of the temperature by the stability of the quartz tubes. Several attempts were carried out to reduce the oxygen content in the ball-milled powders. In the first approach starting powders with lower oxygen content were chosen. Gas-atomized Ti powder contains only 0.137 wt.-% oxygen compared to 0.4 wt.-% in the previous experiments. This powder was mixed with elemental Nb powder to a composition of Ti-40Nb (will be further addressed as Ti-40Nb (at.) powder). Gas-atomized Ti powder had a typical spherical shape and a mean particle size of 45 μm, as demonstrated in Figure 29b.

The milling was carried out starting from elemental gas-atomized Ti and Nb powders (Figure 29b, d) with a speed of 200 rpm for 40 hours with the addition of 2 wt.-% of NaCl as anti-sticking agent. After the ball-milling Ti-40Nb (at.) powder consisted of a single ß-phase (see XRD pattern in Figure 30 c) and the final yield was around 83 wt.-%. The oxygen level in the milled powder was determined as 0.88 wt.-%. This is only half of the oxygen level of Ti-40Nb alloy powder obtained in the previously described milling experiments.

In the second approach the milling parameters were changed to more gentle conditions. The milling was carried out in an interrupted mode with a speed of 250 rpm and with interruptions every 15 minutes for 15 minutes. 2 wt.-% of NaCl were added as an anti-sticking agent. After 40 hours of ball-milling the powder yield was around 84 wt.-% and the oxygen content 0.371 wt.-%. The milling started with elemental gas-atomized Ti and Nb powders (Figure 30a) and ended with a single ß-phase powder, as demonstrated in Figure 30d.

For comparison Ti-45Nb gas-atomized powder (Figure 29c) was also milled for 40 hours with a speed of 200 rpm and an addition of 2 wt.-% NaCl. The powder was already alloyed and consisted of single ß-phase, as demonstrated in the XRD pattern in Figure 30e. After ball-milling the phase composition remained the same but the peaks became broader, suggesting grain refinement and accumulation of defects in the lattice (Figure 30 f). The peak at ≈50° comes from a contamination of the powder with Fe. The final powder had a very fine particle size of around 5 µm and thus, was very reactive. The initial amount of oxygen in gas-atomized Ti-45Nb powder was 0.215 wt.-% and after 40 hours of milling it raised up to 0.314 wt.-%. The amounts of oxygen in initial and ball-milled states for all the above mentioned powders are summarized in Table 6.

Table 6: Amount of oxygen and phase composition in different powders before ball-milling and after ball-milling with an addition of 2 wt.-% NaCl.

Type of powder	Oxygen content, wt.-%		Phase composition	
	Before milling	After milling	Before milling	After milling
Ti-40Nb	0.4	1.77	Nb+α Ti	ß+12.6±1.6 vol.-% α
Ti-40Nb (at.)	0.137	0.88	Nb+α Ti	ß+4.3±1.1 vol.-% α
Ti-40Nb (250 rpm)	0.137	0.371	Nb+α Ti	ß+1.5±0.2 vol.-% α
Ti-45Nb (atomized)	0.215	0.314	ß	ß

Quenching of these four types of powders from 1000°C revealed a strong correlation between the oxygen content in the powder and the amount of α-phase that appears after quenching (Table 6). Figure 32a shows the XRD pattern of quenched Ti-40Nb powder with an oxygen content of 1.77 wt.-% in the as-milled state. The XRD pattern contains peaks of both α- and ß-phases with an amount of α-phase of 12.6±1.6 vol.-%.
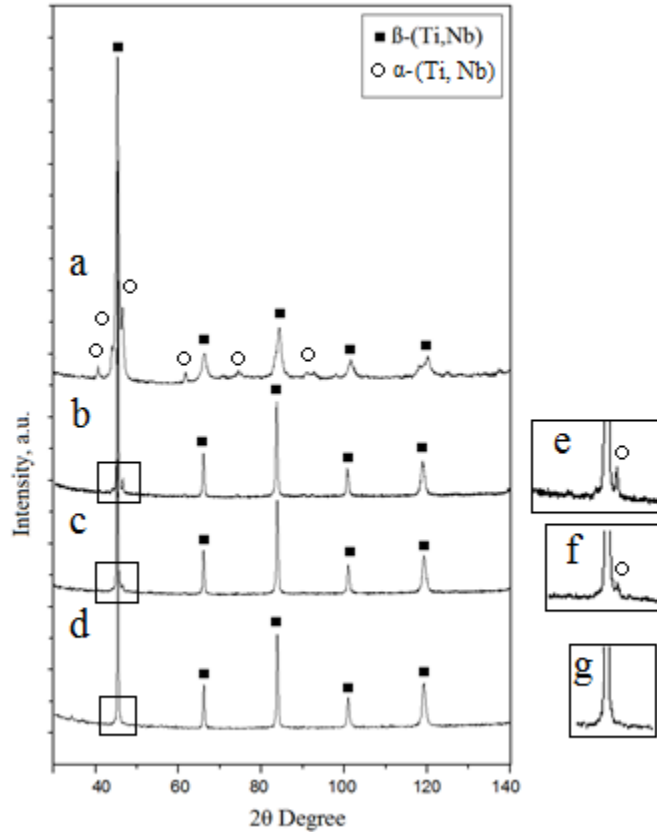
Figure 32: XRD patterns of powders quenched from 1000°C: (a) Ti-40Nb, (b) Ti-40Nb (at.), (c) Ti-40Nb (250 rpm) and (d) Ti-45Nb (atomized) and the enlarged (101) peaks of (e) Ti-40Nb (at.), (f) Ti-40Nb (250 rpm) and (g) Ti-45Nb (atomized).

For Ti-40Nb (at.) powder with 0.88 wt.-% O after milling (Figure 32b, e) the amount of α-phase after quenching was only 4.3±1.1 vol.-%. Ti-40Nb (at.) powder milled with a more gentle regime (250 rpm, pauses every 15 minutes for 15 minutes) had an O content of 0.371 wt.-% and resulted in 1.5±0.2 vol.-% of α-phase after quenching (Figure 32c, f). Ball-milled Ti-45Nb (atomized) powder with the lowest oxygen content of 0.314 wt.-% consisted after quenching only of single ß-phase and no traces of α-phase could be determined from the XRD analysis (Figure 30d, g).

4.1.3. TEM studies of Ti-40Nb powders after heat treatment and quenching

In order to analyze the microstructures and the phase constitution of the Ti-Nb powders in more detail, TEM methods were used. For the TEM study the ball-milled Ti-40Nb powder with highest and lowest oxygen content was chosen, i.e. Ti-40Nb and Ti-40Nb (250 rpm). Prior to TEM studies the powders were quenched from 1000°C to adjust the same phase composition as presented in Figures 30a and d, respectively. TEM images of Ti-40Nb in the as-milled state were already shown in Figure 27 and revealed that the mechanical alloying process is accompanied by a severe grain refinement. This was confirmed by the ring-like selected area diffraction (SAD) pattern presented in the inset of Figure 27a. The mean value of the grain size in as-milled ß-type alloy powder was evaluated both from XRD patterns (Figure 32 b) and TEM images as 12 nm. The grain size after heat treatment at 1000°C for 4 hours and water quenching is around 150-200 nm, i.e. 10 times higher. After heat treatment and quenching of the powders the presence of both β- and α-phases was confirmed by TEM not only in Ti-40Nb (Figure 33) but also in Ti-40Nb (gentle milling with 250 rpm) (Figure 34).
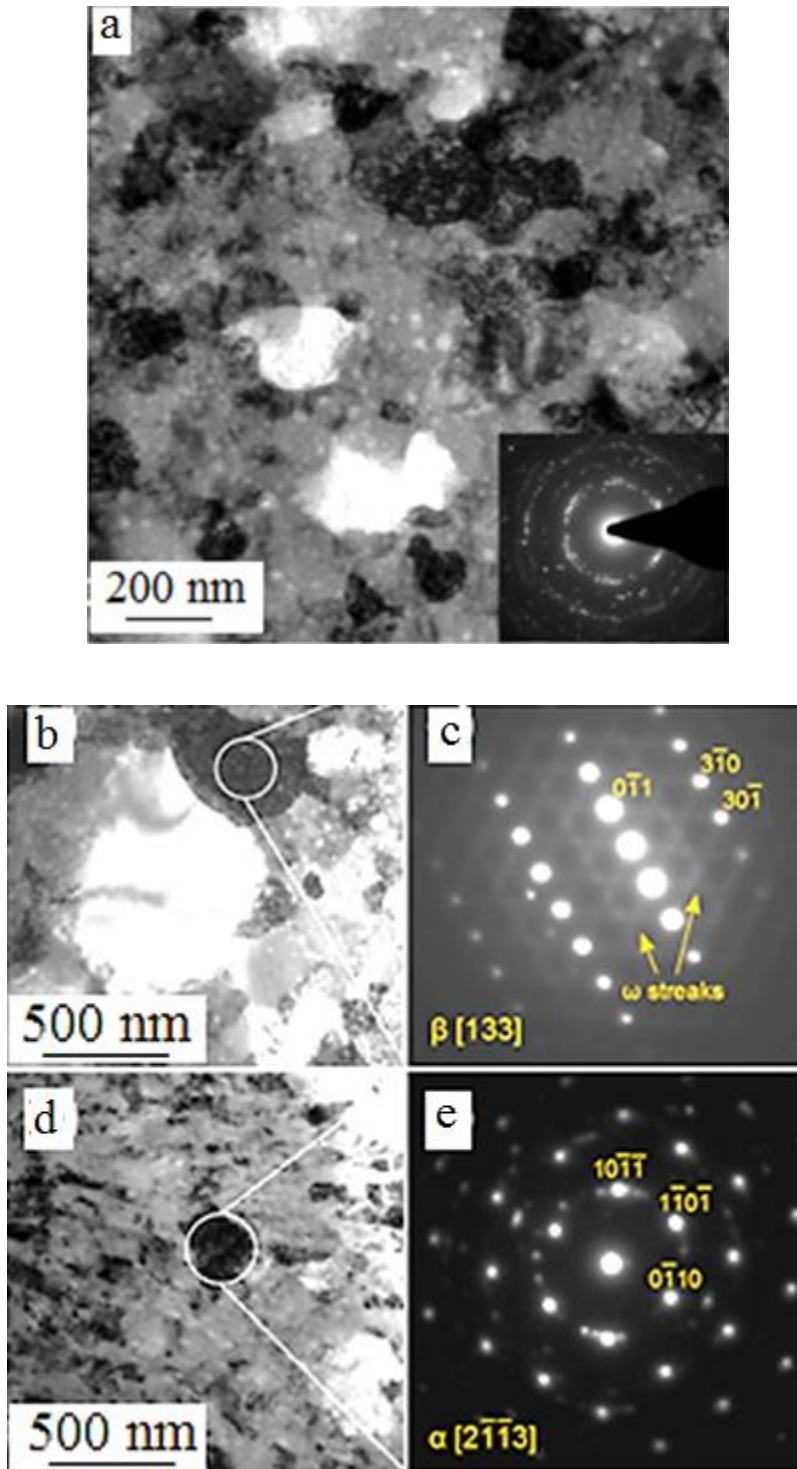
Figure 33: (a) Bright field (BF) and SADP of Ti-40Nb heat treated and quenched, (b) bright field image of a β-phase grain with its (c) SADP showing diffuse ω-phase streaking, (d) bright field image of α-phase grain with its (e) SADP.

The TEM image in Figure 33a represents a bright field image of a Ti-40Nb particle sample taken from the powder with an oxygen content of 1.77 wt.-%. The SADP from the chosen area demonstrated a ring-like pattern because of the small grain size (around 150-200 nm) and the overlapping between them. The reflection from single grains revealed that the structure consists of both α- and ß-phases that is in agreement with the XRD pattern in Figure 32a. The microstructure is mostly represented by a ß-phase matrix (Figure 33b, c) with some α-phase grains (Figure 33d, e). In the diffraction pattern in Figure 33c the reflections of ω-phase are clearly detectable. It is not clear whether the ω-phase which was observed in the heat treated and quenched samples formed athermally in a displacive manner during quenching or thermally activated via diffusional processes. The dimensions of the ω-phase precipitations are of several nanometers. As ω-phase precipitates may form during slow quenching from the ß-phase region or during isothermal aging (see section 2.2.2) it can be concluded that the cooling was not fast enough to suppress the formation of the ω-phase.

This observation supports the XRD results for Ti-40Nb (gentle milling with 250 rpm) that demonstrated only a small α-peak (Figure 32 c). Interestingly, in both samples single grains fully composed of α-phase were found instead of precipitates dispersed in a β-phase matrix (Figure 33 and 34). Additionally, in a Ti-40Nb (250 rpm) sample the selected area diffraction (SAD) patterns of β-phase grains exhibited strong diffuse streaking between the reflexes of the β-phase reciprocal lattice (Figure 34 b), which is a fingerprint of the ω-phase [101]. The heat treatment and quenching procedure not only caused the α- and ω-phases to form, but also led to an increase in grain size which can be attributed to grain growth during the heat treatment from 12 nm in as-milled powder to 150-200 nm in quenched powder. The reduction of the O content from 1.77 wt.-% to 0.371 wt.-% stabilized the β-phase (as seen by the vanishing of the α-phase XRD peak intensities), though it did not significantly influence the formation of the ω-phase during the heat treatment and water quenching procedure.
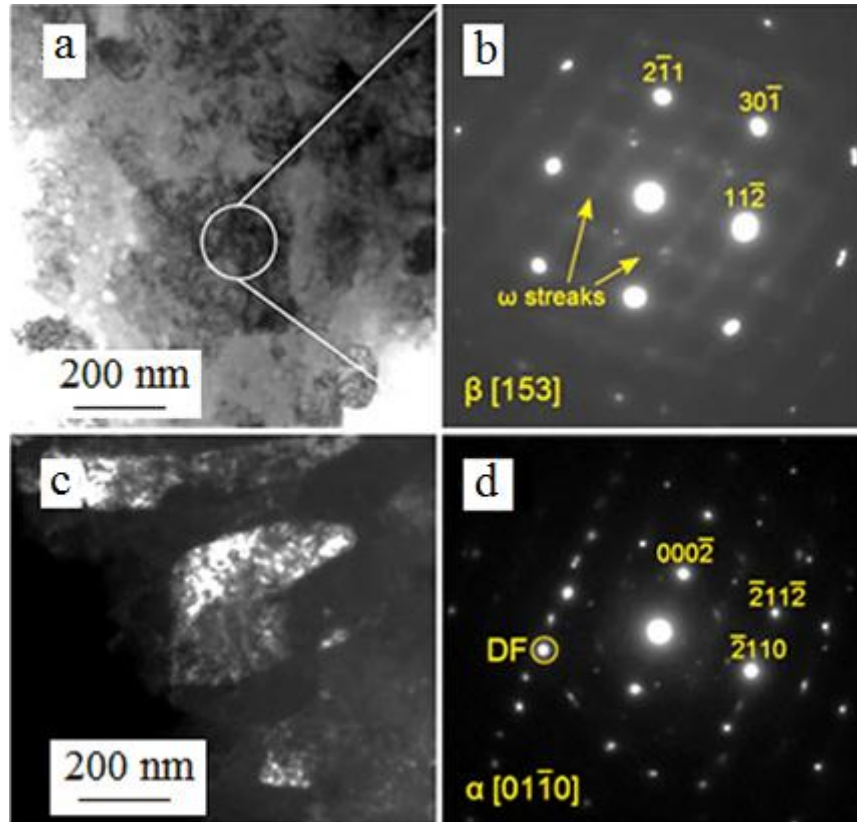
Figure 34: TEM of Ti-40Nb (250 rpm) heat-treated and quenched: (a) bright field image of a β-phase grain and (b) its SADP exhibiting diffuse ω-phase streaking, (c) dark field image of an α-phase grain with its (d) corresponding SADP.

Since Fe is known as β-stabilizer (see 2.2.1.), it can be speculated that Fe-containing wear debris from the milling tools influenced the resulting phase constitution of the heat treated and quenched powders. However because the milling time was kept constant, the amount of wear debris should be identical in all powders. Thus the observed changes in phase constitution of the Ti-40Nb powders can be attributed solely to the influence of oxygen.

4.2. Porous samples preparation and characterization

4.2.1. Loose powder sintering

The ball-milled Ti-40Nb powder with 1.77 wt.-% O was used for all the sample production in section 4.2. To evaluate the influence of micro-porosity of the samples on Young´s modulus and the ultimate compression strength, samples with different porosity were prepared by loose powder sintering. Different porosities were obtained by applying different pressures at the green sintering step (for the processing route see Figure 21). Ti-40Nb powder was pressed at room temperature with 300, 420, 540 and 700 MPa and then sintered for 4 hours at 1000°C. The samples, which were sealed for sintering in quartz tubes, quenched from 1000°C into water. The XRD patterns of as-milled powder and quenched samples are presented in Figure 35. While the as-milled alloy powder was of pure ß-phase the sintering and quenching resulted in a mixture of α- and ß-phases at room temperature. No traces of any other phase of the Ti-Nb system or of any contamination can be detected in the XRD patterns.
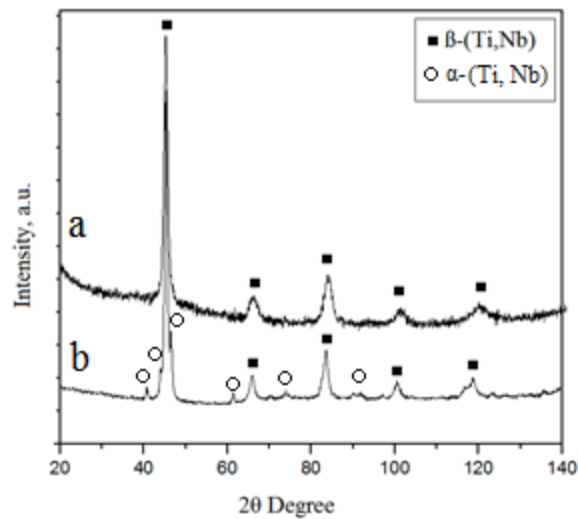

Figure 35: XRD patterns of (a) ball-milled Ti-40Nb powder and (b) sintered and quenched Ti-40Nb sample, produced via cold pressing at 700 MPa.

All in section 4.2.1 prepared samples were submitted to the same thermal treatment and, therefore, had the same phase composition as presented by the XRD pattern in Figure 32b. After quenching, the total porosities of the samples were in the range of 24-36 % according to Archimedes measurements. As reference, a 100% density sample was a cast Ti-40Nb sample with a density of 5.5 g/cm^3 which corresponds to the theoretical density. The pores had an irregular shape and a mean size of around 3 μm as can be seen in Figure 36a. There is only a so-called "micro-porosity" (see section 2.3.2.2) present in the samples produced by loose powder sintering. The powder particles are clearly detectable in all the samples. The particles are interconnected by small necks, which is a typical case for a loose powder sintering process (see section 2.3.2.1). In the SEM images the influence of different pressures and, thus, differences in the sample porosity is not clearly visible.
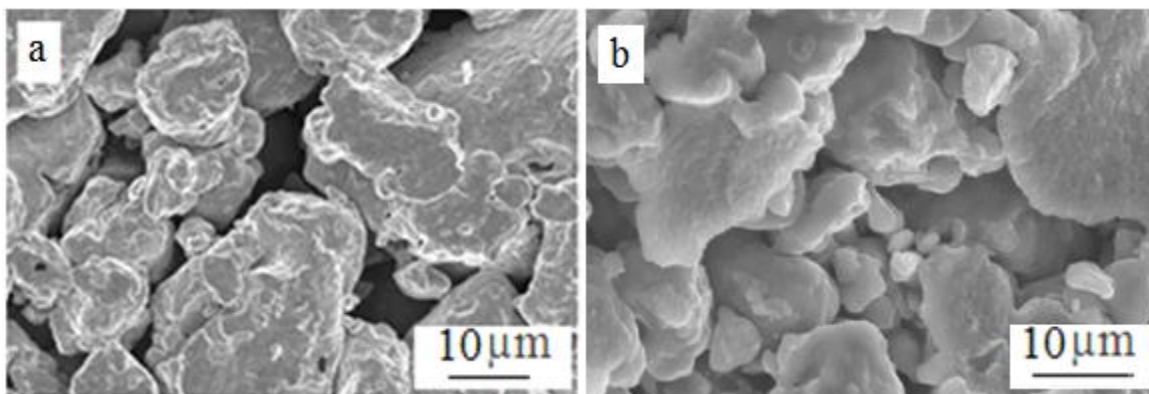

Figure 36: SEM image of micro-pores in samples (a) cold pressed at 700 MPa and sintered at 1200°C and (b) hot-pressed at 700°C and 700 MPa.

The compression tests yielded typical stress-strain curves for porous samples (see section 3.2.6). One of them is presented in Figure 37a. Up to a stress of ≈ 200 MPa the curve suggests an elastic behavior of the material that follows Hook´s law. At the first stage of compression the individual bondings between the powder particles break. The maximum stress that was achieved in this stage was ≈270 MPa for a sample

with ≈26% porosity. At the second stage more connections between particles collapse decreasing the porosity of the sample. There is a short plateau region in the stress-strain curve that corresponds to this process (at strain values of 3-4%). At the last stage a breakage of the whole sample takes place. The maximum strain reached by the sample was ≈ 6%. The maximum elongation of the sample before fracture was ≈1.5% which is a hallmark of brittle failure of a sample. As has been discussed before, the stress-strain curve for a micro-porous Ti-40Nb alloy sample produced by loose powder sintering has similar stages as that for human bone (see section 3.2.6).

Compression tests have demonstrated that Young´s modulus and the ultimate strength decrease with increasing porosity. This behavior was expected according to Oh et al. [8]. The Young´s modulus of microporous Ti-40Nb samples with different densities corresponding to porosities of 22-31% varied from 6.2 to 18.8 GPa, which is in the range of Young´s modulus values of a reference human bone. The ultimate strength of these samples was 141-360 MPa which is little higher than that of a human bone (150 MPa) [14]. The compression test data obtained from numerous stress-strain curves for a variety of micro-porous Ti-40Nb samples are summarized in Figure 38a which shows data for Young´s modulus and the ultimate compression strength.
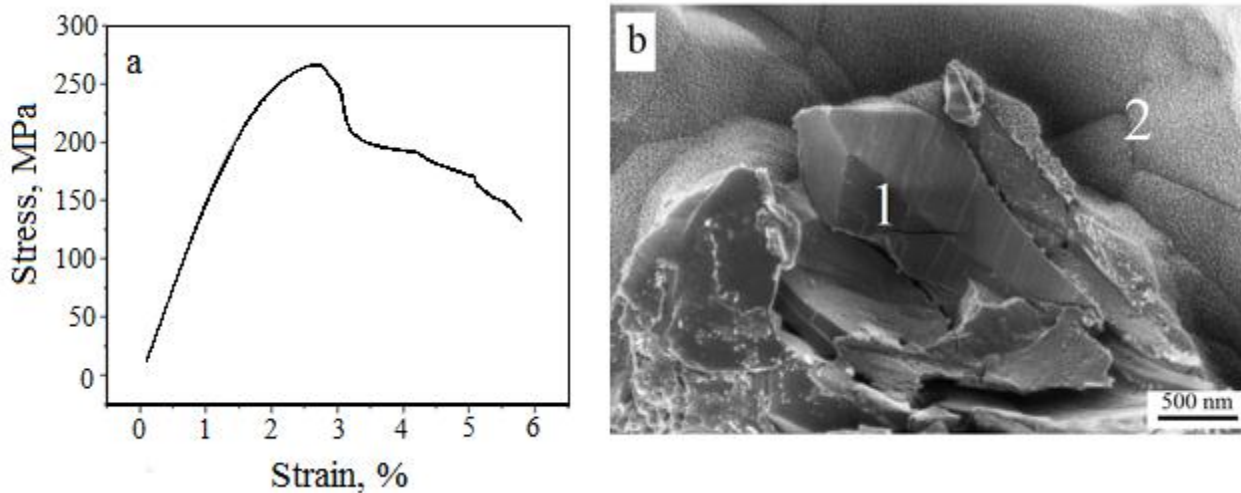
Figure 37: (a) Typical stress-strain curve for Ti-40Nb samples, processed by loose powder sintering at a pressure of 700 MPa with further sintering at 1000°C for 4 hours and (b) Fracture surface of this sample.

The SEM image of a sample after fracture is presented in Figure 37b. A fractured area is marked as 1 and sintered powder particle, which was not damaged by compression, is marked as 2. The fractured zone is a neck, which connected the two powder particles after sintering (according to section 2.3.2.1). The image demonstrates a typical brittle character of a fracture surface. This is in agreement with the compression curve, where the maximum strain is only ~6% which suggests brittle fracture of samples.

The data from the compression tests of samples which were cold-pressed at different pressures and sintered at 1000°C are presented in Figure 38. Young´s modulus is reduced with increasing porosity of the samples as expected according to Oh et al. data [8]. The highest Young´s modulus of ≈20GPa was detected for samples with porosity of ≈25% and the lowest Young´s modulus of ≈8GPa – for ≈35% porosity. The comparison of data obtained in these experiments with Ti-40Nb (ball-milled) to the ones published by Oh et al. [8] for cp-Ti (gas-atomized) reveals that the mechanical properties differ. For the

Ti-40Nb samples porosities of ≈30% correspond to Young´s modulus values of 6-9 GPa compared to result by Oh et al. where a porosity of ≈30% in Ti yielded a Young´s modulus of ≈25 GPa. The reason for that difference can be the phase composition of the alloy. In the experiments described above the alloy consists of mostly ß-phase which has a relatively low Young´s modulus of 62 GPa (see section 2.2 and Figure 9). In the work by Oh et al. the alloy consists of single α-phase Ti with a high Young´s modulus of ≈110 GPa.
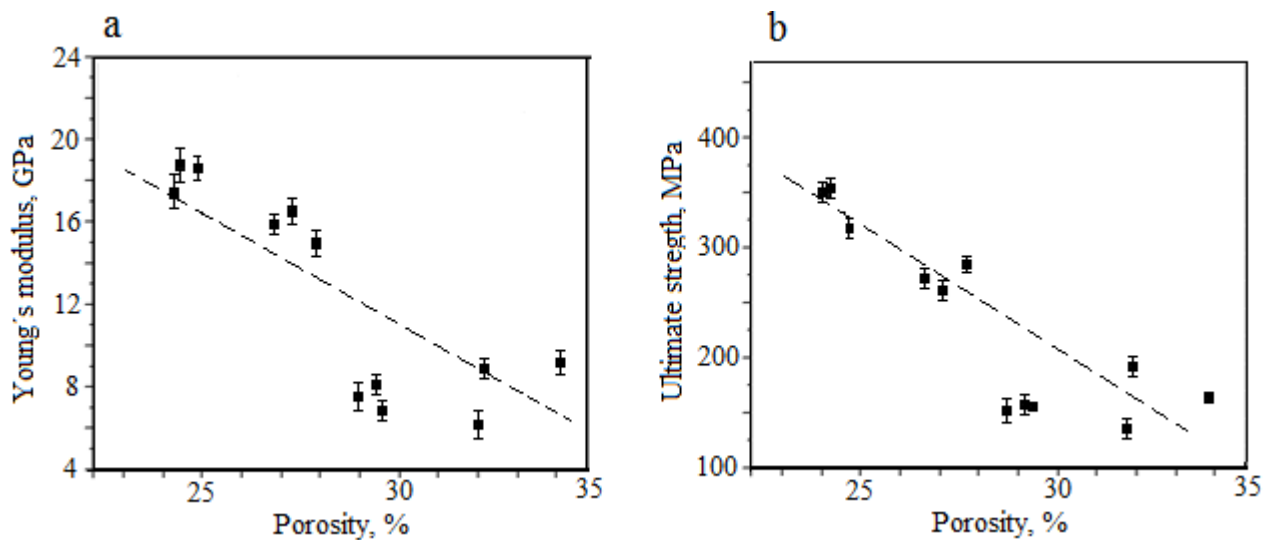

Figure 38: (a) Young´s modulus and (b) compression strength of samples processed by loose powder sintering at a pressure of 300-700 MPa with further sintering at 1000°C for 4 hours.

The ultimate strength of the samples shown in Figure 38b is reduced from 350 to 150 MPa with increasing porosity. The desired mechanical properties of the porous Ti-40Nb samples result from the expected biomedical applications of this alloy. As described before (see Introduction) the Young´s modulus of the human cortical bone is 15-30 GPa and its strength is 70-150 MPa. To avoid the stress shielding (see section 2.1.1) the Young´s modulus of the alloy should be close to the Young´s modulus of the bone. Therefore, the samples with porosities of 24-28% and corresponding Young´s modulus values

of 14-20 GPa are most suitable to fulfill the mentioned requirements. These samples have a relatively high strength of 250-350 MPa. In the work by Oh et al. for Ti powder, a Young´s modulus of ≈20GPa was achieved at higher porosity of 30-35% and the corresponding strength was ≈100 MPa.

In general the phase composition is an important aspect for implant materials. Ti alloys with low Young´s modulus are expected to have a single ß-phase composition and the presence of other phases is not desired. The reason for that is the relatively low Young´s modulus of the ß-phase and its good ductility (see section 2.2.1). In the above mentioned cold pressed and sintered samples the phase composition was determined from the XRD pattern (Figure 35b) as a mixture of α- and ß-phases. But in the case of samples with a relatively high porosity the reduction of Young´s modulus results mostly from the porous structure and, in smaller extent, from the phase composition. That is why it was possible to reduce Young´s modulus to ≈8 GPa in spite of the presence of α-phase in the alloy.

To summarize the results of these experiments, the samples processed from ball-milled Ti-40Nb powder by green compaction at 540 and 700 MPa, sintered at 1000°C and water quenched have the best combination of Young´s modulus and strength and are suitable for biomedical applications.

For comparison a series of samples was produced by hot-pressing at a temperature of 650°C and a pressure of 700 MPa for 30 minutes pressing time. The samples were cooled down within the hot-press chamber. The porosity of these samples was found to be only 5±0.9 %, i.e. a nearly fully dense state was achieved, and it was very fine and not interconnected (see Figure 36b). The compression strength of hot-pressed samples was 1554±50 MPa and Young´s modulus was 80±3 GPa. The typical stress-strain curve of a hot-pressed sample is shown in Figure 39a. The strength of the hot-pressed sample is considerably higher than that of a loosely sintered sample (1400 MPa and 260 MPa, respectively) and the maximum strain of both samples was found to be roughly the same, around 6%. The high strength of the hot-

pressed sample and its high Young´s modulus can be explained by the low porosity of the samples and the relatively high oxygen content in the compacted powder.
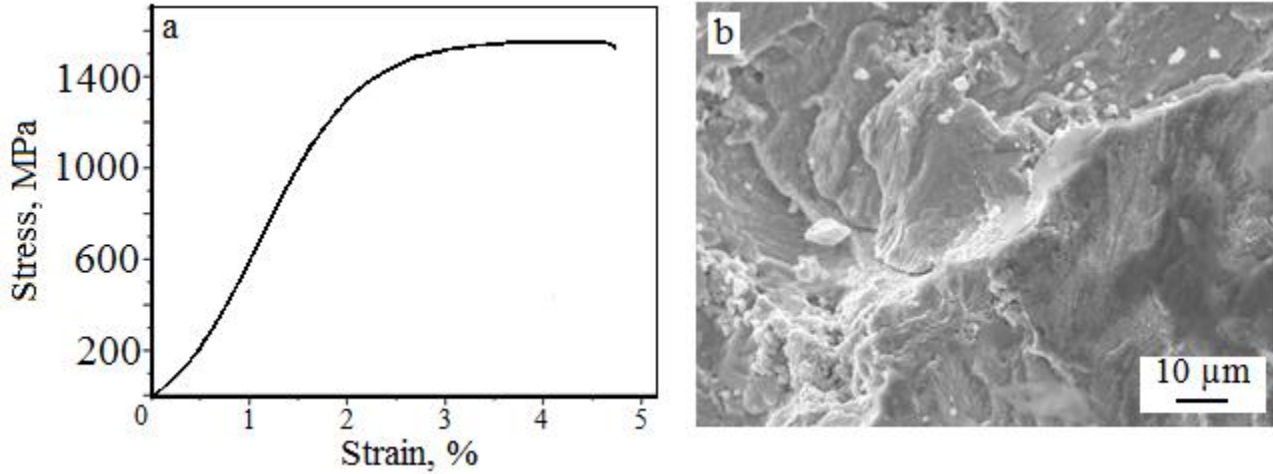

Figure 39: (a) Typical stress-strain curve for Ti-40Nb samples, processed by hot-pressing at 700 MPa and 650 °C and (b) Fracture surface of this sample.

The brittle fracture character was supported by the image of the fracture surface (Figure 39b). The main disadvantage of hot-pressing was the cooling rate of the samples. It was impossible to perform quenching or fast cooling of hot-pressed samples for technical reasons, so the samples were only cooled down inside the chamber. This slow cooling resulted in a high amount of α-phase in the final samples. It can also lead to the formation of ω-phase according to results of Sun et al. [34]. Special hot-press devices with a possibility of fast cooling of the samples should be used for further research in this field. That is why all the below mentioned macro-porous samples were produced by the previously described green compaction at room temperature and the sintering route.

4.2.2. Sintering with space-holder materials

For the sample preparation ß-type Ti-40Nb powder was mixed with NaCl or Mg powder particle fractions to form the desired porosity. Then the samples were green compacted at room temperature with a pressure of 700 MPa, sintered at 1000°C for 4 hours and water quenched. For the removal of NaCl the samples were immersed in 80°C water for 4 hours (Figure 40a) and Mg space-holders evaporated nearly completely during sintering (Figure 40c). Still the samples with NaCl space-holders are easier to produce than those with Mg (Mg evaporation during sintering).

As described in the theoretical part, samples sintered with space-holders have two types of porosities: macro- and micro-porosity (see 2.3.3.3 c). The macro-porosity is formed by the space-holder particles and the micro-porosity – due to incomplete sintering. The size and dimensions of the macro-pores depend on the size and dimensions of the space-holder particles. The average pore size is ~208.0 μm for the macro-pores formed by NaCl particles and ~410 μm for macro-pores formed by Mg particles. In both cases this fits to the range of 200 to 500 μm pore size recommended for biomedical applications. The morphology of a sample prepared by loose powder sintering with additions of NaCl as a space-holder is demonstrated in Figure 40b. Since NaCl particles are not deformed by cold pressing for green body preparation, the macro-pores replicate exactly the shape of the initial space-holder particles (Figure 40a), which is rectangular corresponding to the shape of the NaCl particles. The macro-pores resulting from evaporation of Mg particles which were added as powder fractions of 50% to the starting powder mixture have a slightly ellipsoidal shape (Figure 40e). This is because of the deformation of the initially spherical ductile Mg particles during green compaction. The size and shape of the micro-pores depend on the sample preparation method (for example, loose sintering or hot-pressing) as well as on the process parameters such as compaction pressure, sintering temperature and so on. In the present work the mechanical properties of samples prepared by loose sintering with space-holder were varied by the

amount of the space holder and thus, the amount of the macro-porosity of the sample. The micro-pores of samples prepared with NaCl and Mg space-holders have the same irregular shape and dimensions of ≈3μm as demonstrated in Figure 40 c and f, respectively.
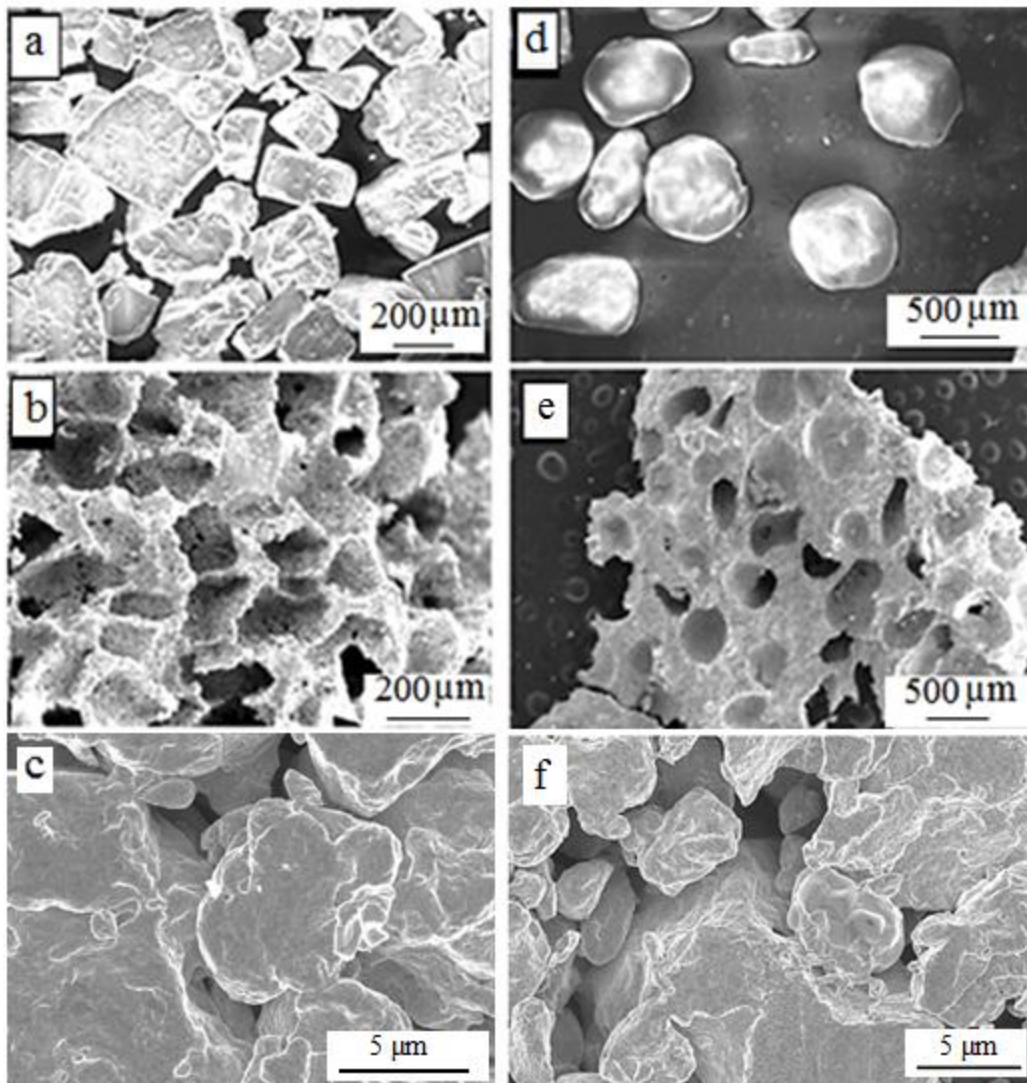

Figure 40: SEM images of (a) NaCl space-holder particles, (b) pores formed by NaCl particles, (c) pores formed between Ti-40Nb powder particles; d) Mg space-holder particles, (e) pores formed by Mg particles, (f) pores formed between Ti-40Nb powder particles.

A series of porous samples produced with NaCl space-holders was prepared for compression tests and structural characterization. The final porosity of the sintered and washed compacts was a sum of macro-pores (produced by space-holders) and micro-pores (formed between Ti-40Nb metal powder particles) and was evaluated as 58, 62 and 65%. As the amount of space-holders (macro-porosity) was known, the micro-porosity was calculated to be about 27.5% which is in good agreement with the porosity of loose sintered samples at the same conditions.

Samples with a porosity of 58, 62 and 65% were submitted to µCT analysis prior to compression tests. The purpose of the study was to characterize the inner porosity of the samples with a non-destructive method. Characteristic µCT images for the samples with different porosities are presented in Figure 41. The cross sectional and 3D images of these samples suggest that the porosity is interconnected and is homogeneously distributed all over the samples, the pores have an almost cubic shape like the NaCl space-holder particles. There were no defects (for example, cracks) found in the inner structure of the samples.
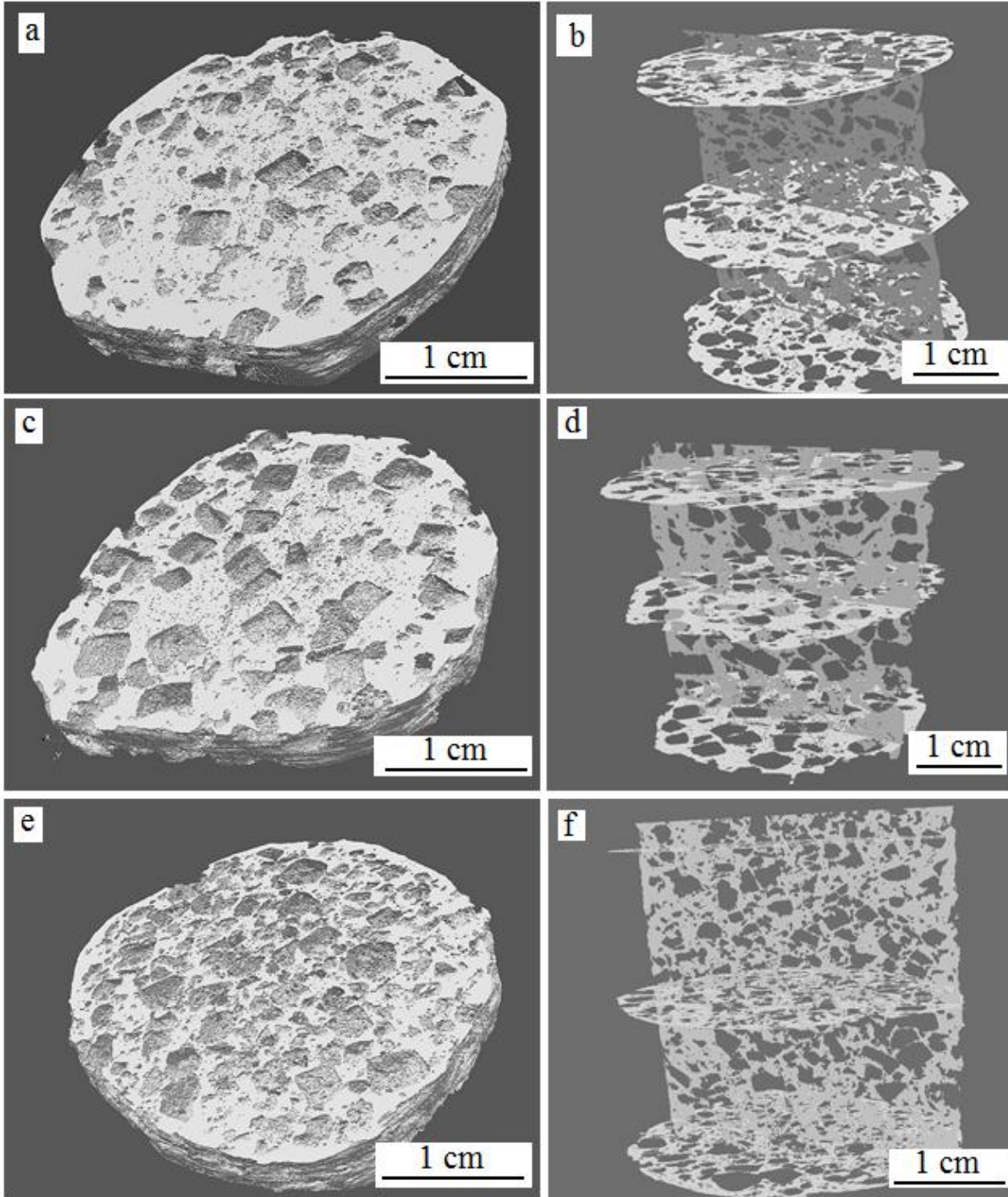
Figure 41: 3D and cross-sectional µCT images of sintered Ti-40Nb samples produced with NaCl as space-holder with porosities of (a), (b) 58 %, (c), (d) 62 % and (e), (f) 65 %.

Compression tests were carried out for porous Ti-40Nb samples, which were produced with NaCl as space-holder material in order to determine compression strength and Young´s modulus. Figure 42a shows a stress-strain curve of a Ti-40Nb sample produced with NaCl as a space-holder. The porosity of the sample was around 58%, but the curve was typical for all the tested samples. It consists of three stages like the theoretically described curve for porous materials (see 3.2.6) and like the stress-strain curve for loosely sintered porous Ti-40Nb samples (Figure 37a). The strength of the samples produced by loose sintering with space-holder is considerably lower than that of the loose sintered sample (10-45 MPa and 260 MPa, respectively). The Young´s modulus of samples produced by loose sintering with space-holder is also very low, only 1.2-3 GPa compared to 5-20 GPa for samples produced by loose powder sintering (Figure 37). The low values of strength and Young´s modulus for the samples with higher porosity are in good agreement with data obtained by Oh et al [8] (see Figure 10).
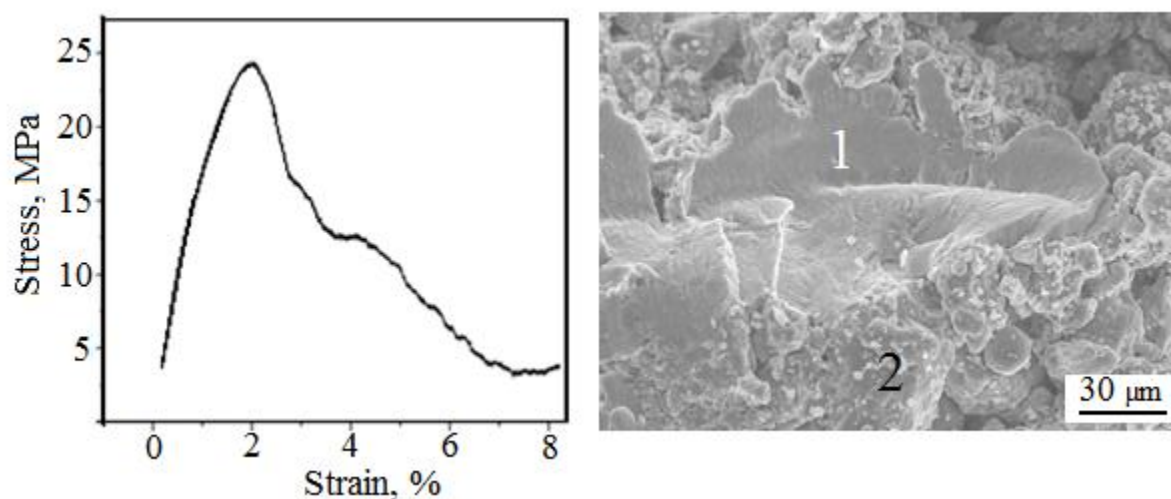

Figure 42: (a) Typical stress-strain curve for porous Ti-40Nb samples, processed by sintering with NaCl space-holder and (b) fracture surface of the sample.

A typical SEM image of a sample fracture surface after compression test is presented in Figure 42b. The fractured area is marked as "1" and the sintered powder, which was not damaged while compression is

marked as "2". The fractured surface demonstrates a typical brittle character. This is in good agreement with Figure 37b, where the fracture of the loosely sintered Ti-40Nb sample is shown. As the temperature regime and the process parameters were the same for loose sintered samples and for those sintered with NaCl space-holders the samples are expected to have a similar brittle behavior.

Figure 43 shows the effect of porosity in the range of 58-65% on Young´s modulus and the ultimate compression strength. It is clearly visible, that Young´s modulus as well as the strength decrease with increasing porosity. The lowest Young´s modulus of ≈1.2 GPa was achieved at a porosity of 64% and the ultimate strength of this sample was found to be ≈10 MPa. The compression strength of samples decreased from 44.9 to 8.24 MPa with increasing porosity.
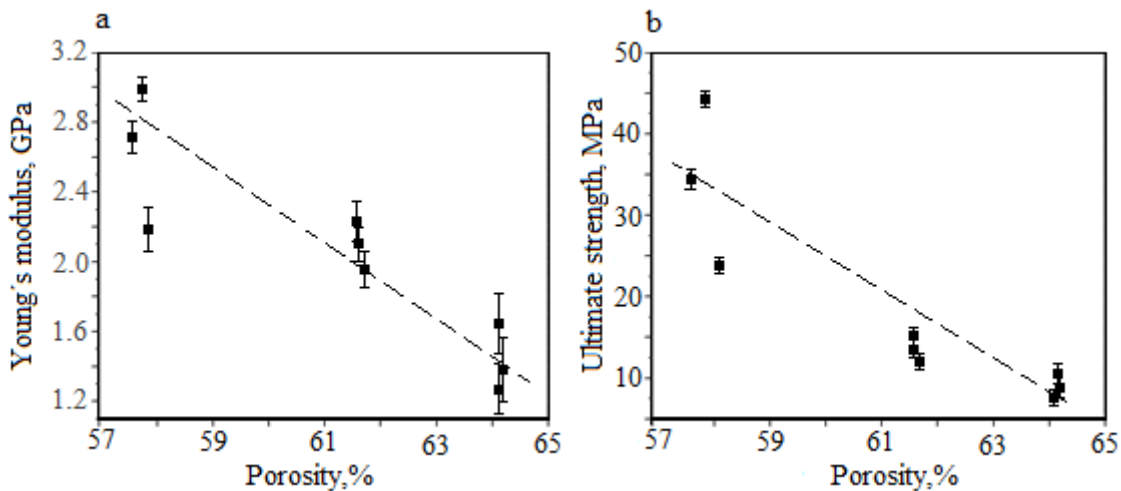

Figure 43: Experimental data for (a) Young´s modulus and (b) ultimate compression strength versus porosity for samples produced with NaCl space-holder.

These values of ultimate compression strength and Young´s modulus are considerably lower than those for the loosely sintered powder given in Figure 38 and are in good agreement with mechanical properties of human spongy bone,which has a Young´s modulus of 0.2-2 GPa and a compression strength of 5-50 MPa [5]. It can be suggested that the porous Ti-40Nb alloy produced with NaCl as a space-holder is a

promising material for biomedical applications. The samples with porosity of 60-63% demonstrate a Young´s modulus in the range of 1-2 GPa and an ultimate compression strength of 10-20 MPa that is very close to the mechanical properties of a human spongy bone.

Summarizing the results for the mechanical properties of ß-type Ti-40Nb samples processed by different methods it can be concluded that these alloys are promising materials for load-bearing implants. In case of a bone fracture, the main support will be provided by an osteosynthesis plate made from cast alloys. The porous Ti-40Nb bodies can be used as mechanically stable substrates of resorbable biomaterials (drugs, bone cements) directly in the bone defects.

The comparison of the results achieved in the present study reveals the excellent mechanical properties of porous Ti-40Nb alloy produced by the above described methods. Niu et al. [85] produced α-phase Ti samples with a porosity in the range of 55‑75%, a corresponding Young´s modulus of 6.4-3 GPa and a plateau stress of 10-35 MPa. A porous Ti‑6Al‑4V α+ß-type alloy with a porosity of 43 to 64% was produced by Esen et al. [106]. The elastic modulus and the yield strength determined in compression tests were in the range of 1.42–14.7 GPa and 28.2–150 MPa, respectively. A ß-type porous Ti–18Nb–4Sn alloy was produced by Xiong et al. [89] The alloy with a porosity of 60% had a Young´s modulus of 10.8 GPa and a compressive strengths of 112 MPa.

Loosely sintered Ti-40Nb powder described in the present study with a porosity of ≈25% demonstrated a Young´s modulus of ≈20 GPa and an ultimate strength of ≈300 MPa, which is very close to the mechanical properties of a human cortical bone. Ti-40Nb samples with a macro- and micro-porosity of ≈60% produced by loose sintering with NaCl space-holders demonstrated mechanical properties similar to those of a spongy human bone: a Young´s modulus of 2 GPa and an ultimate strength of 20 MPa. The

latest samples have an interconnected porosity which is beneficial for bone ingrowth and better implant fixation in the living body.

4.3. Surface modifications

Surface modifications and coatings are used to improve the osseointegration of the implants and to improve their performance in the human body. There are many different ways to modify the surface of the implant (see 2.1.3). A popular method for surface modification of metallic implant materials is coating with bone-like hydroxyapatite $Ca_{10}(OH_2)(PO_4)_6$ (HAP) [107], [108]. Porous Ti-40Nb samples obtained by loose powder sintering with space-holders (produced as described in 4.2.2) were coated with HAP by an electrochemical deposition method. Samples processed with either Mg or NaCl as space-holders were used.

The total porosity of compacts sintered with NaCl as a space-holder was 60 %. Figure 44 shows typical surface morphologies of the HAP coatings after different deposition times at an applied cathodic potential of -1 V vs. SCE. Two types of electrolytes were used for these experiments: electrolyte 1 with 0.61 mMCa$(NO_3)_2$, 0.36 mM $NH_4H_2PO_4$, pH value of 4.5 and double concentrated electrolyte 2 with 1.22 mMCa$(NO_3)_2$, 0.72 mM $NH_4H_2PO_4$, pH value of 6 in electrolyte bath temperature of 80°C.
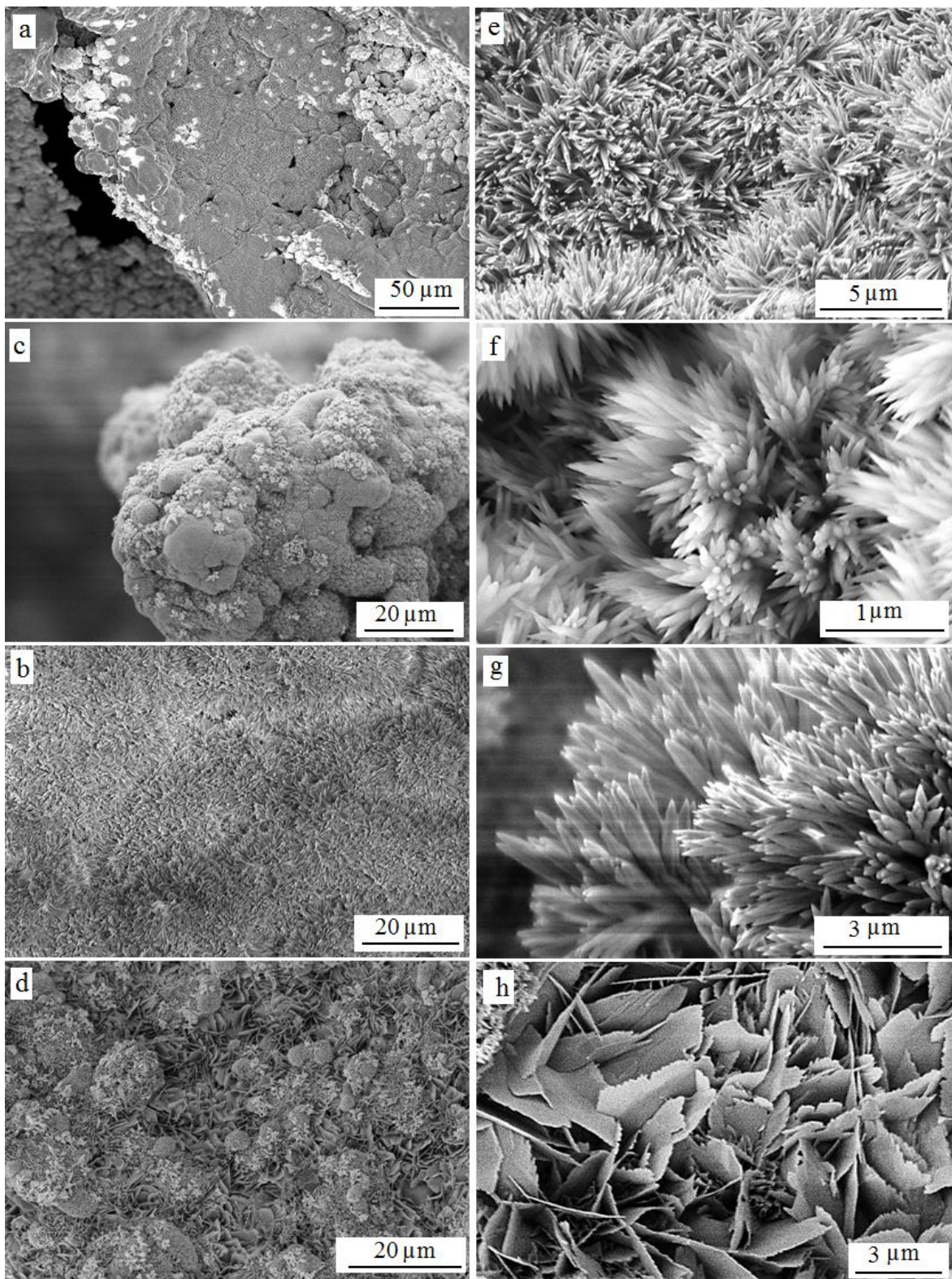
Figure 44: SEM images of HAP coatings on a sample, made with NaCl as space-holder and the corresponding higher resolution images after (a), (e) 1 hour, (b), (f) 2 hours; (c), (g) 3 hours of electrochemical deposition at 1 V vs. SCE in electrolyte 1 and (d), (h) after 3 hours of deposition in electrolyte 2.

After 1 hour of deposition in electrolyte 1 (Figure 44 a), the coating consists of homogeneous needle-like crystals (the morphology of the crystals is clearly visible in Figure 44 e), but it does not completely cover the sample. There are still some gaps in the coating inside of the pores which were detected by SEM. With increasing deposition time to 2 and 3 hours (Figure 44 b and c) in electrolyte 1 the entire surface of the porous sample appears to be homogeneously covered with the HAP layer, including areas inside of the pores. After 3 hours of deposition all the sample is coated with smooth needle-like shaped HAP crystals (Figure 44 g). After 3 hours of deposition in electrolyte 2 all the sample surface is covered with homogeneous HAP coating including the area inside the pores (Figure 44 d). When the electrolyte concentration is increased to the composition of electrolyte 2 the morphology of HAP crystals changes from needle-like to plate-like (Figure 44 h).

Sintered Ti-40Nb samples with a porosity of 50%, produced with Mg particles as space-holder were also submitted to electrochemical deposition of HAP. The development of the layer morphology with increasing deposition time at -1 V vs. SCE in electrolyte 1 is shown in Figures 45 (a) to (c). After 1 hour of deposition (Figure 45 a), a thin layer of HAP is formed on the surface and HAP crystals have the shape of needles (Figure 45 e). The coating inside the pores is much poorer than on the upper cross-sectional surface. After 2 hours of deposition (Figure 45 b) the coating morphology is the same, only the needles became longer, but there are still some gaps in the coating inside of the pores (Figure 45f). Increasing the deposition time to 3 hours results in long needle shaped HAP crystals, which homogeneously cover the entire sample even inside of the pores (Figures 45 c, g). This data is in good agreement with results by Bouyer et al. [109], who reported the formation of needle-like HAP crystals at a temperature above 60 °C. These authors have also indicated by means of TEM that the shape of the HAP crystals varies with the varying electrolyte concentration. Like in the experiments with a previous sample the morphology of HAP crystals has changed from needle-like to plate-like and completely covers the entire sample surface

even inside the pores (Figures 45 d, h). These phenomena can be explained by assuming that the concentration of the electrolyte affects the shape of the precipitated HAP particles and this changes these crystals to less closed forms with plate-like shapes [110].
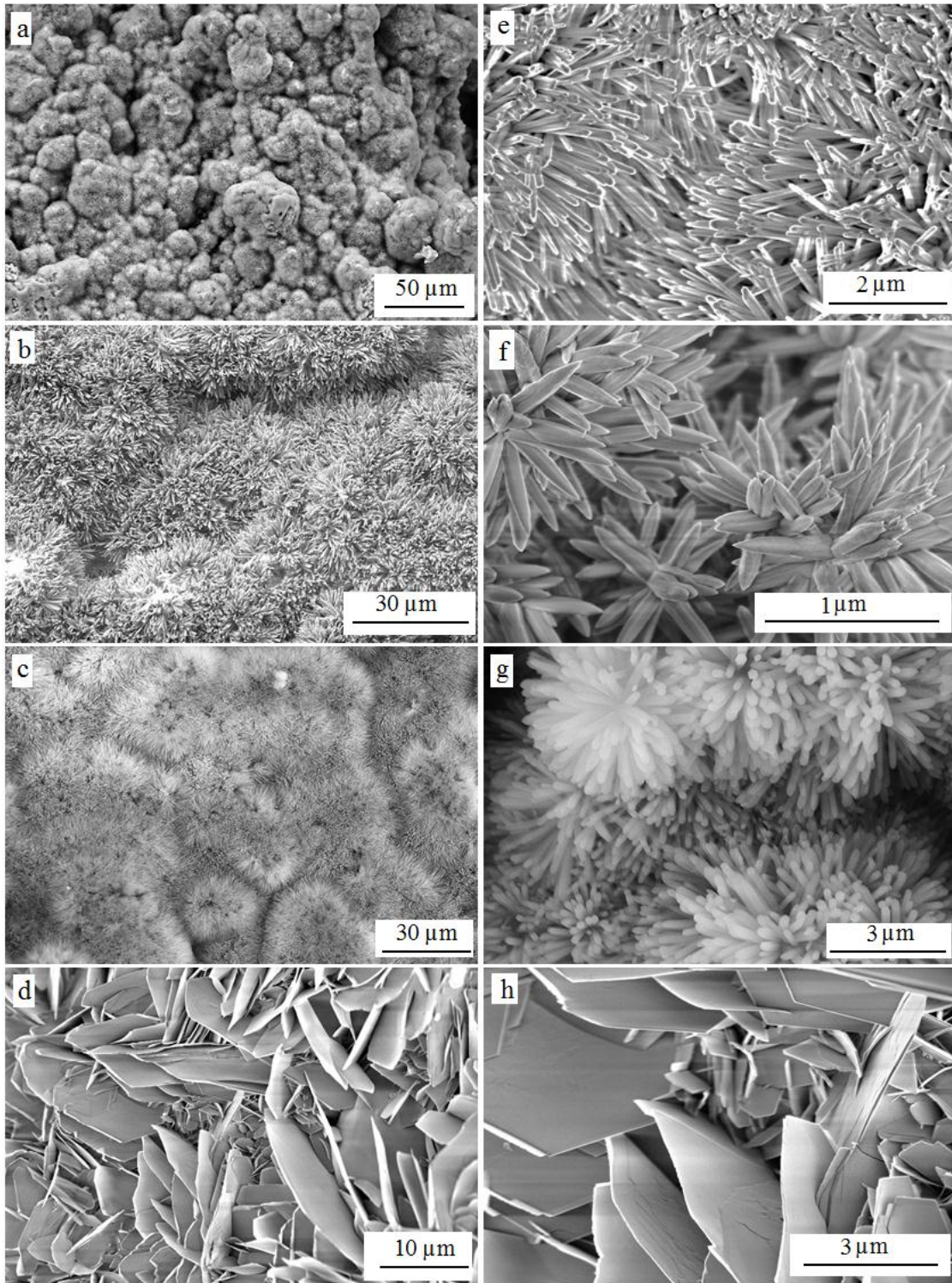
Figure 45: SEM images of HAP coatings on a sample, prepared with Mg as space-holder and corresponding higher resolution images after (a), (e) 1 hour, (b), (f) 2 hours, (c), (g) 3 hours of electrochemical deposition at 1 V vs. SCE in electrolyte 1 and (d), (h) after 3 hours of deposition in electrolyte 2.

Reference Ti-40Nb samples processed by loose powder sintering were also covered with HAP in electrolytes with different concentrations. After 3 hours of deposition in electrolyte 1 the sample´s surface was homogeneously covered with needle-like HAP crystals (Figure 46 a). After 3 hours of deposition in electrolyte 2 the morphology of the crystals changed to plate-like (Figure 46 b). In both cases the coating was homogeneous and no cracks were detected by SEM.
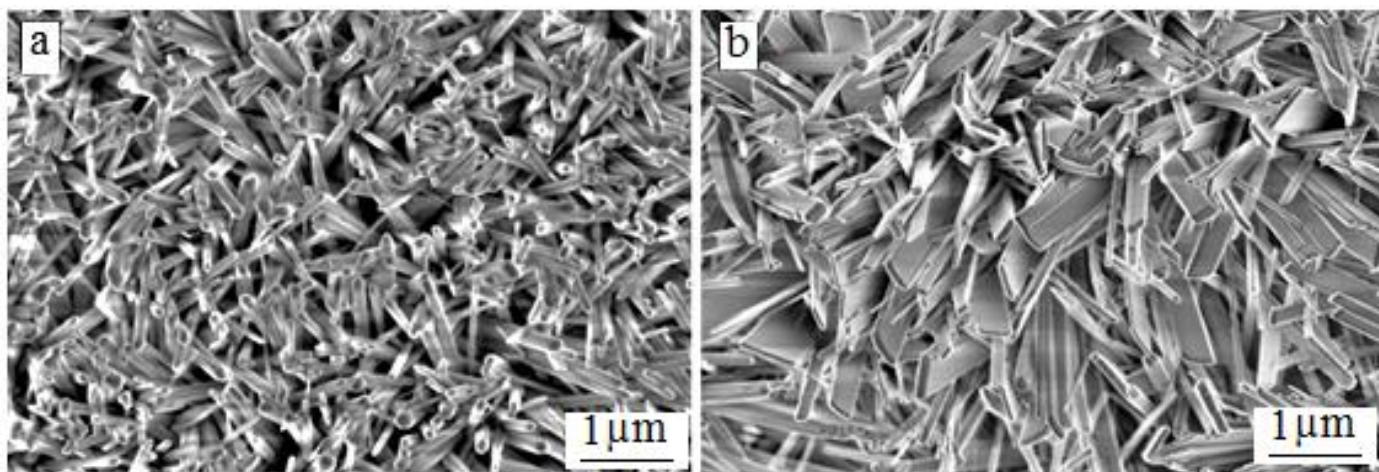

Figure 46: SEM images of HAP coatings on a reference Ti-40Nb sample, prepared by loosely powder sintering after (a) 3 hours of electrochemical deposition in electrolyte 1 and (b) after 3 hours of deposition in electrolyte 2.
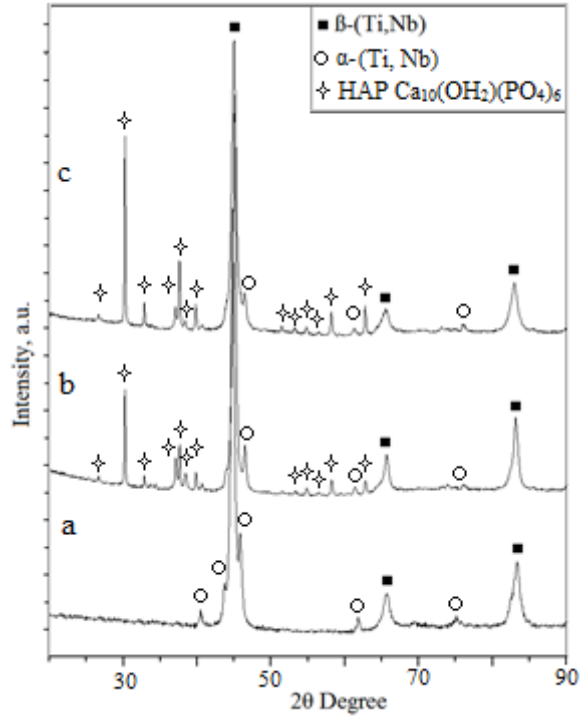
Figure 47: XRD patterns of a reference Ti-40Nb sample, prepared by loose powder sintering (a) before coating, (b) after 3 hours of deposition in electrolyte 1, (c) after 3 hours of deposition in electrolyte 2.

XRD patterns of Ti-40Nb samples taken after electrochemical deposition experiments (Figure 47) show the diffraction peaks that correspond to the HAP phase. Besides those peaks only reflections from Ti-Nb phases were detected. These results confirm that the needle- and plate-like structures observed in the SEM are really HAP. In order to check the composition of the electrodeposited coatings, EDX analyses were carried out for all samples. The Ca-to-P atomic ratio for stoichiometric HAP is 1.67 [16]. For the samples coated in electrolyte 1, the mean value of the Ca-to-P ratio is about 1.7 within the error limits of the method. The atomic percentage of Ca and P in the coating is two times higher than the one achieved in electrolyte 1.

In all cases deposition in electrolyte 1 resulted in smooth needle-shaped HAP crystals, which grew longer with increasing deposition time. The needles on samples produced with NaCl space-holders appear to be longer and bigger than on the other samples produced with Mg as space-holder or with no space-holder. Brown and Fulmer [111] have shown that the presence of NaCl can accelerate the formation of a HAP layer.

There are several shapes of the HAP crystals expected depending on the coating method and conditions: flower-like, plate-like, self-assembled nanorods and many others [112]. The most common geometries of HAP crystals obtained by electrochemical deposition are flake-like (plate-like) and flower-like as was demonstrated by Wang et al. [113]. The authors report on a flake-like structure of HAP crystals produced in 0.042 M $Ca(NO_3)_2$, 0.025 M $NH_4H_2PO_4$ and 0.15 M $NaNO_3$ (mass fraction) electrolyte and the XRD data supported the formation of the HAP layer. The substrates used for electrochemical deposition were commercially pure titanium sheets that did not contain any porosity and had a simple flat geometry. Thus it can be concluded that the processing method and geometry of the substrate does not have a strong influence on the formation of the HAP layer. The same plate-like structure on commercial pure Ti plates was also obtained by Lee et al. [114], but the authors refer to the micro-pores in the material that were completely covered with HAP. In another work by Lee et al. [110] the dependence of the geometry of the HAP coating on the deposition time and temperature was demonstrated. A commercially pure titanium surface was used as a substrate for CaP deposition on oxide micropores formed after anodization. This deposition was performed at a cathodic potential in an electrolyte containing 0.042 M $Ca(NO_3)_2$ and 0.025 M $NH_4H_2PO_4$. The authors report on the formation of a porous HAP layer after short deposition times (1 and 5 minutes) and a needle-like structure after longer deposition time of 1 hour. Changing the deposition temperature to 25°C resulted in the formation of plate-like crystal geometry [110].

In the present study with Ti-40Nb substrates different HAP crystal geometries were obtained in electrolytes with different salt concentrations and after different deposition times. The geometry of the HAP crystals was the same for samples processed with and without space-holders, the length and morphology of the HAP crystals was homogeneous all over the sample. Thus, it can be concluded that electrochemical deposition is not only a cheap and fast way of coating [112], but it is also suitable for an application on ß-type Ti-40Nb substrates with a complicated porous geometry.

Conclusions and Outlook

Considering the design of new load-bearing long-term materials for hard tissue replacement there are two main problems: mechanical biocompatibility and biological "safety" of the material. The mechanical compatibility demands low Young´s modulus values (similar to the bone´s Young´s modulus, i.e. 10-30 GPa for cortical bone, 0.2-2 GPa for spongy bone), relatively high strength (≈150 MPa for cortical bone, 5-50 MPa for spongy bone) and good fatigue properties. Besides that the materials and alloying elements should not be harmful for the human body, i.e. should not cause any allergic or other tissue reactions. These materials are expected to have good corrosion resistance and wear resistance as well.

In the present study which aims at the production of porous ß-type Ti-40Nb alloy samples only biocompatible elements were used (see section 2.1.2): Ti is already a well-known and commonly used implant material and Nb has a very high corrosion resistance, does not cause tissue reactions and is, therefore, also considered to be safe for use in biomedical applications. Ti-Nb alloys were already commercialized (for example as superconductors) and are now promising new materials for biomedical applications.

To fabricate a material with a low Young´s modulus two approaches were followed: an alloy composition of the Ti-Nb system with relatively low Young´s modulus was selected and a certain amount of porosity was introduced into the alloy. Empirical studies with alloys processed under non-equilibrium melt-metallurgical conditions related that there are two minima of the value of Young´s modulus in the Ti-Nb system, i.e. at ≈15 wt.-% Nb and at ≈40 wt.-% Nb (see section 2.2.2). The alloys with a composition around Ti-15Nb are promising shape memory alloys due to martensite stabilization and Ti-40Nb (Ti-45Nb) alloys have the lowest Young´s modulus of ≈62 GPa in cast and solution treated states due to a single metastable ß-phase which can be stabilized at room temperature. Thus, a composition of Ti-40Nb

was chosen. Another way to further reduce the elastic modulus of an alloy body is to give it a porous architecture (see section 2.3). In this work several powder metallurgical methods to produce porous samples were applied. This comprises especially the alloy powder production by mechanical alloying followed by different compaction methods.

For the production of the alloy powder mechanical alloying by ball-milling starting from elemental Ti and Nb powders and employing NaCl as milling agent was conducted. A homogeneous single ß-type phase Ti-40Nb alloy was produced after 40 hours of ball-milling (see 4.1). It has been demonstrated that the milling parameters as well as the purity of the initial powders have a strong influence on the phase composition of the final powder. Intense milling contaminated the powder with oxygen (which is a strong α-phase stabilizer) and, in consequence, upon sintering and quenching the phase composition of the powder changed from β to α+ß mixture. When a Ti starting powder with lower oxygen content was used (0.137 wt.-% O compared to 0.4 wt.-% O in the previously used Ti powder) and gentle milling parameters (interrupted milling with 250 rpm) were applied the oxygen content in as-milled alloy powders dropped to 0.137 wt.-% (compared to 1.77 wt.-% O in previous experiments). This allowed to preserve almost single ß-phase Ti-40Nb alloy states also upon further sintering and quenching (see section 4.1.2).

Porous samples were produced by loose powder sintering, hot-pressing and sintering with space-holders. NaCl or Mg particles were used as a space-holder material. It has been demonstrated that porous samples fabricated by loose powder sintering with NaCl space-holder particles had porosities in a range from 58 to 65% mainly related to the presence of pores of typical dimensions of 150-300 µm resulting in Young´s modulus values which are similar compared to that of spongy bone ($\approx$ 0.2-2 GPa) and strength values of around 30-45 MPa (also similar to those of human spongy bone). Thus, these alloy samples satisfied the demands of low Young´s modulus and an appropriate strength together with suitable macro-porosity for

osseointegration and are, therefore, excellent candidates for long-term load-bearing implants for hard tissue replacement. The improvement of the surface biocompatibility was carried out by a coating of porous samples with hydroxyapatite by electrochemical method resulting in homogeneous coating. The morphology and size of hydroxyapatite crystals can be controlled by deposition time and concentration of the electrolyte solution.

In order to make a short outlook for a further improvement of the present porous Ti-40Nb alloy it can be suggested to apply other techniques for porous sample processing, for example selective laser melting (SLM). Several experiments with SLM of ball-milled Ti-40Nb powder have demonstrated the principal possibility to apply this method to ball-milled powders. One of the main advantages of SLM versus sintering and hot-pressing is a very high cooling rate which is directly and immediately applied to th powder during the laser processing. So a metastable ß-type Ti-40Nb alloy state can be better stabilized. The first samples obtained so far by SLM have porosities of around 20%, providing a Young´s modulus of 33 GPa and an ultimate strength of ≈ 800 MPa. It can be suggested that different SLM parameters will result in different porosities and different, certainly even better, mechanical properties.

Another interesting approach to reduce Young´s modulus and to keep the strength of the samples on a high level is to produce samples with gradient porosity. The outer porous structure is beneficial for the osseointegration and ensures the reduction of the stiffness of the whole sample. The inner core with higher density ensures the strength of the sample. These samples can be produced both by loose powder sintering and by hot pressing.

Acknowledgements

References

[1]. R.M. Berlin, L.J. Gustavson, K.K. Wang, *Cobalt-Base Alloys for Biomedical Applications*, J.A. Disegi, R.L. Kennedy, R. Pillar eds., ASTM STR 1356, ASTM, Werst Conshohocken, PA, 1999, pp.62-70

[2]. M. Niinomi, *Recent metallic materials for biomedical applications*, Metall. Mater. Trans. A, **33A** (2002) 477-486

[3]. M. Niinomi, *Mechanical biocompatibilities of titanium alloys for biomedical applications*, J. Mech. Behavior Biomed. Mater. **1** (2008) 30

[4]. W. F. Ho, C. P. Ju , J. H. Lin, *Structure and properties of cast binary Ti-Mo alloys*, Biomaterials **20** (1999) 2115

[5]. D. Kuroda, M. Niinomi, M. Morinaga, Y. Kato, T. Yashiro, *Design and mechanical properties of new β type titanium alloys for implant materials*, Mater. Sci. Eng. A **243** (1998) 244

[6]. T. Ozaki, *Development of beta titanium alloys with low Young's modulus*, Presented at Materials and Processes for Medical Devices Conference, ASM, St. Paul, USA, 2003

[7]. M. Niinomi, T. Hanawa, T. Narushima, *Japanese research and development on metallic biomedical, dental, and healthcare materials*, JOM **57** (2005) 18-24

[8]. I.H. Oh, N. Nomura, N. Masahashi, S. Hanada, *Mechanical properties of porous titanium compacts prepared by powder sintering*, Scripta Mater. **49** (2003) 1197

[9]. W. Xue, B. V. Krishna, A. Bandyopadhyay, S. Bose, *Processing and biocompatibility evaluation of laser processed porous titanium*, Acta Biomater. **3** (2007) 1007

[10]. M. A. Lopez-Heredia, J. Sohier, C. Gaillard, S. Quillard, M. Dorget, P. Layrolle, *Rapid prototyped porous titanium coated with calcium phosphate as a scaffold for bone tissue engineering*, Biomaterials, **29** (2008) 2608

[11]. X. Miao, Y. Hu, J. Liu, X. Huang, *Hydroxyapatite coating on porous zirconia*, Mater. Sci. Eng. C **27** (2007) 257

[12]. Y.Y. Zhuang, R. Hu, H.Y. Shi, J. Tang, C.J. Lin, 6th Asian Symposium on Biomedical Materials (ASM6) Emei, China, 2004

[13]. J. Park, R.S. Lakes, *Biomaterials: an introduction*, Springer Science Business Media LLC (2007)

[14]. B. V. Krishna, S. Bose, A. Bandyopadhyay, *Low stiffness porous Ti structures for load-bearing implants*, Acta Biomater. **3** (2007) 997-1006

[15]   A. Geetha, A.K. Singh, R. Asokamani, A.K. Gogia, *Ti based biomaterials, the ultimate choice for orthopaedic implants – A review*, Prog. Mater. Sci. 54 (2009) 397-425

[16].   M.P. Staiger, A. M. Pietak, J. Huadmai, G. Dias, *Magnesium and its alloys as orthopedic biomaterials: A review*, Biomaterials **27** (2006) 1728–1734

[17].   M. Long, H.J. Rack , *Titanium alloys in total joint replacement – a materials science perspective* Biomaterials **19** (1998) 1621-1639

[18].   M. Niinomi, D. Kuroda, K. Fukunaga, *Corrosion wear fracture of new beta type biomedical titanium alloys,* M. Mater. Sci. Eng. A, **A263** (1999) 193–199

[19].   Y. L. Zhou, M. Niinomi, T.Akahori, H. Fukui, H. Toda, *Corrosion resistance and biocompatibility of Ti-Ta alloys for biomedical applications* , Mater. Sci. Eng. A, **398** (2005) 28–36

[20].   J.L. Woodman, J.J. Jacobs, J.O. Galante, R.M. Urban, *Metal ion release from titanium-based prosthetic segmental replacements of long bones in baboons: A long-term study*, J. Orthop. Res. **1** (1984) 421-430

[21].   K. Merritt, S.A. Brown, *Metal Sensitivity Reactions to Orthopedic Implants*, Internat. J. of Dermatol. **20** (1981) 89-94

[22].   M. Niinomi, *Fatigue performance and cyto-toxicity of low rigidity titanium alloy, Ti-29Nb-13Ta-4.6Zr*, Biomaterials **24** (2003) 2673–2683

[23].   J.C. Hornez, A. Lefèvre, D. Joly, H.F. Hildebrand, *Multiple parameter cytotoxicity index on dental alloys and pure metals*, Biomol. Eng. **19** (2002), 103–117

[24].   M. Niinomi, *Materials for biomedical devices*, Woodhead publishing limited, 2010, 366

[25].   T. Rae, *The toxicity of metals used in orthopaedic prostheses. An experimental study using cultured human synovial fibroblasts*, J. Bone Joint Surg. **63-b** (1981) 435-440

[26].   P.G. Laing, A.B. Fergosun, E.S. Hodge, *Tissue reaction in rabbit muscle exposed to metallic implants*, J. Biomed. Mater. Res. **1** (1967) 135-149

[27].   X. Liu, P. K. Chu, C. Ding, *Surface modification of titanium, titanium alloys, and related materials for biomedical applications*, Mater. Sci. Eng. R **47** (2004) 49

[28].   J. Lausmaa, D.M. Brunette, P. Tengvall, M. Textor, P. Thomsen (Eds.), *Titanium in Medicine*, Springer, Berlin (2001), 231–266

[29].   G. He, M. Hagiwara, *Ti alloy design strategy for biomedical applications*, Mater. Sci. Eng. C **26** (2006) 14-19

[30]. C. Leyens, M. Peters, *Titanium and titanium alloys: fundamentals and applications*, Wiley-VCH (2003)

[31]. L.J. Murray, *Binary Alloy Phase Diagrams*, Second Edition, T.B. Massalski (editor-in-chief) Materials Information Soc., Materials Park, Ohio (1990)

[32]. D.L. Moffat, U. R. Kattner, *The Stable and Metastable Ti-Nb Phase Diagrams*, Metall. Trans. A **19A** (1988) 2389-2397

[33]. J.P. Morniroli, M. Gantois, *Study of conditions under which omega-phase forms in Titanium-Niobium and Titanium-Molybdenium alloys*, Mem. Sci. Rev. Metall., **70** (1973) 831-842

[34]. J. Sun, Q. Yao, H. Xing, W.Y. Guo, *Elastic properties of β, α'' and ω metastable phases in Ti–Nb alloy from first-principles,* J. Phys: Condens. Matter. **19** (2007) 486215

[35]. H. Ikehata, N. Nagasako, T. Furuta, A. Fukumoto, K. Miwa, T. Saito, *First-principles calculations for development of low elastic modulus Ti alloys*, Phys. Rev. **B 70** (2004) 1741113

[36]. H.Y. Kim, Y. Ikehara, J.I. Kim, H. Hosoda, S. Miyazaki, *Martensitic transformation, shape memory effect and superelasticity of Ti–Nb binary alloys*, Acta Mater. **54** (2006) 2419–2429

[37]. B.A. Hatt, V.G. Rivlin, *Phase transformations in superconducting Ti-Nb alloy*s, Brit. J. Appl. Phys. **1** (1968) 1145-1149

[38]. N. Nomura, K. Sakamoto, K. Takahashi, S. Kato, *Fabrication and Mechanical Properties of Porous Ti/HA Composites for Bone Fixation Devices*, Mater. Trans. **51** (2010) 1449-1454

[39]. Y. Kuboki, H. Takita, D. Kobayashi, E. Tsuruga, M. Inoue, M. Murata, *BMP‐Induced osteogenesis on the surface of hydroxyapatite with geometrically feasible and nonfeasible structures: Topology of osteogenesis*, J. Biomed. Mater. Res. **39** (1998), 190–199

[40]. S.F. Hulbert, F.A. Young, R.S. Mathews, J.J. Klawitter, C.D. Talbert, F.H. Stelling, *Potential of ceramic materials as permanently implantable skeletal prostheses*, J. Biomed. Mater. Res. **4** (1970) 433–456

[41]. P.C. Angelo, R. Subramanian, *Powder metallurgy: science, technology and applications*, Eastern Economy Edition (2009)

[42]. Y.P. Zhang, B. Yuan, M.Q. Zeng, C.Y. Chung, X.P. Zhang, *High porosity and large pore size shape memory alloys fabricated by using pore-forming agent (NH4HCO3) and capsule-free hot isostatic pressing*, J. Mater. Proc. Tech. **192** (2007) 439–442

[43]. G.Ryan, A. Pandit, D. P. Apatsidis, *Fabrication methods of porous metals for use in orthopaedic applications*, Biomaterials **27** (2006) 2651-2670

[44]. T. Aydogmus, S. Bor, *Processing of porous TiNi alloys using magnesium as space holder*, J. Alloy Compd. **478** (2009) 705–710

[45]. A. Bansiddhi, D.C. Dudand, *Shape-memory NiTi foams produced by replication of NaCl space-holders*, Acta Biomater. **6** (2008) 1996-2007

[46]. L. Facchini, E. Magalini, P. Robotti, *Ductility of a Ti-6Al-4V alloy produced by selective laser melting of prealloyed powders*, Rapid Prototyping J. **16** (2010) 450-459

[47]. L.C. Zhang, D. Klemm, J. Eckert, Y.L. Hao, T.B. Sercombe, *Manufacture by selective laser melting and mechanical behavior of a biomedical Ti–24Nb–4Zr–8Sn alloy*, Scripta Mater. **65** (2011) 21–24

[48]. D. K. Pattanayak, A. Fukuda, T. Matsushita, M. Takemoto, S. Fujibayashi, K. Sasaki, N. Nishida, T. Nakamura, T. Kokubo, *Bioactive Ti metal analogous to human cancellous bone: Fabrication by selective laser melting and chemical treatments*, Acta Biomater. **7** (2011) 1398–1406

[49]. A. Fukuda, M. Takemoto, T. Saito, S. Fujibayashi, *Bone bonding bioactivity of Ti metal and Ti–Zr–Nb–Ta alloys with Ca ions incorporated on their surfaces by simple chemical and heat treatments,* Acta Biomater. **7** (2011) 2327-2336

[50]. D. Handtrack, F. Despana, C. Sauer, B. Kieback, N. Reinfried, Y. Grin, *Fabrication of ultra-fine grained and dispersion-strengthened titanium materials by spark plasma sintering*, Mater. Sci. Eng. A **437** (2006) 423–429

[51]. C. Suryanarayana, *Mechanical alloying and milling*, Prog. Mater. Sci.**46** (2001) 1-184

[52]. P. R. Soni, *Mechanical Alloying: Fundamentals and Applications*, Cambridge Internationsl Scince Publishing (2001)

[53]. E. Hellstern, H.J. Fecht, C. Garland, W.L. Johnson. In: McCandlish LE, Polk DE, Siegel RW, Kear BH, editors. Multicomponent ultrafine microstructures, Pittsburgh, PA: Mater. Res. Soc, (1989)

[54]. I. S. Polkin, A. B. Borzov, *New materials produced by mechanical alloying*, Adv. Perform. Mater. **2** (1995) 99-109

[55]. T. Koyano, T. Takizawa, T. Fukunaga, U. Mizutani, S. Kamizuru, E. Kita, A. Tasaki, *Mechanical alloying process of Fe‑ Cr powders studied by magnetic measurements*, J. Appl. Phys. **73** (1993), 429–433

[56]. C. Suryanarayana, *Does a disordered γ-TiAl phase exist in mechanically alloyed Ti-Al powders?* Intermetallics **3** (1995) 153-160

[57]. H.J. Fecht, G. Han, Z. Fu, W.L. Johnson, *Metastable phase formation in the Zr- Al binary system induced by mechanical alloying*, J. Appl. Phys. **67** (1990) 1744-1748

[58]. C. Suryanarayana, F. H. Froes, *Mechanical Alloying of Titanium-Base Alloys*, Adv. Mater. **5** (1993) 96-106

[59]. C.C. Koch, O.B. Cavin, C. G. McKamey, J.O. Scarbroug, *Preparation of ''amorphous'' Ni60Nb40 by mechanical alloying*, Appl. Phys. Letters **43** (1983) 1017-1019

[60]. C. Machio, D. Nyabadza, H.K. Chikwanda, M. Pasha, V.M. Sibanda, *Mechanical alloying and sintering of Ti-10wt.% Mg powders*, Mater. Sci. Forum **618 - 619** (2009) 105-108

[61]. A. Omran, K. Woo, E. Kwon, N.A. Barakat, H. Lee, S. Kim, D. Zhang, *Fabrication of biocompatible ß-Ti-Nb-Sn alloy by pulsed current activated sintering using high energy ball milled powder*, Sci. Adv. Mater. **1** (2009) 205-211

[62]. Z.C. Zhou, J.Y. Xiong, S.Y. Gu, D.K. Yang, J. Du, *Anelastic relaxation caused by interstitial atoms in ß-type sintered Ti-Nb alloys*, J. Alloy Comp. **509** (2011) 7356-7360

[63]. A. S. Khan, H. Zhangr, L. Takac, *Mechanical response and modeling of fully compacted nanocrystalline iron and coppe*r, Int. J. Plasticity, **16** (2000) 1459–1476

[64]. Y.A. Giffoni, E.C.T. Ramos, H.R.Z. Sandim, M.T.T. Pacheco, *Structural evaluation of mechanically alloyed Ti-Nb powders*, Mater. Sci. Forum **591-593** (2008) 141-146

[65]. L. Schultz, J. Eckert, *Mechanically alloyed glassy metals*, Top. Appl. Phys. **72** (1994) 69-120

[66]. M. Phasha, K. Maweja, C. Babst, *Mechanical alloying by ball milling of Ti and Mg elemental powders: Operation condition considerations*, J. Alloy Compd. **492** (2010) 201-207

[67]. P. Bhattacharya, P. Bellon, R.S. Averback, S.J. Hales, *Nanocrystalline TiAl powders synthesized by high-energy ball milling: effects of milling parameters on yield and contamination*, J. Alloy Compd. **368** (2004) 187-196

[68]. A. Nouri, P. D. Hodgson, C. Wen, *Effect of process control agent on the porous structure and mechanical properties of a biomedical Ti–Sn–Nb alloy produced by powder metallurgy*, Acta Biomater. **6** (2010) 1630-1639

[69]. M. Hida, K. Asai, Y. Takemoto, A. Sakakibara, *Solid solubility in nanocrystalline Ti/Mg and Mg/Ti composites powder produced by mechanical alloying*, Mater. Sci. Forum **235-238** (1997) 187-192

[70]. H. Bahmanpour, K.M. Yousseff, M. S. Khoshkhoo, S. Scudino, J. Eckert, R.O. Scattergood, C.C. Koch, *Microstructure and mechanical properties of Cu-Zn alloys produced by surfactant-assisted ball milling*, Presented at MRS Fall Meeting, Boston, MA (2011)

[71]. U.M.R. Seelam, G. Barkhordarian, A. Suryanarayana, *Is there a hexagonal-close-packed (hcp) → face-centered-cubic (fcc) allotropic transformation in mechanically milled Group IVB elements?* J. Mater. Res. **24** (2009) 3454-3461

[72]. A. Nouri, P. Hodgson, C. Wen, *Effect of ball-milling time on the structural characteristics of biomedical porous Ti–Sn–Nb alloy*, Mater. Sci. Eng. C **31** (2011) 921-928

[73]. M. N. Ahsan, A. J. Pinkerton, R.J. Moat, J. Shackleton, *A comparative study of laser direct metal deposition characteristics using gas and plasma-atomized Ti–6Al–4V powders*, Mater. Sci. Eng. A **528** (2011) 7648–7657

[74]. G. Martins, C. R. M. Silva, C. A. Nunes, *Beta Ti-45Nb and Ti-50Nb Alloys Produced by Powder Metallurgy for Aerospace Application*, Mater. Sci. Forum **660-661** (2010) 405-409

[75]. R.L. Sands, C.R. Shakespeare, *Powder Metallurgy Practice and Applications*, London : Newnes (1966)

[76]. S.J.L. Kang, *Sintering. Densification, Grain growth and microstructure*, Elsevier (2005)

[77]. G. S. Upadhyaya, *Powder Metallurgy Technology*, Cambridge international science publishing, (2002)

[78]. B. Kieback, M. Noethe, R. Grupp, J. Banhart, T. Rasp, T. Kraft, *Analysis of particle rolling and intrinsic rotations in copper powder during sintering*, J. Mater. Sci. **47** (2012) 7047–7055

[79]. B. Kieback, A. Neubrand, H. Riedel, *Processing techniques for functionally graded materials*, Mater. Sci. Eng. A **362** (2003) 81-106

[80]. K Asaoka, N Kuwayama, O Okuno, *Mechanical properties and biomechanical compatibility of porous titanium for dental implants*, J. Biomed. Mater. Res. **19** (1985) 699-713

[81]. E. Arzt, M. E Ashby, K. E. Easterling, *Practical Applications of Hot-lsostatic Pressing Diagrams: Four Case Studies*, Metal. Trans. A **14a** (1983) 211-221

[82]. V.A.R. Henriques, H.R.Z. Sandim, G.C. Coelho, C.R.M. da Silva, *Microstructural evolution during hot pressing of the blended elemental Ti–6%Al–7%Nb alloy*, Mater. Sci. Eng. A **347** (2003) 315-324

[83]. P. Patnaik, *Handbook of inorganic chemicals*. New-York: McGraw-Hill (2003)

[84]. W. Niu, S. Gill, H. Dong, C. Bai, *A two-scale model for predicting elastic properties of porous titanium formed with space-holders*, Comp. Mater. Sci. **50** (2010) 172-178

[85]. W. Niu, C. Bai, G. Qiu, Q.Wang, *Processing and properties of porous titanium using space holder technique*, Mater. Sci. Eng. A **506** (2009) 148–151

[86]. Z. Gao, Q. Li, F. He, *Mechanical modulation and bioactive surface modification of porous Ti–10Mo alloy for bone implants*, Mater. Design **42** (2012) 13–20

[87]. M. H. Lee, K. B. Kim, J. H. Han, J. Eckert, D. J. Sordelet, *High strength porous Ti–6Al–4V foams synthesized by solid state powder processing*, J. Phys. D: Appl. Phys. **41** (2008) 105404

[88]. M. Bram, H. Schiefer, D. Bogdanski, M. Koller, H. P. Buchkremer, D. Stover, *Implant surgery: How bone bonds to PM titanium*, Met. Powder Rep. **61** (2006) 26-31

[89]. J. Xiong, Y. Li, X. Wang, P. Hodgson, C. Wen, *Mechanical properties and bioactive surface modification via alkali-heat treatment of a porous Ti–18Nb–4Sn alloy for biomedical applications*, Acta Biomater. **4** (2008) 1963–1968

[90]. J.Y. Wong, J.D. Bronzino, D.R. Peterson, *Biomaterials: principles and Practices*, CTR Press (2012)

[91]. N. Schlorke-de Boer, *Metallische Massivgläser auf Fe-Al-P-C-B-(Ga-) Basis und Verbundmaterialen mit Mg-Y-Cu-Glas-Matrix*, Ph.D. Thesis, Technische Universität Dresden (2001)

[92]. P. Thompson, I.G. Wood, *X-ray Rietveld refinement using Debye-Scherrer geometry*, J. Appl. Crystallogr. **16** (1983) 458-472

[93]. B. Budiansky, *On the elastic moduli of some heterogeneous materials*, J. Mech. Phys. Solids **13** (1965) 223-227

[94]. E. Ryshkewitch, *Compression Strength of Porous Sintered Alumina and Zirconia*, J. Am. Ceram. S. **36** (1953) 65-68

[95]. M. Todo, H. Kuraoka, J. Kim, K. Taki, M. Ohshima, *Deformation behavior and mechanism of porous PLLA under compression*, J. Mater. Sci. **43** (2008) 5644–5646

[96]. V. Kefalas, D.A. Eftaxiopoulos, *Experimental study of cancellous bone under large strains and a constitutive probabilistic mode,l* J. Mech. Behav. Biomed. **6** (2012) 41-52

[97]. Y.S. Kwon, K. B. Gerasimov, S.K. Yoon, *Ball temperatures during mechanical alloying in planetary mills*, J. Alloy Compd. **346** (2002) 276-181

[98]. E. Ivanov, I. Konstanchuk, B. Bokhonov, V. Boldyrev, *Hydrogen interaction with mechanically alloyed magnesium–salt composite materials*, J. Alloy Compd. **359** (2003) 320-325

[99]. J. Phasha, A. S. Bolokang, P. E. Ngoepe, *Solid-state transformation in nanocrystalline Ti induced by ball milling*, Mater. Lett. **64** (2010) 1215-1218

[100]. I. Manna, P. P. Chattopadhyay, P. Nandi, F. Banhart, H.J. Fecht, *Formation of face-centered-cubic titanium by mechanical attrition*, J. Appl. Phys. **93** (2003) 1520-1524

[101]. A.T. Balcerzak, S.L. Sass, *The formation of the ω phase in Ti-Nb alloys*, Metall. Trans. **3** (1972) 1601-1605

[102]. D.L. Moffat, D.C. Larbalestier, *The competition between martensite and omega in quenched Ti-Nb alloys*, Metall. Trans. A **19A** (1988) 1677-1686

[103]. L. Shaw, J. Villegas, H. Luo, M. Zawrah, D. Miracle, *Effects of process-control agents on mechanical alloying of nanostructured aluminum alloys*, Metall. Mater. Trans. A **34** (2003) 159-170

[104]. M. Nakai, M. Niinomi, T. Akahori, H. Tsutsumi, M. Ogawa, *Effect of Oxygen Content on Microstructure and Mechanical Properties of Biomedical Ti-29Nb-13Ta-4.6Zr Alloy under Solutionized and Aged Conditions*, Mater. Trans. **50** (2009) 2716-2720

[105]. C.Ouchi, *Mettalurgy and Technology of Practical Titanium Alloys*, ed. By Fujishiro S, Eylon D, Kishi T (TMS, Warrendale, PA, 1994) 10

[106]. Z. Esen, S. Bor, *Characterization of Ti–6Al–4V alloy foams synthesized by space holder technique*, Mater. Sci. Eng. A **528** (2011) 3200–3209

[107]. L.G. Gibson, M.F. Ashby, *Cellular Solids: Structure and Properties*, Cambridge: Cambridge University press (1999)

[108]. M. Sivakumar, I. Manjubala, *Preparation of hydroxyapatite/fluoroapatite-zirconia composites using Indian corals for biomedical applications*, Mater. Lett. **4** (2001) 199-205

[109]. E. Bouyer, F. Gitzhofer, M. I. Boulos, *Morphological study of hydroxyapatite nanocrystal suspension*, J. Mater. Sci. **11** (2000) 523-531

[110]. K. Lee, Y.H. Jeong, Y.M. Ko, H.C. Choe, W.A. Brantley, *Hydroxyapatite coating on micropore-formed titanium alloy utilizing electrochemical deposition*, Thin Solid Films, In Press, Corrected Proof, Available online 7 September 2013

[111]. P.W. Brown, M. Fulmer, *Kinetics of hydroxyapatite formation at low-temperature*, J. Am. Ceram. S. **74** (1991) 934-940

[112]. M. Sadat-Shoja, M.T. Khorasani, E. Dinpanah-Khoshdargi, A. Jamshidi, *Synthesis methods for nanosized hydroxyapatite with diverse structures*, Acta Biomater. **8** (2013) 7591-7621

[113]. J. Wang, Y. Chao, Q. Wan, Z. Zhu, H. Yu, *Fluoridated hydroxyapatite coatings on titanium obtained by electrochemical deposition*, Acta Biomater. **5** (2009) 1798-1807

[114]. K. Lee, Y.H. Jeong , W. A. Brantley, H.C. Choe, *Surface characteristics of hydroxyapatite films deposited on anodized titanium by an electrochemical method*, Thin Solid Films, **546** (2013) 185-188

List of publications

Parts of this work were published in the following publications:

1. K. Zhuravleva, S. Scudino, M. S. Khoshkhoo, A. Gebert, M. Calin, L. Schultz, J. Eckert, *Mechanical Alloying of β-Type Ti–Nb for Biomedical Applications*, Adv. Eng. Mater. **15** (2013) 262-268

2. K. Zhuravleva, A. Chivu, A. Teresiak, S. Scudino, M. Calin, L. Schultz, J. Eckert, A. Gebert, *Porous low modulus Ti40Nb compacts with electrodeposited hydroxyapatite coating for biomedical applications*, Mater. Sci. Eng. C **33** (2013) 2280-2287

3. K. Zhuravleva, M. Bönisch, S. Scudino, M. Calin, L. Schultz, J. Eckert, A. Gebert, *Phase transformations in ball-milled Ti-40Nb and Ti-45Nb powders upon quenching from the β-phase region*, Powder Technol. **253** (2014) 166–171

4. K. Zhuravleva, M. Bönisch, K. G. Prashanth, U. Hempel, A. Helth, T. Gemming, M. Calin, S. Scudino, L. Schultz, J. Eckert, A. Gebert, *Production of Porous β-Type Ti–40Nb Alloy for Biomedical Applications: Comparison of Selective Laser Melting and Hot Pressing,* Materials **6** (2013) 5700-5712

Erklärung

Hiermit versichere ich, daß ich die vorliegende Arbeit ohne unzulässige Hilfe Dritter und ohne Benutzung anderer als der angegeben Hilfsmittel angefertigt habe; die aus fremden Quellen direkt übernommenen Gedanken sind als solche kenntlich gemacht. Die Arbeit wurde bisher weder im Inland noch im Ausland in gleicher oder ähnlicher Form einer anderen Prüfungsbehörde vorgelegt.

Die vorliegende Arbeit wurde in Zeitraum März 2011 bis Juli 2014 am Institute für Metallische Werkstoffe des Institute für Festkörper- und Werkstoffforschung (IFW) Dresden unter der wissenschaftlichen Betreuung von Herrn Prof. Dr. L. Schultz angefertigt.

Es haben zuvor keine erfolglosen Promotionsversuche stattgefunden.

Hiermit erkläre ich, daß ich die bestehende Prüfungsordnung der Fakultät Mathematik und Naturwissenschaften der Technischen Universität Dresden vom 16.04.2003 anerkenne.